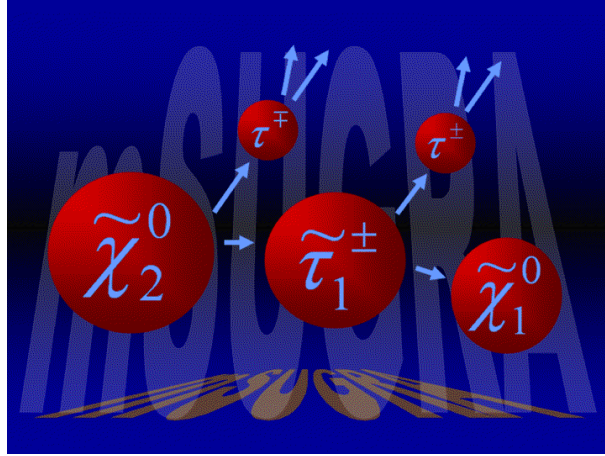


The discovery potential of the
 $\tilde{\chi}_2^0$ in mSUGRA in the τ -channel
at high $\tan \beta$ at the LHC



Diploma thesis

Florian Heinemann

ETH Zurich, Switzerland

performed at CERN

supervised by

Dr. André Holzner, ETHZ

Dr. Luc Pape, CERN

Prof. Dr. Felicitas Pauss, ETHZ

November 2003 to March 2004

Contents

1	Introduction	1
2	Supersymmetry	3
2.1	MSSM	3
2.2	Superpotential and R-parity	5
2.3	mSUGRA	5
3	Monte Carlo generators	7
3.1	ISASUGRA	7
3.2	PYTHIA	7
4	Experiments	9
4.1	Large Electron Positron Collider	9
4.2	Wilkinson Microwave Anisotropy Probe	12
4.3	Large Hadron Collider	13
5	Kinematics for $\tilde{\chi}_2^0$ searches	17
5.1	Sequential two-body decays	17
5.2	Formulae and kinematic configurations	20
5.3	Endpoints for top quark events	22
6	Searches for the $\tilde{\chi}_2^0$	25
6.1	Searches at low $\tan\beta$	25
6.2	Searches at $\tan\beta = 35$	27
6.2.1	Choice of parameters	28
6.2.2	Production, decay and selection of $\tilde{\chi}_2^0$	30
6.2.3	Methods to find the endpoint	33
	Linear fit	33
	Gaussian fit	34
6.2.4	Selection of the leptonic decay	35
6.2.5	The kinematic limit of $M_{\rho^\pm \rho^\mp q}$	36
6.2.6	Selection of quarks	41
6.2.7	The kinematic limit of $M_{\rho^\pm \rho^\mp q}$ for light quarks	41
6.2.8	Two kinematic limits in $M_{\rho^\pm q}$ for light quarks	45
6.2.9	The kinematic limit of $M_{\rho_1^\pm q} + M_{\rho_2^\mp q}$ for light quarks	54
6.2.10	The kinematic limit of $M_{\rho^\pm \rho^\mp q}$ for bottom quarks	59
6.2.11	Two kinematic limits in $M_{\rho^\pm q}$ for bottom quarks	63
6.2.12	The kinematic limit of $M_{\rho_1^\pm q} + M_{\rho_2^\mp q}$ for bottom quarks	70
6.2.13	The kinematic limit of $M_{\rho^\pm \rho^\mp q}$ for top quarks	75
6.2.14	Two kinematic limits in $M_{\rho^\pm q}$ for top quarks	78
6.2.15	The kinematic limit of $M_{\rho_1^\pm q} + M_{\rho_2^\mp q}$ for top quarks	85

6.2.16	Examples of measurements with 30 fb^{-1}	90
7	Conclusions	95
8	Outlook	97
A	Problems using PYTHIA 6.220	99
A.1	Bug in the hadronic tau decay	99
A.2	Particle listing	99
A.3	PYTHIA 6.220 and TAUOLA	99
A.4	Calculated cross sections	100
	Bibliography	102
	Acknowledgements	103

Abstract

One of the goals of the Large Hadron Collider (LHC) is to search for supersymmetric particles predicted by the minimal Supergravity Model (mSUGRA). In previous studies the discovery potential for the next-to-lightest neutralino ($\tilde{\chi}_2^0$) has been investigated in many areas of its parameter space. It has been pointed out that the leptonic decay of the $\tilde{\chi}_2^0$ offers kinematic properties which can be well used for mass reconstructions of sparticles. However, in the parameter space where taus dominate the leptonic decay, the $\tilde{\chi}_2^0$ discovery is especially difficult since a full tau reconstruction will not be possible at LHC. In several recent publications it has been indicated that studies are necessary in that region.

This study analyses the possibility of using kinematic endpoints for a sparticle mass reconstruction at $\tan\beta = 35$, $A_0 = 0$ and $\mu > 0$. A region of 25 points around the benchmark point I' with $m_0 = 181$ and $m_{1/2} = 350$ is chosen where the cascade decay $\tilde{\chi}_2^0 \rightarrow \tau^\pm + \tilde{\tau}^\mp \rightarrow \tau^\pm + \tau^\mp + \tilde{\chi}_1^0$ has a branching ratio of over 95%. In this cascade decay at least three particles, the $\tilde{\chi}_1^0$ and two ν_τ , escape the detector. Therefore, a precise mass reconstruction in the investigated region using the kinematic limits is not possible. However, this study shows that some invariant mass endpoints can be well estimated, using a m_0 and $m_{1/2}$ independent correlation between the distribution maximum and the kinematic limit. Furthermore, a linear fit at the tail of the invariant mass distribution gives in most of the cases a good estimate as well. In addition, a method is described how to measure two endpoints within the single rho with one quark invariant mass distribution. The influence of the mixing between \tilde{b}_1 (\tilde{t}_1) and the heavier \tilde{b}_2 (\tilde{t}_2) on endpoint measurements is also discussed.

The simulations are performed with PYTHIA 6.220 in combination with ISASUGRA 7.69. The results are at Monte Carlo level, and give the minimal systematic and statistical uncertainties on measurements of 13 kinematic endpoints. For the mass reconstruction of sparticles with a 30 fb^{-1} data sample the minimal uncertainties of 20.4 GeV (7.9%) for the $\tilde{\chi}_2^0$, 20.5 GeV (14.8%) for the $\tilde{\chi}_1^0$, 21.2 GeV (14.0%) for the $\tilde{\tau}_1^\pm$, 28.2 GeV (3.6%) for the \tilde{d}_1 and \tilde{s}_1 , 25.7 GeV (3.6%) for the \tilde{b}_2 and 28.8 GeV (3.9%) for the \tilde{t}_2 have been calculated.

Chapter 1

Introduction

Today, the Standard Model [1] of electroweak and strong interactions describes nature at the smallest scales accessible in high energy physics. Both theories are based on the same fundamental principle, the local gauge invariance. Through precision measurements at LEP and SLC the electroweak theory has been checked very thoroughly, and no obvious deviation or inconsistency has been observed. The only particle of that theory that still has to be discovered is the Higgs boson. It is necessary for explaining the existence of massive fundamental particles in nature. Quantum Chromodynamic (QCD), describing the strong interactions within the Standard Model, is tested very well at HERA. Only for gravitation, it has not been possible yet to construct a theory based on quantum mechanics which can be tested in experiments.

However, there are a lot of open questions which have to be solved. The origin of mass, the reason for the huge matter antimatter asymmetry in the universe and the nature of cold dark matter are not known until now. The Standard Model has a large number of parameters which - instead of arising from a more fundamental theory - have to be measured. Furthermore, there are theoretical motivations for physics beyond the Standard Model. One is the hierarchy problem concerning the quadratically divergent fermion loop corrections to the Higgs mass. Additionally, - for reasons of concinnity - theorists want to unify the gauge couplings. J.C. Maxwell working out his famous equations as well as S. Glashow, S. Weinberg and A. Salam - all three responsible for the electroweak unification - have shown that a unification of theories can be very successful.

In order to answer some of these questions, one possibility is to extend the Standard Model Poincaré algebra to a supersymmetric graduated Lie algebra which leads to a larger particle spectrum. The model with the minimal particle content is the Minimal Supersymmetric Standard Model (MSSM). It is an important prediction of this theory that every particle described by the Standard Model has a supersymmetric partner, a sparticle: Each fermion has a bosonic and each boson has a fermionic superpartner. However, none of the predicted sparticles has been discovered yet. If our universe really was supersymmetric directly at the Big Bang, Supersymmetry had to be broken at a very short time after it. Otherwise, every particle would have the same mass as its superpartner, which is definitely excluded by experiments. The MSSM solves the hierarchy problem, provided there are sparticles in the 1 – 10 TeV mass region. It makes a unification of the gauge couplings possible, and in some cases even predicts a candidate for cold dark matter. Furthermore, the MSSM gives strong constraints for the lightest Higgs mass which there has to be lower than 130 GeV [2].

The mechanism for breaking Supersymmetry is not specified in the general MSSM. The breaking through gravity is one possibility, and is given by the minimal Supergravity model (mSUGRA) [3]. This theory is very appealing because it reduces the 124-dimensional parameter space of the MSSM to five dimensions. Since in mSUGRA an ideal candidate for cold dark matter can be predicted, also experimentalists use this model.

The start of the Large Hadron Collider (LHC) at CERN near Geneva is foreseen in the year 2007. In addition to searches for the Higgs boson, one of the main goals is to test the

predictions of prospective theories. If the MSSM describes nature, it is the aim to produce enough supersymmetric particles such that the two detectors CMS and ATLAS are able to discover them. After the discovery, it is important to measure their properties since these properties are necessary for distinguishing between different ways of Supersymmetry breaking. It is thus essential to determine the best methods for sparticle searches within the different models before the start of the LHC.

A short introduction into the principles of Supersymmetry is given in chapter 2. There the focus is set on the Minimal Supersymmetric Standard Model (MSSM), since it provides the simplest supersymmetric extension of the Standard Model being consistent with experiments. Furthermore, the mSUGRA model is introduced being one possible realisation of the MSSM and the framework in which this study has been carried out. The Monte Carlo generators used in this work are presented in chapter 3. In chapter 4, three important experiments concerning this study are presented. Part of the mSUGRA parameter space has been excluded due to limits on sparticle masses with the Large Electron Positron collider (LEP) at CERN. The Wilkinson Microwave Anisotropy Probe (WMAP), a NASA satellite, provides strong constraints for the cold dark matter density in the universe. In mSUGRA the $\tilde{\chi}_1^0$ is the lightest supersymmetric particle. Assuming the $\tilde{\chi}_1^0$ to be the candidate for cold dark matter, the parameter space can be further substantially reduced. In the future, the Large Hadron Collider (LHC) will be an ideal machine to search for Supersymmetry. Chapter 5 gives an introduction to the basic kinematics used in this analysis. The formulae and configurations for the kinematic endpoints are explained. Chapter 6 is the main chapter where the analysis methods and the results for $\tilde{\chi}_2^0$ searches at high $\tan\beta$ are presented. Many surveys have been made in several areas of the mSUGRA parameter space which are accessible at the LHC. It has been shown that the leptonic decay of the next-to-lightest neutralino,

$$\tilde{\chi}_2^0 \rightarrow l^\pm + \tilde{l}^\mp \rightarrow l^\pm + l^\mp + \tilde{\chi}_1^0 ,$$

has a useful kinematic feature: The dilepton invariant mass spectrum has a sharp edge near the kinematic upper limit. This feature was first discussed in [4]. If the decay into electrons and muons has a sufficient branching ratio, the endpoint can be measured very precisely, and therefore can be used for sparticle mass reconstructions. In some regions of the parameter space, however, the decay into taus dominates. At the benchmark point I' with $\tan\beta = 35$, $A_0 = 0$, $\mu > 0$, $m_0 = 181$ and $m_{1/2} = 350$ [5] 96% of all $\tilde{\chi}_2^0$ decays are into taus. Therefore, methods introduced for the dileptonic decay of the $\tilde{\chi}_2^0$ are applied to the tau channel. Since the endpoint is always smeared out due to the presence of neutrinos in the final states, the existence of a correlation between the different endpoints and the distribution maxima has been investigated. For distributions where the ratio between both values shows a linear dependence, the measurement precision can be improved. The single rho with the associated quark channel offers two endpoints which can be well estimated in most of the cases without knowing whether the corresponding tau comes from the slepton or the $\tilde{\chi}_2^0$. Additionally, it turned out that by using more endpoints than sparticle masses the determination of the sparticle masses can be improved significantly. The outlook in chapter 8 summarises problems and ideas which have not been treated in this work.

Chapter 2

Supersymmetry

The Standard Model successfully passed all particle physics experiments in the last 30 years. Especially the LEP and SLC experiments have tested its predictions with high precision. Indeed, there are experiments like the measurements of the anomalous magnetic moment of the muon in Brookhaven [6] and the WMAP measuring the cold dark matter density in our universe (see section 4.2) which may give a hint that physics beyond the Standard Model exists. But they do not exclude it. Thus, the motivation for introducing Supersymmetry is based on theoretical aspects.

In nature it is often possible to explain its principles and make predictions using symmetries. Since the discovery of the Pauli Principle, particles are divided in two groups, the fermions whose spin is an odd multiple of $\frac{1}{2}$ and the bosons with integer spin. A supersymmetric operation on the representation of a particle belonging to one group transforms it to a member of the other group. Thus, the spin changes but the mass and the couplings to other particles remain the same. The electron with spin $\frac{1}{2}$ and a mass of 0.511 MeV would have a bosonic partner with spin 0 and the same mass in a supersymmetric world. However, no supersymmetric partner has been discovered until now. It is therefore certain that - if Supersymmetry exists at a high energy scale - it is broken at the electroweak scale which is at the moment accessible for experiments.

2.1 MSSM

Particles and their interactions are described by Quantum Field Theories. The fundamental principles of nature are described through particles and their interactions whereas also the interactions are treated as particles in such theories. A quantum field is a complex n-dimensional function $\psi(x)$ representing one or more particles. $\psi(x)$ has the property that $|\psi(x)|^2$ gives the probability to find that particle at the space-time point x . Since only $|\psi(x)|^2$ is measurable, the phase of $\psi(x)$ is a free parameter. It is natural to assume that at any point in the universe the phase can be chosen differently without changing the particle's physical state:

$$\psi(x) \rightarrow e^{i\theta(x)}\psi(x). \quad (2.1)$$

This is the basis of all gauge theories like the Standard Model and its minimal supersymmetric extension. The direct consequence is that gauge bosons are responsible for the interactions between fermions. In the Standard Model the electroweak interactions result from a local $SU(2)_L \times U(1)_Y$ symmetry and the strong interactions from a local $SU(3)$ symmetry. The interactions within the MSSM are based on the same symmetries.

The MSSM is minimal in the sense that it is the simplest possible supersymmetric extension of the Standard Model with a minimal particle content. The MSSM has an additional second Higgs doublet, describes more than twice as many particles than the Standard Model and solves the following problems:

1. One of the main problems of the Standard Model is the *Hierarchy Problem*. The radiative corrections to the Higgs mass including the fermion loops at one-loop-level has a unphysical quadratic divergence. Indeed, this divergence can be canceled by a mass counter term which, however, has to be fine tuned at each order in perturbation theory. In the MSSM, two additional scalar particles S , provided they are in the region of 1 – 10 TeV, are responsible for the cancellation of that divergence. The remaining divergence is then only logarithmic, multiplied with $(m_S^2 - m_f^2)$ being zero in the supersymmetric limit.
2. Within the Standard Model, it is not possible to achieve a *unification of gauge couplings* - at any scale - which reduces the number of open parameters, and is therefore favoured by many theorists. The MSSM provides the possibility of gauge coupling unification at a scale of about 10^{16} GeV.
3. In some models within the MSSM there exists a *candidate for cold dark matter*. Experiments measuring the rotation velocities of galaxies have shown that it is very likely that there is more than just visible matter in our universe. One component of the so called dark matter seems to be cold, meaning that it consists of particles moving at a non-relativistic speed. Indeed, the Standard Model axion can be responsible for cold dark matter. But, it has not been discovered until now, and it is not clear whether it can explain the measured cold dark matter density sufficiently [7]. If mSUGRA is the model describing the Supersymmetry breaking in nature and if the lightest supersymmetric particle is a neutralino, it would be an excellent candidate for cold dark matter.
4. In the MSSM the mechanism of *electroweak symmetry breaking* occurs radiatively at the level of perturbation theory, without the need for any new strong interaction. Thus, in contrast to the SM the MSSM gives an explanation for the Higgs mechanism.

However, the MSSM gives neither a hint to the source of CP violation nor is it able to make predictions for any particle mass. Furthermore, the MSSM still is a theory without quantum gravity. String theories may solve some of these problems, although a phenomenologically viable string theory has yet to be constructed [8].

There are two different kinds of superfields in the Minimal Supersymmetric Standard Model at the GUT-scale and above:

1. The *Chiral Scalar Superfields* consisting of a complex scalar field, S , and a 2-component Majorana fermion field, ζ . The SM quarks and leptons and the MSSM higgsinos at the TeV-scale are connected with ζ and its partners, the squarks, sleptons and Higgses, with S .
2. The *Massless Vector Superfields* consisting of a gauge field $F_{\mu\nu}^A$ and a 2-component Majorana fermion field, λ_A . The field $F_{\mu\nu}^A$ is connected with the Standard Model gauge bosons and λ_A with its Superpartners, the gauginos, at the TeV-scale.

These fields respect the same $SU(3) \times SU(2)_L \times U(1)_Y$ gauge symmetries as do the Standard Model fields. In order to confirm or confute the predictions of the MSSM it is first necessary to find the new particles meaning to find the mass peaks of the mass eigenstates (Column *Mass* in Table 2.1). In the MSSM every supersymmetric particle has the same gauge couplings than its Standard Model partner. Thus, the second step would be to measure the interaction couplings and the spin of the new particles.

<i>MSSM Particles</i>					
Extended Standard Model			Supersymmetric Partners		
<i>Interaction</i>	<i>Mass</i>	<i>Spin</i>	<i>Interaction</i>	<i>Mass</i>	<i>Spin</i>
$e_{L/R}^{\pm}, \mu_{L/R}^{\pm}, \tau_{L/R}^{\pm}$	$e^{\pm}, \mu^{\pm}, \tau^{\pm}$	1/2	$\tilde{e}_{L/R}^{\pm}, \tilde{\mu}_{L/R}^{\pm}, \tilde{\tau}_{L/R}^{\pm}$	$\tilde{e}_{1/2}^{\pm}, \tilde{\mu}_{1/2}^{\pm}, \tilde{\tau}_{1/2}^{\pm}$	0
$\nu_e, \nu_{\mu}, \nu_{\tau}$	$\nu_e, \nu_{\mu}, \nu_{\tau}$	1/2	$\tilde{\nu}_e, \tilde{\nu}_{\mu}, \tilde{\nu}_{\tau}$	$\tilde{\nu}_e, \tilde{\nu}_{\mu}, \tilde{\nu}_{\tau}$	0
$u'_{L/R}, c'_{L/R}, t'_{L/R}$	u, c, t	1/2	$\tilde{u}'_{L/R}, \tilde{c}'_{L/R}, \tilde{t}'_{L/R}$	$\tilde{u}_{1/2}, \tilde{c}_{1/2}, \tilde{t}_{1/2}$	0
$d'_{L/R}, s'_{L/R}, b'_{L/R}$	d, s, b	1/2	$\tilde{d}'_{L/R}, \tilde{s}'_{L/R}, \tilde{b}'_{L/R}$	$\tilde{d}_{1/2}, \tilde{s}_{1/2}, \tilde{b}_{1/2}$	0
B^0, W^0	γ, Z^0	1	\tilde{B}^0, \tilde{W}^0	$\tilde{\chi}_1^0, \tilde{\chi}_2^0, \tilde{\chi}_3^0, \tilde{\chi}_4^0$	1/2
H_u^0, H_d^0	h, H, A^0, A^{\pm}	0	$\tilde{H}_u^0, \tilde{H}_d^0$		1/2
W^{\pm}	W^{\pm}	1	\tilde{W}^{\pm}	$\tilde{\chi}_1^{\pm}, \tilde{\chi}_2^{\pm}$	1/2
H^{\pm}	H^{\pm}	1	\tilde{H}^{\pm}		1/2
g	g	1	\tilde{g}	\tilde{g}	1/2

Table 2.1: This is the particle spectrum of the MSSM. The extended Standard Model has instead of only one an additional second Higgs doublet. The labels “L” and “R” denote the left- and right-handed electroweak eigenstates. The mass eigenstates $x_{1/2}$ are defined as $x_{1/2} = x_{L/R} \cdot \cos \theta \pm x_{R/L} \cdot \sin \theta$. Since θ is close to zero for electrons, muons, up, down, charmed and strange quarks, the mass eigenstates are mostly denoted with “L/R” instead of “1/2”, in the literature.

2.2 Superpotential and R-parity

In the SM, the effects due to the masses of quarks and leptons are parametrised by the Yukawa potential. The Yukawa couplings in the MSSM are specified by means of a function called superpotential. The general superpotential of the MSSM contains terms where the baryon and the lepton numbers are violated. These terms have significant experimental restrictions especially from measurements of the proton decay and the double beta decay. There are two ways to make the theory describing the data. First, the involved parameters can be tuned such that they are in accordance with experimental results. Alternatively, by introducing a new symmetry this problem is solved. This symmetry and its corresponding transformation is well explained in [8] and [9]. It leads to a multiplicative quantum number, the R-parity, which by convention is 1 for all Standard Model particles and -1 for their superpartners. It is given by

$$R = (-1)^{3(B-L)+2s} \quad (2.2)$$

for a particle with baryon number B, lepton number L and spin s. This symmetry has an important influence on the MSSM phenomenology since it requires that supersymmetric particles always are produced in pairs and that no supersymmetric particle can decay into solely Standard Model particles. In particular, the lightest supersymmetric particle is stable.

2.3 mSUGRA

In mSUGRA it is assumed that the three interactions are unified at the Grand Unification Theory (GUT) scale (10^{16} GeV) and that Supersymmetry is broken due to gravity. The beauty of mSUGRA lies in the fact that this model needs only four more parameters and the sign of a fifth additional parameter with respect to the known free parameters in the Standard Model. If mSUGRA describes the breaking of the Supersymmetry correctly, all scalar particles like sfermions and Higgs bosons have a common mass m_0 at the GUT scale. Also the gaugino

masses M_1 , M_2 and M_3 , corresponding to the U(1), SU(2) and SU(3) gauge symmetries, unify to a common mass $m_{1/2}$ at the GUT scale which can be seen in figure 2.1.

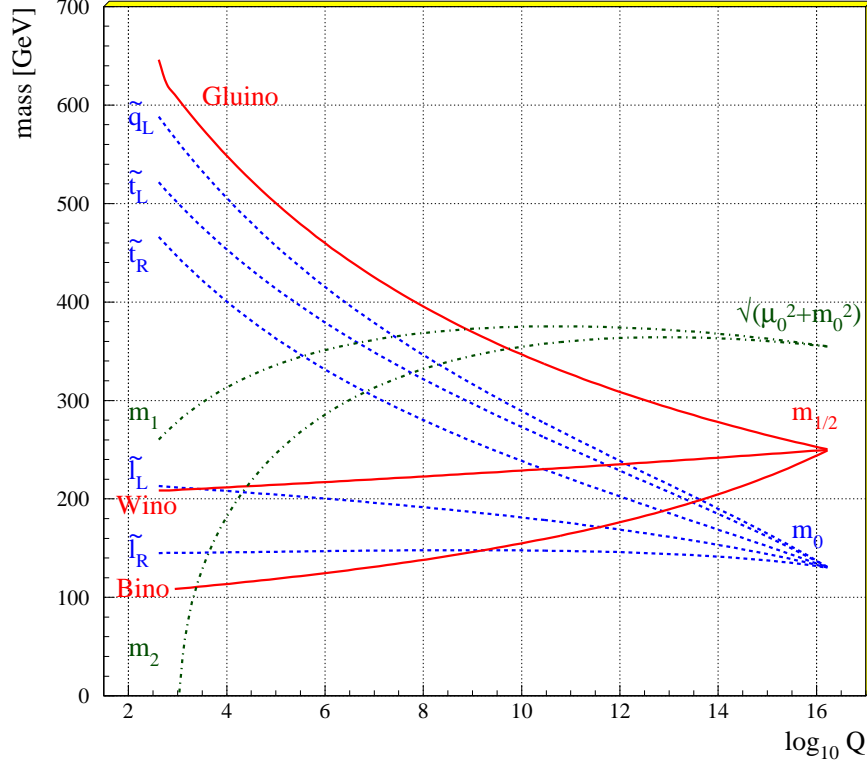


Figure 2.1: Evolution of the particle masses in mSUGRA through the Renormalisation Group equations (RNG) as a function of the energy scale. The mass spectrum is reduced to three distinct values at the GUT scale, whereas the particle spectrum at the experimentally accessible scale is split. In mSUGRA the gluino is always the heaviest gaugino.

All trilinear coupling parameters A_{ijk} have the same value A_0 at M_{GUT} , and the ratio of the vacuum expectation values of the two Higgs doublets is given by $\tan \beta$. The magnitude of the Higgsino mass parameter μ is given by the four mSUGRA parameters but its sign is the fifth open parameter. In mSUGRA with conserved R-parity (see section 2.2) the lightest supersymmetric particle (LSP) has to be stable. In some parts of the mSUGRA parameter space the $\tilde{\tau}_1^\pm$ is the LSP. However, a charged stable supersymmetric particle is cosmologically excluded. In other parts, the lightest neutralino is the LSP. This neutral weakly interacting particle is an ideal candidate for cold dark matter. If the latter is a concentration of lightest neutralinos, the WMAP data (see section 4.2), giving constraints on the cold dark matter density in the universe, can be used to restrict the mSUGRA parameter space. Very often, this restriction is shown in the $m_0 - m_{1/2}$ plane for different values of $\tan \beta$, A_0 and $\text{sign}(\mu)$.

One of the challenges of the LHC is to decide whether mSUGRA is the right theory for the description of nature. If this is the case, the next step will be to determine the values of the five parameters.

Chapter 3

Monte Carlo generators

At LHC, protons - which are made of quarks and gluons - will be accelerated to 7 TeV, and will collide at different interaction regions. These collisions will produce leptons together with quarks and gluons, both fragmenting into jets, in the final state. In most of the cases it is not possible to calculate analytically the Quantum Field theory based production cross sections and 4-momenta of particles produced in such collisions. Therefore, Monte Carlo generators, generally used for statistical models in science, are a useful tool for simulations in particle physics. In order to estimate the sensitivity of analysis methods, which will be utilised after having collected the first real data, simulations of proton-proton collisions at the LHC are necessary. Here, the first step is to generate quark-quark, quark-gluon and gluon-gluon collisions with a Monte Carlo generator. The particle distribution functions which describe how the quarks and gluons are distributed within the protons are measured at HERA and by other experiments. The choice of the special Monte Carlo generator depends on the physics model for which sensitivity studies are made. The output at this level are the precise 4-momenta of all particles in such an event. Then detector effects and effects due to event reconstruction have to be included.

3.1 ISASUGRA

In this study ISASUGRA 7.69 is used which is part of ISAJET 7.69 [10]. It calculates numerically the masses, the branching ratios and the weak-scale mass parameters within the mSUGRA model. The particle spectrum calculated by ISASUGRA can be used as an input for PYTHIA [11]. The cross sections are evaluated by ISAJET or PYTHIA. ISASUGRA takes the following values as input: The choice of the mSUGRA parameters and the top mass. The top mass is set to 175 GeV in this study which is the same value used by most of the recent publications of mSUGRA studies. Presently, the updated value is 174.3 ± 5.1 GeV [12]. Furthermore, A_0 is set to zero, μ is positive and the value for $\tan \beta$ is 35. The values for m_0 and $m_{1/2}$ and the motivation for the parameter choice are given in chapter 6.

3.2 PYTHIA

PYTHIA is a program for the Monte Carlo generation of high energy physics events arising from collisions between elementary particles such as e^+ , e^- , p and \bar{p} in various combinations. It is based on theories and models for a number of physics processes, including hard and soft interactions, parton distributions, initial and final state parton showers, multiple interactions, fragmentation and decay. The version used in this study is the corrected (See appendix A.1) version of PYTHIA 6.220. In PYTHIA it is possible to include new particles, cross sections, processes, and also to specify the decays of particles. In order to save CPU time, the taus in this study have been forced to decay solely into charged rhos. The production cross section calculated by PYTHIA did not change, with respect to the cross section with all tau channels included,

due to that adjustment (See appendix A.4). Therefore, in order to normalise all distributions to 30 fb^{-1} , the PYTHIA 6.220 branching ratio of 24.9 % for $\tau^\pm \rightarrow \rho^\pm \nu_\tau$ has to be included. In this study an event is defined as one produced $\tilde{\chi}_2^0$ decaying into two τ . Thus, the number of produced events has been multiplied by the squared branching ratio.

Chapter 4

Experiments

4.1 Large Electron Positron Collider

The operation of the Large Electron Positron (LEP) collider at CERN started in August 1989. With a circumference of 27 km, LEP was the largest accelerator in the world. It stopped in November 2000, but the analysis of data is still going on. LEP accelerated electrons and positrons - in opposite directions in a vacuum pipe inside a retaining ring of magnets - which collided head-on at different interaction points. The four LEP experiments were called ALEPH, DELPHI, L3 and OPAL.

The MSSM predicts a light Higgs with $M_{h^0} \leq 130$ GeV, and with LEP a lower constraint of $M_{h^0} \geq 114$ GeV was obtained. In some parts of the mSUGRA parameter space, especially for low values of m_0 and $m_{1/2}$, LEP should have produced enough supersymmetric particles necessary for a discovery. However, there was no evidence for Supersymmetry at LEP. Thus, a value for $\tan\beta$ lower than 2.4 has been excluded [13]. The LEP Susy Working Group has obtained preliminary results which are shown in figure 4.1 and 4.2. These results are based on

1. a combination of $E_{CM} = 183 - 208$ GeV ALEPH, DELPHI, L3 and OPAL searches for pair production of \tilde{e} in the $\tilde{e} \rightarrow e\tilde{\chi}_1^0$ channel,
2. a combination of $E_{CM} = 183 - 208$ GeV ALEPH, DELPHI, L3 and OPAL searches for pair production of $\tilde{\tau}$ in the $\tilde{\tau} \rightarrow \tau\tilde{\chi}_1^0$ channel,
3. a combination of the $E_{CM} = 205 - 208$ GeV ALEPH, L3 and OPAL searches for pair production of $\tilde{\chi}_1^\pm$,
4. the $E_{CM} \leq 202$ GeV ALEPH searches for pair production of heavy stable charged particles,
5. the DELPHI and ALEPH searches for neutralinos decaying into $\tilde{\tau}$ and τ ,
6. a combination of $E_{CM} < 209$ GeV ALEPH, DELPHI, L3 and OPAL searches for the lightest scalar neutral Higgs in the $ee \rightarrow hZ$ reaction.

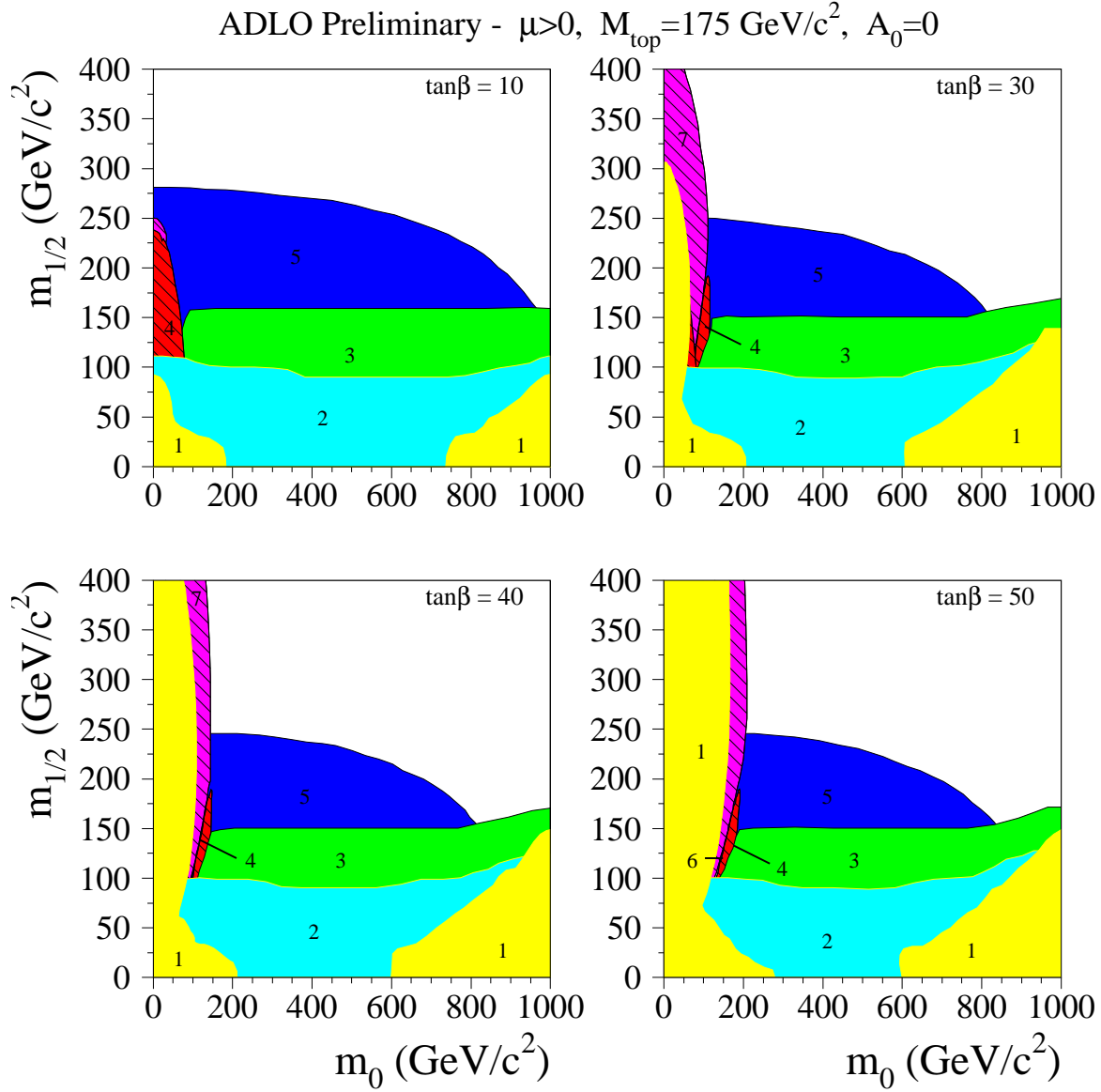


Figure 4.1: The excluded regions in the m_0 - $m_{1/2}$ -plane through measurements with LEP for $\mu > 0$ and $A_0 = 0$. Yellow (1): no mSUGRA solution: no EWSB or tachyonic particles; Light blue (2): regions inconsistent with the measurement of the electroweak parameters at LEP1; Green (3): regions excluded by chargino searches; Red (4): regions excluded by selectron or stau standard searches; Dark Blue (5): regions excluded by the search for hZ ; Brown (6): regions excluded by the neutralino stau cascade searches. Magenta (7): regions excluded by the search for heavy stable charged particles applied to staus [14].

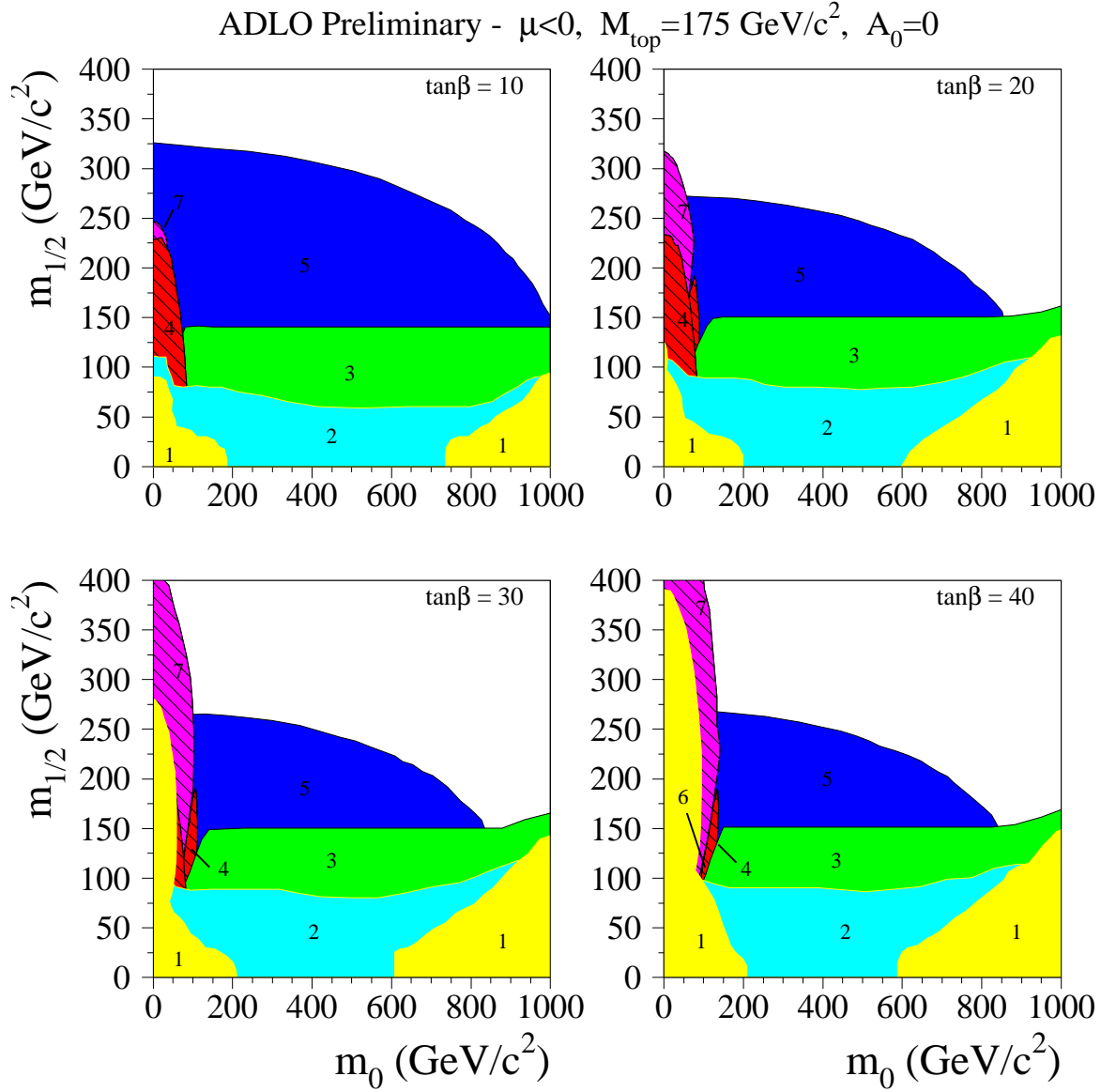


Figure 4.2: The excluded regions in the m_0 - $m_{1/2}$ -plane through measurements with LEP for $\mu < 0$ and $A_0 = 0$. Yellow (1): no mSUGRA solution: no EWSB or tachyonic particles; Light blue (2): regions inconsistent with the measurement of the electroweak parameters at LEP1; Green (3): regions excluded by chargino searches; Red (4): regions excluded by selectron or stau standard searches; Dark Blue (5): regions excluded by the search for hZ ; Brown (6): regions excluded by the neutralino stau cascade searches. Magenta (7): regions excluded by the search for heavy stable charged particles applied to staus [14].

4.2 Wilkinson Microwave Anisotropy Probe

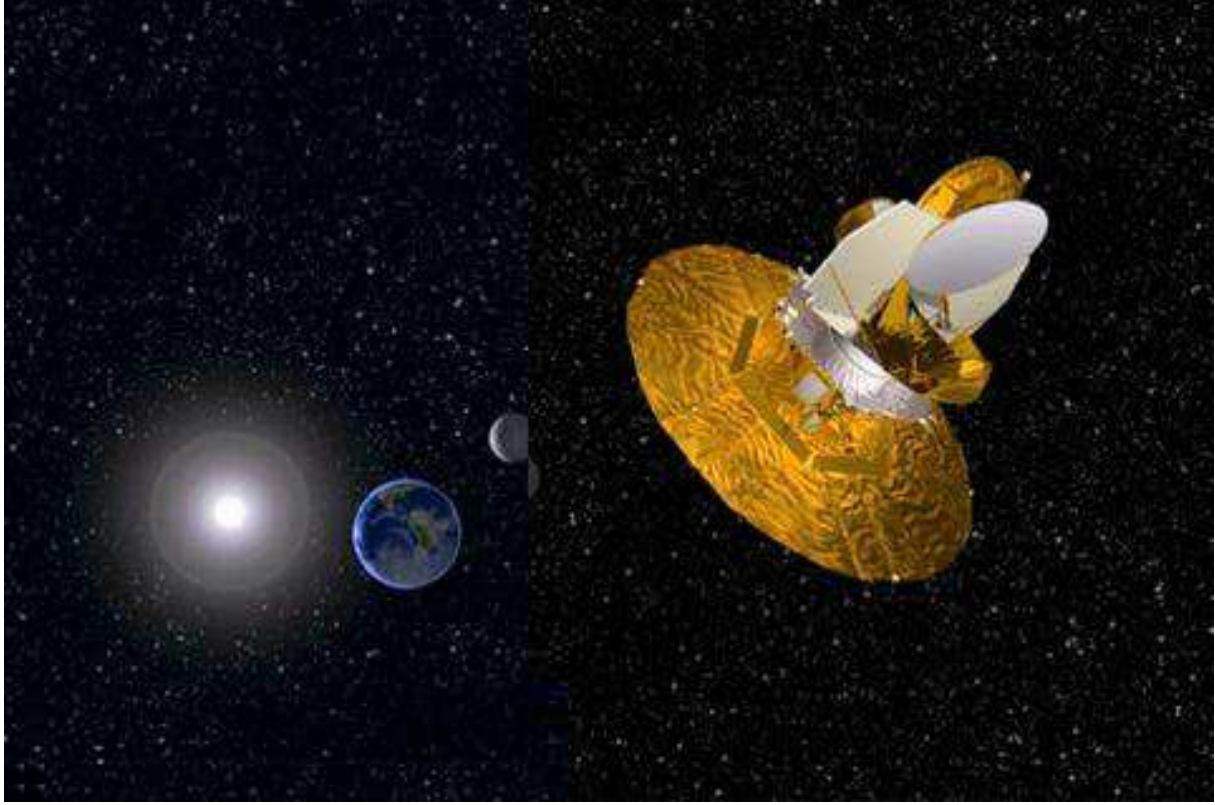


Figure 4.3: A view of the WMAP satellite in the universe [15].

The cosmic microwave background (CMB) radiation is the radiant heat left over from the Big Bang. It was first observed in 1965 by Arno Penzias and Robert Wilson at the Bell Telephone Laboratories in Murray Hill, New Jersey [16]. The properties of the radiation give information about the physical conditions in the early universe, and can therefore be used for a better understanding of the formation of cosmic structures such as galaxies and dark matter. As a consequence, assuming that cold dark matter is made of neutralinos, the CMB radiation data leads to restrictions on the allowed mSUGRA parameters. Thus, this data is important for making constraints on the mSUGRA parameter space.

If the $\tilde{\chi}_1^0$ were abundantly produced directly after the Big Bang they would have had mostly annihilated to the relic density which has been measured with WMAP. In neutralino relic density calculations for mSUGRA there is a 'bulk' region of relatively low values of $m_{1/2}$ and m_0 , where neutralinos annihilate dominantly through t-channel slepton exchange ($\tilde{\chi}_1^0 \tilde{\chi}_1^0 \rightarrow l \bar{l}$). For a large neutralino mass, the relic density is generally large. However, neutralino-stau coannihilation ($\tilde{\chi}_1^0 \tilde{\tau} \rightarrow \tau V$) can reduce the relic density to satisfy the cosmologically favored relic density bounds. The region where this is possible ($M_{\tilde{\tau}} - M_{\tilde{\chi}_1^0} \ll M_{\tilde{\chi}_1^0}$) has a highly fine-tuned relic density since a small variation in m_0 would lead to a large change in $\Omega_{LSP} h^2$. Furthermore, there is a region where rapid annihilation through s-channel Higgs boson resonances ($\tilde{\chi}_1^0 \tilde{\chi}_1^0 \rightarrow H \rightarrow b\bar{b}, \tau\bar{\tau}$) can reduce the neutralino relic density to the measured region. Finally, in the focus point region at large m_0 - where the $\tilde{\chi}_1^0$ is Higgsino like - the relic density is achieved mainly through the $\tilde{\chi}_1^0 \tilde{\chi}_1^0 \rightarrow W^+ W^-$ and the $\tilde{\chi}_1^0 \tilde{\chi}_1^0 \rightarrow Z Z$ channels.

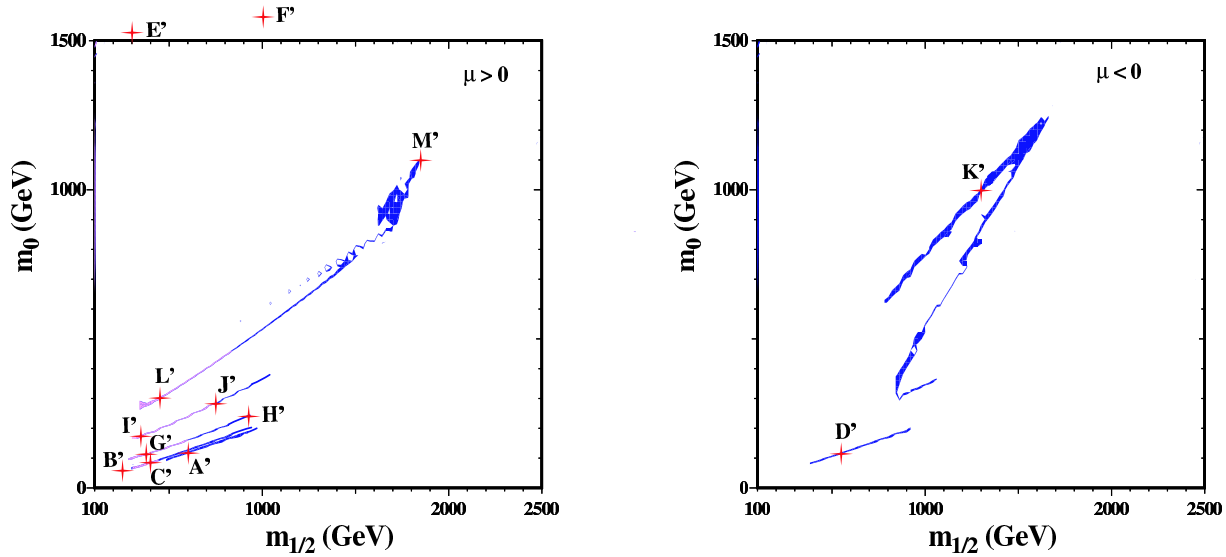


Figure 4.4: The shaded strips display the regions of the $(m_{1/2}, m_0)$ plane that are compatible with $0.094 < \Omega_{LSP} h^2 < 0.129$ at the $2\text{-}\sigma$ level where $\Omega_{LSP} h^2$ is the normalised density. These areas are in the bulk (B', C', G', I', L'), coannihilation tail (A', D', H', J') and rapid-annihilation funnel (K', M') regions. Left plot: $\mu > 0$ and $\tan \beta = 5$ (A'), 10 (B', C'), 20 (G', H'), 35 (I', J') and 50 (L', M'). Right plot: $\mu < 0$ and $\tan \beta = 10$ (D') and 35 (K'). The parts of these WMAP lines for $\mu > 0$ compatible with the $g_\mu-2$ measurements at BNL [17] at the $2\text{-}\sigma$ level have lighter (pink) shading [5].

The Wilkinson Microwave Anisotropy Probe (WMAP), shown in figure 4.3, is a NASA satellite, and presently the best experiment to measure the CMB radiation and its spatial fluctuations. Launched in 2001, WMAP is now able to resolve small temperature fluctuations of the order of only millionths of a degree. Instead of measuring the absolute temperature values of the CMB radiation WMAP measures the temperature differences between two different points in the sky, taking advantage of the higher accuracy of differential measurements. Figure 4.4 shows that the region in the two-dimensional $m_{1/2}-m_0$ plane consistent with experimental data is reduced to nearly one dimensional strips due to the WMAP measurements. Therefore, the WMAP experiment gives a hint where we have to focus the searches for mSUGRA.

4.3 Large Hadron Collider

This study concerns physical processes that might happen at the Large Hadron Collider (LHC). The construction of the LHC has been approved by the CERN's Council in December 1994. The LHC, shown in figure 4.5, is the successor of the Large Electron Positron collider (LEP), and will be installed in the 27 kilometre circumference LEP tunnel being about 100 metre underground. The LHC will operate at a center-of-mass energy \sqrt{s} of 14 TeV being the highest ever reached in the world. The design luminosity is $2.3 \cdot 10^{34} \text{ cm}^{-2} \text{ s}^{-1}$. Furthermore, lead-ion collisions are planned with a total \sqrt{s} of 1148 TeV and a luminosity of $1.0 \cdot 10^{27} \text{ cm}^{-2} \text{ s}^{-1}$. The accelerator consists of two interleaved synchrotron rings, whose main elements are 1232 superconducting NbTi dipole and 392 quadrupole magnets operating in superfluid helium at a temperature of 1.9 K. The dipole magnets guide the particles along the ring while the quadrupole magnets are focusing the particle bunches. The nominal field for LHC magnets to handle 7 TeV beams is 8.34 Tesla, and the goal is to achieve 9.0 Tesla [19]. Two 450 GeV beams coming from

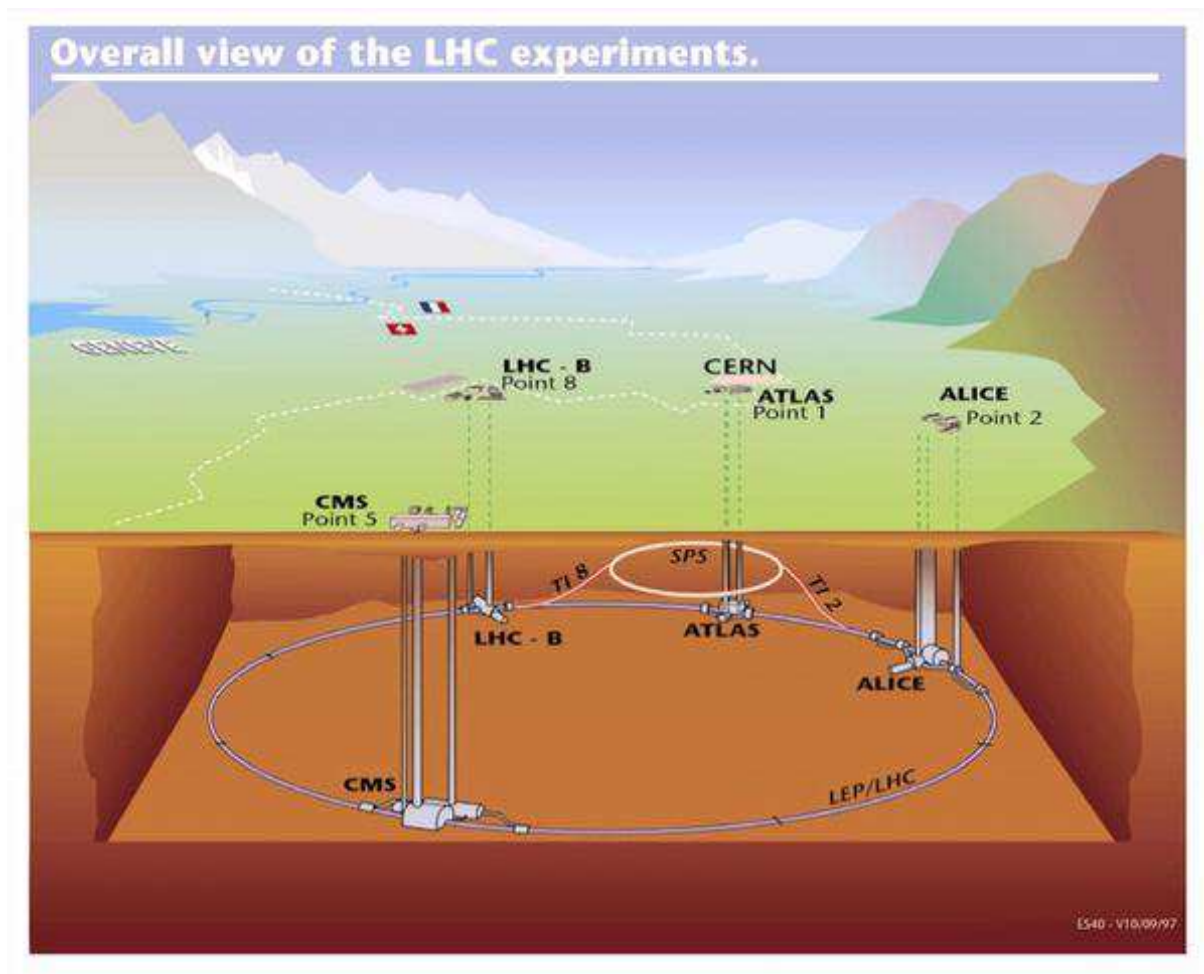


Figure 4.5: A schematic view of the LHC at CERN near Geneva [18].

the Super Proton Synchrotron (SPS) will be injected into the LHC, and then accelerated with superconducting cavities, 8 cavities per ring, operating at 2 MV and 400 MHz.

The experimental program of the LHC will include the dedicated heavy-ion detector ALICE (A Large Ion Collider Experiment), the specialised B-physics spectrometer LHCb and the general purpose detectors CMS (Compact Muon Solenoid) and ATLAS (A Toroidal LHC ApparatuS). The physics goals of CMS (Figure 4.6) and ATLAS include searches for the Higgs boson, which is predicted by the Standard Model, as well as for supersymmetric particles which appear in Supersymmetry theories like mSUGRA or the Gauge Mediated Susy Breaking (GMSB) scenario. If the latter particles exist they will be produced mainly through squark or gluino production at LHC. These processes can lead to long decay chains which allow to give constraints for all involved sparticle masses.

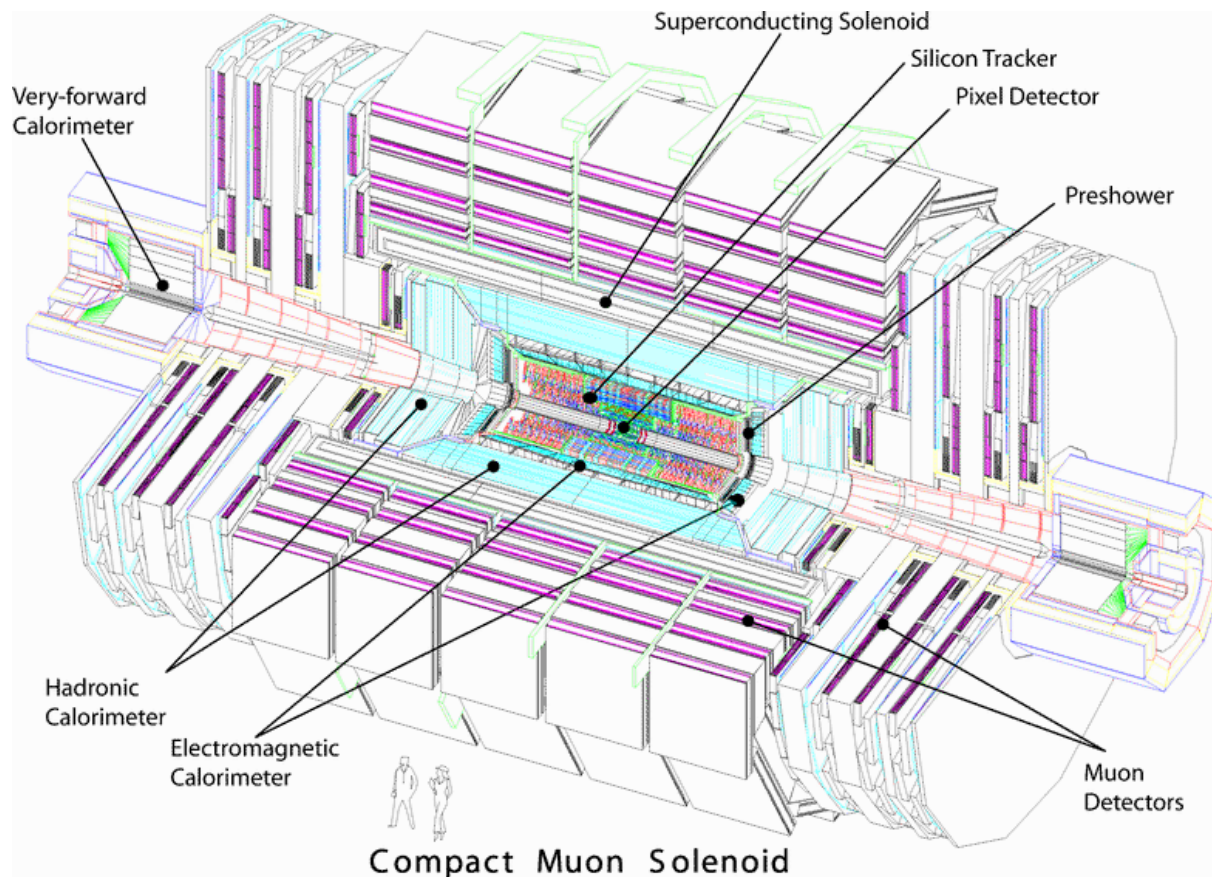


Figure 4.6: A schematic view of the CMS detector. The pixel detector is closest to the interaction vertex. The second innermost detector is the silicon tracker followed by the crystal electromagnetic calorimeter and the hadronic calorimeter. Outside of the superconducting solenoid which generates a magnetic field of 4 Tesla there are the muon chambers. The total weight is 12500 T which is nearly twice as much as the weight of the Tour Eiffel.

Chapter 5

Kinematics for $\tilde{\chi}_2^0$ searches

At the Large Hadron Collider the colliding parton's center of mass and exact center of mass energy is not known. Therefore, it is sensible to concentrate on Lorentz invariant quantities like the invariant mass. The invariant mass of n particles with energy E_i and 3-momentum p_i is frame independent, and given by

$$M^2 = \left(\sum_{i=1}^n E_i \right)^2 - \left(\sum_{i=1}^n p_i \right)^2 \quad (5.1)$$

The lowest limit of M is in any case the sum of all n particle rest frame masses. If there is no external force the invariant mass of a system of particles does not change, even if some particles decay or annihilate. In the following calculations the speed of light c and Planck's constant \hbar are set to one.

Invariant mass distributions carry information about the particles at the end of a decay chain as well as about the decaying particles. For this study, the kinematic formulae and configurations presented in this chapter are relevant. In general it is necessary to distinguish between massive and massless particles. If the energy of a particle is a few magnitudes higher than its mass, it is a good estimation to treat it as massless. Therefore, in the following calculations [20] all Standard Model quarks and leptons - except the top quark in section 5.3 - are chosen to be massless. In the Monte Carlo simulations, however, the correct masses are taken into account.

5.1 Sequential two-body decays

Only two-body decays have to be taken into account for the processes in this study. In the two-body decay of a particle M into m_1 and m_2 , the energy, E_i^* , and 3-momentum, p_i^* , in the rest frame of M , which is denoted with a “*”, are given by

$$M = E_1^* + E_2^*, \quad |p_1^*| = |p_2^*| = p^*. \quad (5.2)$$

Squaring the first equation gives

$$2E_1^*E_2^* = M^2 - m_1^2 - m_2^2 - 2p^{*2}.$$

Squaring again and extracting p^* leads to

$$\begin{aligned} p^{*2} &= \frac{1}{4M^2} [(M^2 - m_1^2 - m_2^2)^2 - 4m_1^2m_2^2] \\ &= \frac{1}{4M^2} [M^4 - 2M^2(m_1^2 + m_2^2) + (m_1^2 - m_2^2)^2] \\ &= \frac{1}{4M^2} [M^2 - (m_1 + m_2)^2][M^2 - (m_1 - m_2)^2]. \end{aligned}$$

The energy becomes

$$\begin{aligned}
E_1^{*2} &= p^{*2} + m_1^2 \\
&= \frac{1}{4M^2} [M^4 - 2M^2(m_1^2 + m_2^2) + (m_1^2 - m_2^2)^2 + 4M^2 m_1^2] \\
&= \frac{1}{4M^2} [M^2 + m_1^2 - m_2^2]^2.
\end{aligned}$$

In summary:

$$E_1^* = \frac{M^2 + m_1^2 - m_2^2}{2M} \quad (5.3)$$

$$|p_1^*| = |p_2^*| = \frac{[(M^2 - (m_1 + m_2)^2)(M^2 - (m_1 - m_2)^2)]^{1/2}}{2M} \quad (5.4)$$

The formulae are considerably simplified if one of the decay particles is massless. Assuming that $m_2 = 0$ one obtains:

$$E_1^* = \frac{M^2 + m_1^2}{2M}, \quad E_2^* = \frac{M^2 - m_1^2}{2M}, \quad |p_1^*| = |p_2^*| = \frac{M^2 - m_1^2}{2M}. \quad (5.5)$$

The transformation from the rest frame of M to the lab system is defined by two kinematic variables of M , the velocity $\beta = q/E$ and $\gamma = E/M$, where q and E are the lab frame momentum and energy of M . The Lorentz transformation to the lab system is most easily decomposed into a longitudinal and a transverse part:

$$\begin{aligned}
E_i &= \gamma [E_i^* + \beta p^* \cos \theta_i^*] \\
p_{Ti} &= p_{Ti}^* = p^* \sin \theta_i^* \\
p_{Li} &= \gamma [\beta E_i^* + p^* \cos \theta_i^*]
\end{aligned} \quad (5.6)$$

with $\theta_2^* = \theta_1^* + \pi$. The maximum and minimum values of E_i and p_{Li} are obtained for $\cos \theta_i^* = +1$ and -1 respectively.

The investigated leptonic $\tilde{\chi}_2^0$ decay chain in the analysis presented here is

$$\tilde{\chi}_2^0 \rightarrow \tilde{l}^\pm + l^\mp, \quad \tilde{l}^\pm \rightarrow \tilde{\chi}_1^0 + l^\pm. \quad (5.7)$$

The calculations are valid for taus as well as for other leptons l , which are assumed to be massless. Moreover, maxima and minima of effective masses correspond to collinear configurations, where the particles are emitted along or opposite to the direction of the Lorentz boost. In this case,

$$E_{l2} = \gamma E_{l2}^* (1 \pm \beta). \quad (5.8)$$

As the Lorentz transformation parameters are

$$\beta = \frac{M_{\tilde{\chi}_2^0}^2 - M_l^2}{M_{\tilde{\chi}_2^0}^2 + M_l^2}, \quad \gamma = \frac{M_{\tilde{\chi}_2^0}^2 + M_l^2}{2M_{\tilde{\chi}_2^0} M_l}, \quad (5.9)$$

this yields to

$$\gamma (1 \pm \beta) = \frac{1}{2M_{\tilde{\chi}_2^0} M_l} [(M_{\tilde{\chi}_2^0}^2 + M_l^2) \pm (M_{\tilde{\chi}_2^0}^2 - M_l^2)] \quad (5.10)$$

so that the maximum energies associated with the boost direction and minimum energies associated with the opposite-to-the-boost direction are:

$$E_{l2}^{max} = \frac{M_{\tilde{\chi}_2^0}}{M_l} E_{l2}^*, \quad E_{l2}^{min} = \frac{M_l}{M_{\tilde{\chi}_2^0}} E_{l2}^*. \quad (5.11)$$

Similarly, for the momentum with the sign being measured in the boost direction it is

$$p_{l2} = \gamma E_{l2}^* (\beta \pm 1) \quad (5.12)$$

leading to

$$p_{l2}^{max} = E_{l2}^{max}, \quad p_{l2}^{min} = -E_{l2}^{min}. \quad (5.13)$$

These expressions considerably simplify the later calculations. In the following the kinematic limit for both leptons is calculated. The effective mass can be computed in the rest frame of $\tilde{\chi}_2^0$. The z-axis is chosen along the direction of the slepton, as depicted on figure 5.1.

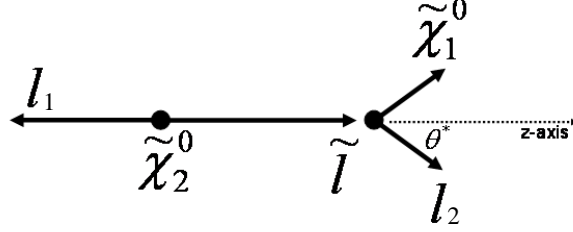


Figure 5.1: Kinematics of the χ_2^0 decay via a slepton \tilde{l} .

The dileptonic effective mass is given by

$$\begin{aligned} M_{ll}^2 &= (E_{l1} + E_{l2})^2 - (-p_{l1} + p_{Ll2})^2 - (0 + p_{Tl2})^2 \\ &= 2E_{l1}E_{l2} + 2p_{l1}p_{Ll2} = 2E_{l1}(E_{l2} + p_{Ll2}) \end{aligned} \quad (5.14)$$

where the indices L and T denote the longitudinal and transverse components. As particle $l1$ is massless, the energy and momentum of $l1$ and \tilde{l} are given by the expressions (5.5) and similarly for particle $l2$ in the rest frame of \tilde{l} .

$$E_{l2}^* = |p_{l2}^*| = \frac{M_{\tilde{l}}^2 - M_{\tilde{\chi}_1^0}^2}{2M_{\tilde{l}}} \quad (5.15)$$

The Lorentz transformation of the massless particle $l2$ into the rest frame of $\tilde{\chi}_2^0$ becomes

$$\begin{aligned} E_{l2} &= \gamma E_{l2}^* (1 + \beta \cos \theta^*) \\ p_{Ll2} &= \gamma E_{l2}^* (\beta + \cos \theta^*) \end{aligned} \quad (5.16)$$

from which

$$\begin{aligned} E_{l2} + p_{Ll2} &= \gamma E_{l2}^* (1 + \beta)(1 + \cos \theta^*) \\ &= \frac{M_{\tilde{\chi}_2^0}^2}{2M_{\tilde{l}}} (M_{\tilde{l}}^2 - M_{\tilde{\chi}_1^0}^2) (1 + \cos \theta^*). \end{aligned} \quad (5.17)$$

The effective mass then takes the simple expression

$$\begin{aligned} M_{ll}^2 &= 2 \frac{M_{\tilde{\chi}_2^0}^2 - M_{\tilde{l}}^2}{2M_{\tilde{\chi}_2^0}} \frac{M_{\tilde{\chi}_2^0}^2}{2M_{\tilde{l}}} (M_{\tilde{l}}^2 - M_{\tilde{\chi}_1^0}^2) (1 + \cos \theta^*) \\ &= \frac{(M_{\tilde{\chi}_2^0}^2 - M_{\tilde{l}}^2)(M_{\tilde{l}}^2 - M_{\tilde{\chi}_1^0}^2)}{2M_{\tilde{l}}^2} (1 + \cos \theta^*) \end{aligned} \quad (5.18)$$

with the upper endpoint of the mass distribution given by

$$M_{ll}^{max} = M_{\tilde{\chi}_2^0} \sqrt{\left(1 - \frac{M_{\tilde{l}}^2}{M_{\tilde{\chi}_2^0}^2}\right) \left(1 - \frac{M_{\tilde{\chi}_1^0}^2}{M_{\tilde{l}}^2}\right)}. \quad (5.19)$$

This corresponds to the configuration where the two leptons are emitted back-to-back in the rest frame of the $\tilde{\chi}_2^0$. Since the \tilde{l} is a particle with spin 0 it should decay isotropically. Thus, formula (5.18) shows that the distribution in M_{ll} increases linearly with M_{ll} leading to a sharp edge at the kinematic limit given by formula (5.19).

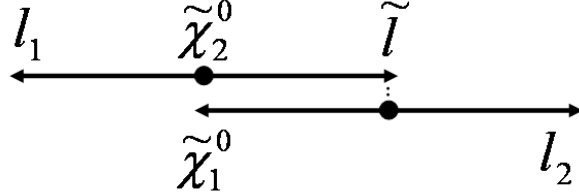
The following section shows a summary of all formulae for the endpoints which are used in the analysis and the related configurations. They are calculated in the same way as described above.

5.2 Formulae and kinematic configurations

Here the endpoints available for the decay chain $\tilde{q} \rightarrow q + \tilde{\chi}_2^0$, $\tilde{\chi}_2^0 \rightarrow l1 + \tilde{l}$, $\tilde{l} \rightarrow l2 + \tilde{\chi}_1^0$ are summarized.

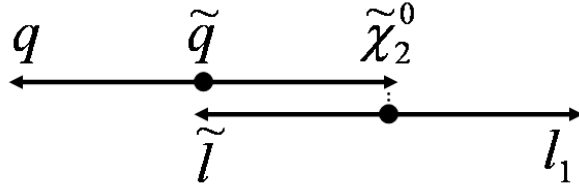
1. M_{ll}^{max}

$$M_{ll}^{max} = M_{\tilde{\chi}_2^0} \sqrt{\left(1 - \frac{M_{\tilde{l}}^2}{M_{\tilde{\chi}_2^0}^2}\right) \left(1 - \frac{M_{\tilde{\chi}_1^0}^2}{M_{\tilde{l}}^2}\right)} \quad (5.20)$$



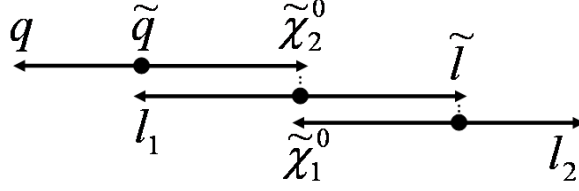
2. M_{l1q}^{max} (1st lepton)

$$M_{l1q}^{max} = M_{\tilde{q}} \sqrt{\left(1 - \frac{M_{\tilde{\chi}_2^0}^2}{M_{\tilde{q}}^2}\right) \left(1 - \frac{M_{\tilde{l}}^2}{M_{\tilde{\chi}_2^0}^2}\right)} \quad (5.21)$$



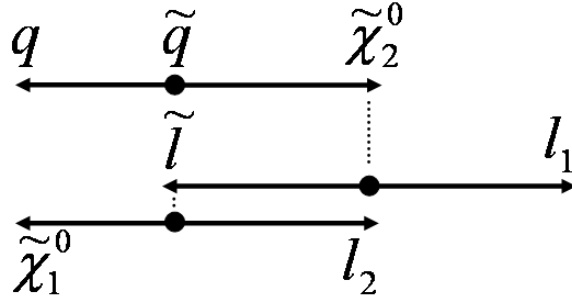
3. $\mathbf{M}_{\mathbf{l2q}}^{\mathbf{max}}$ (2nd lepton)

$$M_{l_2q}^{max} = M_{\tilde{q}} \sqrt{\left(1 - \frac{M_{\tilde{\chi}_2^0}^2}{M_{\tilde{q}}^2}\right) \left(1 - \frac{M_{\tilde{\chi}_1^0}^2}{M_l^2}\right)} \quad (5.22)$$



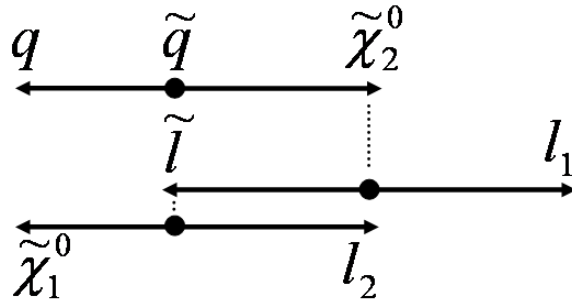
4. $\mathbf{M}_{\mathbf{llq}}^{\mathbf{max}}$, for $M_{\tilde{\chi}_2^0}^2 < M_{\tilde{q}} M_{\tilde{\chi}_1^0}$

$$M_{llq}^{max} = M_{\tilde{q}} \sqrt{\left(1 - \frac{M_{\tilde{\chi}_2^0}^2}{M_{\tilde{q}}^2}\right) \left(1 - \frac{M_{\tilde{\chi}_1^0}^2}{M_{\tilde{\chi}_2^0}^2}\right)} \quad (5.23)$$



5. $(\mathbf{M}_{\mathbf{l1q}} + \mathbf{M}_{\mathbf{l2q}})^{\mathbf{max}}$

$$M_{l_1q+l_2q}^{max} = M_{l_1q}^{max} + \frac{M_{\tilde{l}}}{M_{\tilde{\chi}_2^0}} M_{l_2q}^{max} \quad (5.24)$$



Four of these five endpoints are in principle necessary to determine all involved masses, provided that several consecutive decay channels are open (long decay chains). However, it will not always be possible to measure them precisely. Therefore, it will be sensible to use all available endpoints.

5.3 Endpoints for top quark events

The mass of the top quark is very large and therefore not negligible. Thus, not only upper endpoints but also lower endpoints arise in the invariant mass distributions. In the analysis presented in section 6.2.13 to 6.2.15 the top quark is involved. The corresponding decay chain is

$$\tilde{t} \rightarrow t + \tilde{\chi}_2^0 \rightarrow t + \tilde{l} + l \rightarrow t + l + l + \tilde{\chi}_1^0. \quad (5.25)$$

With

$$E_t = \frac{M_{\tilde{t}}^2 + m_t^2 - M_{\tilde{\chi}_2^0}^2}{2M_{\tilde{t}}} \quad , \quad p_t = \sqrt{E_t^2 - m_t^2} \quad (5.26)$$

$$E_{\tilde{\chi}_2^0} = \frac{M_{\tilde{t}}^2 + M_{\tilde{\chi}_2^0}^2 - m_t^2}{2M_{\tilde{t}}} \quad , \quad p_{\tilde{\chi}_2^0} = \sqrt{E_{\tilde{\chi}_2^0}^2 - M_{\tilde{\chi}_2^0}^2} \quad (5.27)$$

the endpoint formulae are the following:

$$(M_{l1t}^{max})^2 = m_t^2 + M_{\tilde{t}}^2 \left(1 - \frac{M_{\tilde{\chi}_2^0}^2}{M_{\tilde{t}}^2} + \frac{m_t^2}{M_{\tilde{t}}^2}\right) \left(1 - \frac{M_{\tilde{l}}^2}{M_{\tilde{\chi}_2^0}^2}\right) \frac{E_{\tilde{\chi}_2^0} + p_{\tilde{\chi}_2^0}}{M_{\tilde{t}}} \times \frac{1}{2} \left(1 + \sqrt{1 - \left(\frac{m_t}{E_t}\right)^2}\right) \quad (5.28)$$

$$(M_{l1t}^{min})^2 = m_t^2 + M_{\tilde{t}}^2 \left(1 - \frac{M_{\tilde{\chi}_2^0}^2}{M_{\tilde{t}}^2} + \frac{m_t^2}{M_{\tilde{t}}^2}\right) \left(1 - \frac{M_{\tilde{l}}^2}{M_{\tilde{\chi}_2^0}^2}\right) \frac{E_{\tilde{\chi}_2^0} - p_{\tilde{\chi}_2^0}}{M_{\tilde{t}}} \times \frac{1}{2} \left(1 - \sqrt{1 - \left(\frac{m_t}{E_t}\right)^2}\right) \quad (5.29)$$

$$(M_{l2t}^{max})^2 = m_t^2 + M_{\tilde{t}}^2 \left(1 - \frac{M_{\tilde{\chi}_2^0}^2}{M_{\tilde{t}}^2} + \frac{m_t^2}{M_{\tilde{t}}^2}\right) \left(1 - \frac{M_{\tilde{\chi}_1^0}^2}{M_{\tilde{l}}^2}\right) \frac{E_{\tilde{\chi}_2^0} + p_{\tilde{\chi}_2^0}}{M_{\tilde{t}}} \times \frac{1}{2} \left(1 + \sqrt{1 - \left(\frac{m_t}{E_t}\right)^2}\right) \quad (5.30)$$

$$(M_{l2t}^{min})^2 = m_t^2 + M_{\tilde{t}}^2 \left(1 - \frac{M_{\tilde{\chi}_2^0}^2}{M_{\tilde{t}}^2} + \frac{m_t^2}{M_{\tilde{t}}^2}\right) \frac{M_{\tilde{l}}^2}{M_{\tilde{\chi}_2^0}^2} \left(1 - \frac{M_{\tilde{\chi}_1^0}^2}{M_{\tilde{l}}^2}\right) \frac{E_{\tilde{\chi}_2^0} - p_{\tilde{\chi}_2^0}}{M_{\tilde{t}}} \times \frac{1}{2} \left(1 - \sqrt{1 - \left(\frac{m_t}{E_t}\right)^2}\right) \quad (5.31)$$

$$(M_{llt}^{max})^2 = m_t^2 + M_{\tilde{t}}^2 \left(1 - \frac{M_{\tilde{\chi}_2^0}^2}{M_{\tilde{t}}^2} + \frac{m_t^2}{M_{\tilde{t}}^2}\right) \left(1 - \frac{M_{\tilde{\chi}_1^0}^2}{M_{\tilde{\chi}_2^0}^2}\right) \frac{E_{\tilde{\chi}_2^0} + p_{\tilde{\chi}_2^0}}{M_{\tilde{t}}} \times \frac{1}{2} \left(1 + \sqrt{1 - \left(\frac{m_t}{E_t}\right)^2}\right) \quad (5.32)$$

$$(M_{llt}^{min})^2 = m_t^2 + M_{\tilde{t}}^2 \left(1 - \frac{M_{\tilde{\chi}_2^0}^2}{M_{\tilde{t}}^2} + \frac{m_t^2}{M_{\tilde{t}}^2}\right) \left(1 - \frac{M_{\tilde{\chi}_1^0}^2}{M_{\tilde{\chi}_2^0}^2}\right) \frac{E_{\tilde{\chi}_2^0} - p_{\tilde{\chi}_2^0}}{M_{\tilde{t}}} \times \frac{1}{2} \left(1 - \sqrt{1 - \left(\frac{m_t}{E_t}\right)^2}\right) \quad (5.33)$$

The configurations for the upper endpoints here are the same as for the massless case described in section 5.2. The lower endpoints are realised with a configuration where all detected particles go into the same direction.

Chapter 6

Searches for the $\tilde{\chi}_2^0$

Since mSUGRA is a Supersymmetry breaking scenario within the minimal supersymmetric extension of the Standard Model favoured by many theorists, it is of high importance to develop analysis methods for this model. Although the measurements at LEP (see section 4.1) and with the WMAP satellite (see section 4.2) give a strong constraint on its parameter space there is still a huge number of open possibilities with very different phenomenologies. Many studies for mSUGRA have been performed in the past years. Most of them concentrate on methods for models with $\tan\beta$ lower than 10. Actually, there is no reason for preferring low $\tan\beta$ -models. It has been pointed out in several recent publications that due to the different phenomenology at different $\tan\beta$ values, studies for high $\tan\beta$ values are very important.

Since there is no evidence for a heavy charged stable particle in the universe and assuming R-parity conservation, the lightest supersymmetric particle in mSUGRA is the stable neutralino $\tilde{\chi}_1^0$. A neutral weakly interacting stable particle escapes the detector, thus, a direct mass reconstruction is not possible. However, it is useful to search for the next-to-lightest neutralino, the $\tilde{\chi}_2^0$, which decays in detectable particles within the detector. It is mainly produced in gluino and squark decays. The focus here is on the leptonic cascade decay channel shown in figure 6.1.

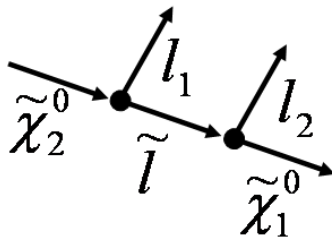


Figure 6.1: Leptonic cascade decay of $\tilde{\chi}_2^0$.

It dominates in areas of the parameter space where $M_{\tilde{\chi}_2^0}$ is larger than $M_{\tilde{l}}$. Results from studies for $\tilde{\chi}_2^0$ -searches in mSUGRA at low $\tan\beta$ [21] are presented very briefly in the following. Then the results of the Monte Carlo analysis at $\tan\beta = 35$ performed in this work are discussed. The latter shows that in principle there are ways to reconstruct the involved sparticle masses in that area of the parameter space.

6.1 Searches at low $\tan\beta$

Leptonic decays of the $\tilde{\chi}_2^0$ have a useful kinematic characteristic. The dilepton invariant mass spectrum has a sharp edge near the kinematic upper limit which is given by formula (5.20).

Thus, constraints on the involved sparticle masses which are independent of the underlying model can be obtained by measuring the endpoint of this distribution. The most straightforward signature for selecting the $\tilde{\chi}_2^0$ decays is provided by the topology with two same-flavour opposite-sign leptons accompanied by large missing transverse energy which comes from the $\tilde{\chi}_1^0$. It is the advantage of low $\tan\beta$ models that many of the charged leptons coming from the $\tilde{\chi}_2^0$ are electrons and muons which can be fully reconstructed. Figure 6.2 shows two representative examples of $\tilde{\chi}_2^0$ branching ratios as a function of $m_{1/2}$ within the WMAP constrained parameter space.

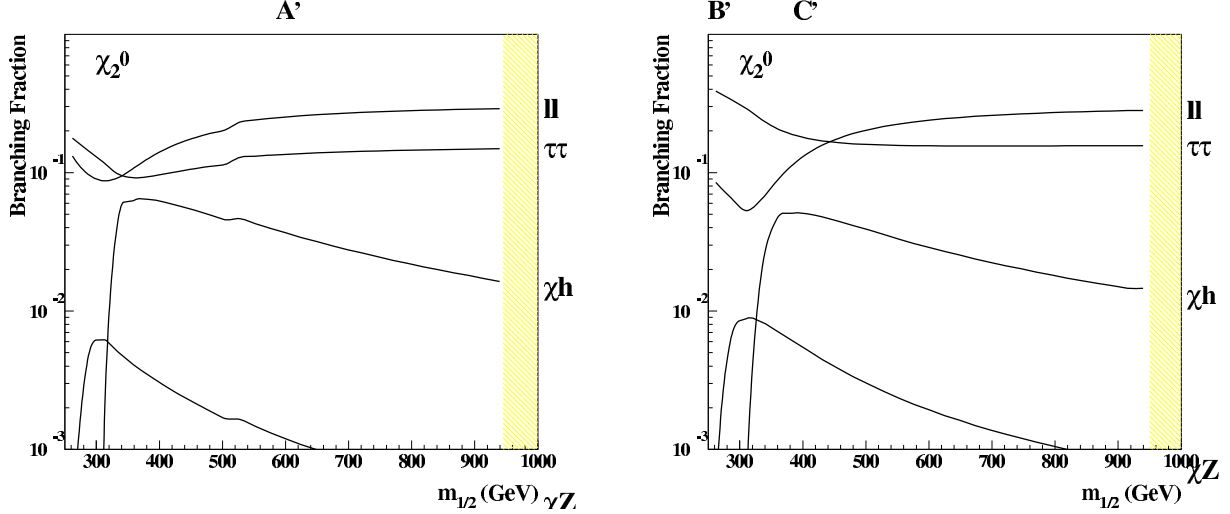


Figure 6.2: Dominant branching ratios along the WMAP line for the $\tilde{\chi}_2^0$ as a function of $m_{1/2}$ at $\tan\beta = 5$ (left) and $\tan\beta = 10$ (right). μ is positive and A_0 is set to zero. The locations of the updated benchmark points A'($m_0 = 107, m_{1/2} = 600$), B'(57,250) and C'(80,400) are indicated [5]. Here leptons ℓ are electrons and muons whereas taus are shown separately.

In the two opposite-sign leptons + E_T^{miss} + (jets) channel the largest Standard Model background is $t\bar{t}$ production, with $t \rightarrow bW$, and both W s decaying into leptons, or one of the leptons coming from a W decay and the other from the b -decay of the same t -quark. Defining the significance σ as $\sigma = (N_{EV} - N_B)/\sqrt{N_{EV}}$ it has been shown that the observability of the kinematic endpoint varies from $\sigma = 77$ at $m_0 = 200$ and $m_{1/2} = 160$ to $\sigma = 27$ at $m_0 = 60$ and $m_{1/2} = 230$ for an integrated luminosity $L_{int} = 10^3 \text{ pb}^{-1}$ [21]. For this luminosity, the appearance of the edges in the distributions is already sufficiently pronounced in a significant part of the m_0 - $m_{1/2}$ -plane. The position of the kinematic edge can be measured with a precision of about 0.5 GeV. Figure 6.3 shows different realisations of such an edge very clearly.

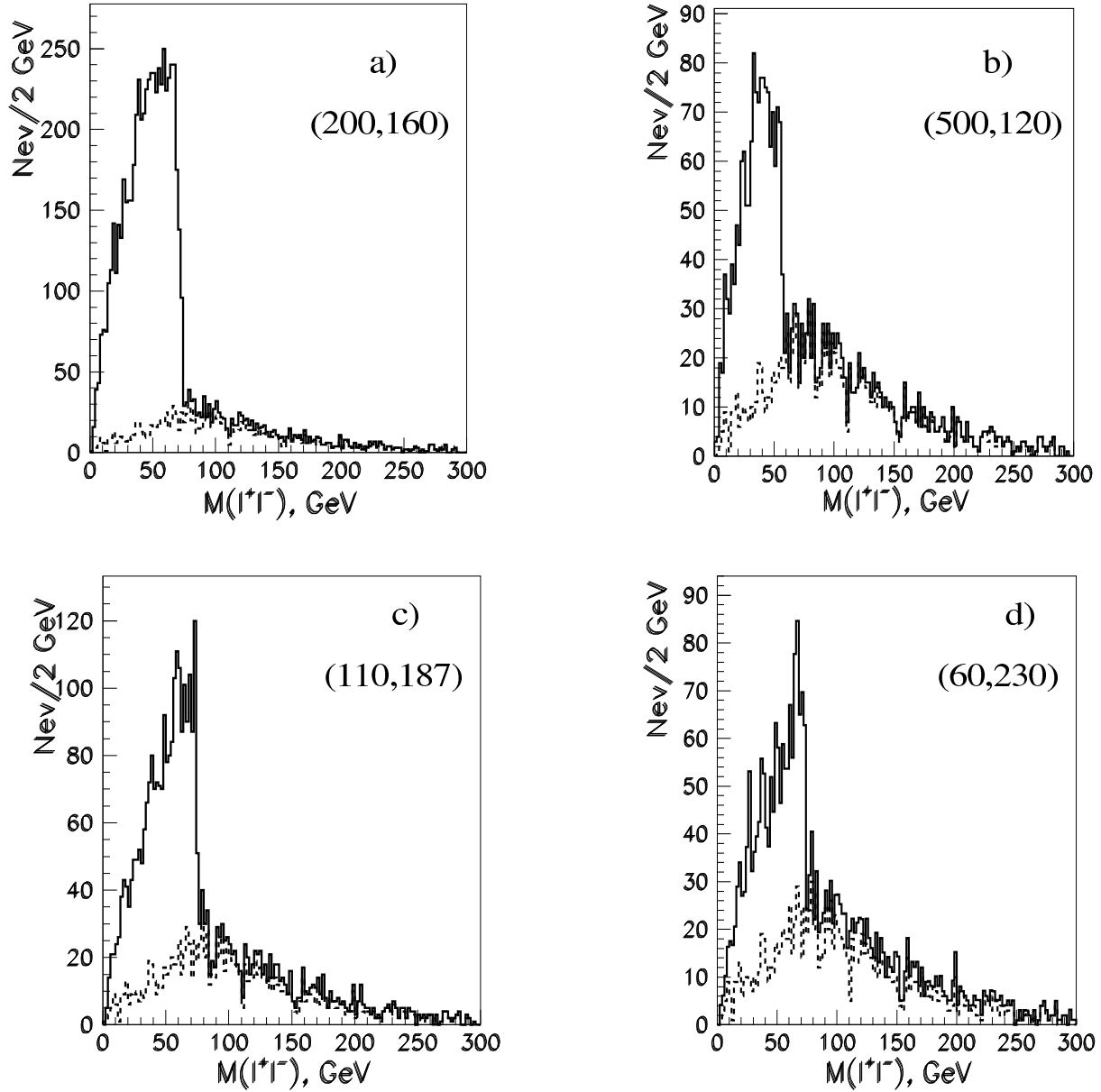


Figure 6.3: The solid line shows the invariant mass distribution of two same-flavour, opposite-sign leptons of $\tilde{\chi}_2^0$ decays at various $(m_0, m_{1/2})$ points for $\tan\beta = 2$ and $\mu < 0$ with $L_{int} = 10^3 \text{ pb}^{-1}$. The Standard Model background is given by the dashed line.

With increasing m_0 and $m_{1/2}$ the cross sections are decreasing and therefore a higher integrated luminosity is needed. In order to perform a full mass reconstruction of the sparticles further analysis methods are necessary which are described to some extent in [21].

6.2 Searches at $\tan\beta = 35$

The kinematic characteristic of the leptonic $\tilde{\chi}_2^0$ decay does not change with increasing $\tan\beta$. However, the branching ratios do. Simulations made with ISASUGRA show that the decay into taus became more and more important with increasing $\tan\beta$. Figure 6.4 illustrates the $\tilde{\chi}_2^0$ branching ratios, evaluated at $\tan\beta = 35$.

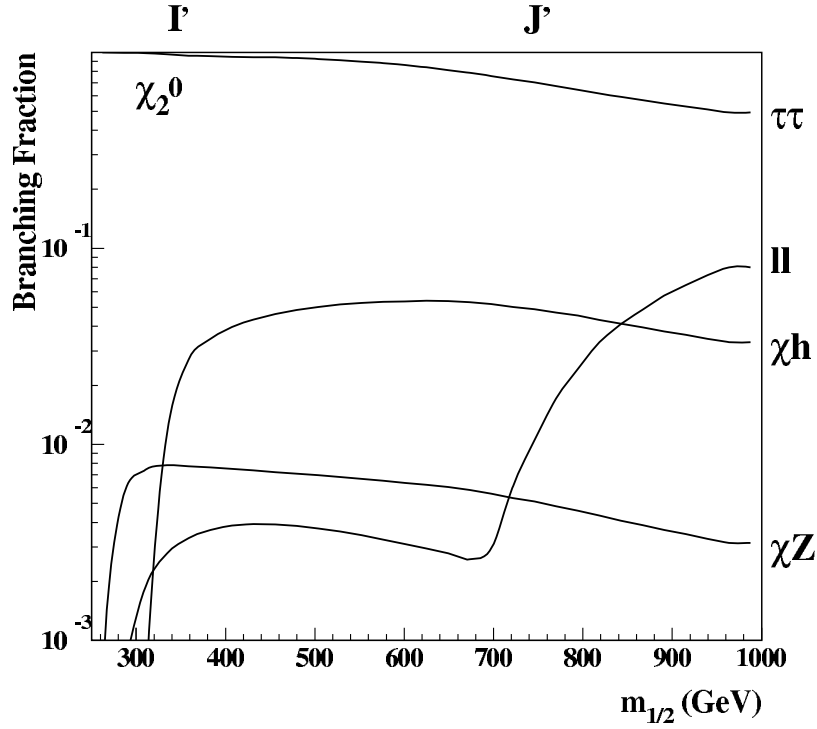


Figure 6.4: Dominant branching ratios along the WMAP line for $\tilde{\chi}_2^0$ as a function of $m_{1/2}$ at $\tan\beta = 35$, $\mu > 0$ and $A_0 = 0$. The location of updated benchmark points $\Gamma(m_0 = 181, m_{1/2} = 350)$ and $J'(299, 750)$ are indicated [5]. Here leptons ℓ are electrons and muons whereas taus are shown separately.

Neither with CMS nor with ATLAS will it be possible to fully reconstruct taus since they decay into at least one ν_τ which escapes the detector. Therefore, the kinematic endpoint in the dilepton invariant mass distribution will in general be smeared out. It is the aim of the following study to investigate the $\tilde{\chi}_2^0$ discovery potential in this region of the mSUGRA parameter space. Furthermore, the goal is to use the $\tilde{\chi}_2^0$ discovery for sparticle mass reconstructions.

6.2.1 Choice of parameters

At the moment it is not known whether the MSSM with mSUGRA describing the Supersymmetry breaking is the right extension of the Standard Model. However, there are experimental (see section 4.1 and 4.2) and theoretical constraints on the mSUGRA parameter space. For the development of analysis methods it is necessary to choose parameters in a characteristic region which is not yet excluded by any experiment and which is accessible for future experiments like the Large Hadron Collider.

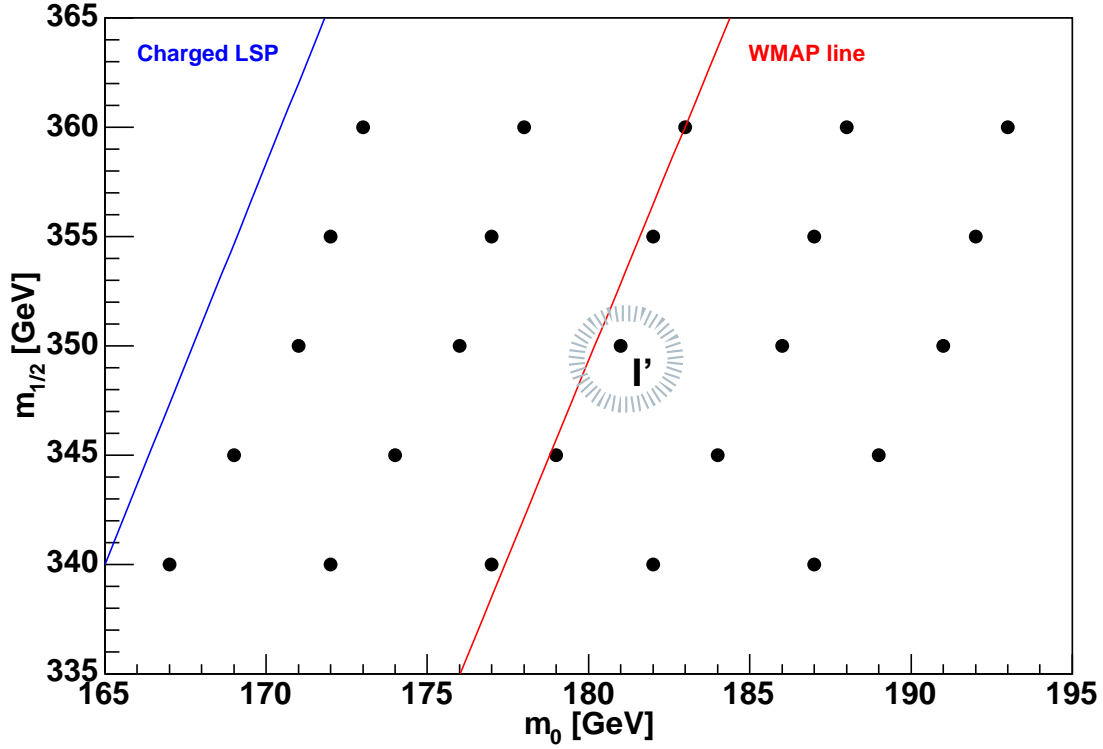


Figure 6.5: Points for the analysis in the m_0 - $m_{1/2}$ plane in an area around the benchmark point I' . The upper left side is excluded due to cosmological constraints.

The parameters in this analysis are chosen with the following motivation:

1. $\tan \beta = 35$: There is no experimental limit which excludes high $\tan \beta$ models. It is still necessary to develop methods for the $\tilde{\chi}_2^0$ discovery at LHC assuming these models. It is especially necessary to determine whether it is possible to discover the $\tilde{\chi}_2^0$ in the τ -channel which is favoured at $\tan \beta = 35$.
2. $m_0 \in [167, 193], m_{1/2} \in [340, 360]$ around I' in figure 6.4: In that region the branching ratio $\text{BR}(\tilde{\chi}_2^0 \rightarrow \tilde{\tau}_1^\pm \tau^\mp)$ is with over 95% especially high. For the analysis 25 points in that region are chosen. In order to consider the WMAP results and the cosmologically excluded region the points are not equidistant which can be seen in figure 6.5.
3. $A_0 = 0$: A non zero value would only be necessary for the electroweak symmetry breaking if the top mass was lower than the measured value. However, it would lead to different particle masses.
4. $\mu > 0$: There is no special reason to choose $\mu > 0$, but the results are not very sensitive to that choice [20].

The masses of the particles relevant for this study in the chosen area of the mSUGRA parameter space are given in table 6.1.

<i>Masses in GeV for $(m_0, m_{1/2})$</i>					
<i>Particle</i>	(167,340)	(187,340)	(181,350)	(173,360)	(193,360)
\tilde{g}	812.06	812.49	834.16	855.61	856.23
\tilde{d}_1/\tilde{s}_1	759.81	764.82	782.61	800.09	804.65
\tilde{d}_2/\tilde{s}_2	730.15	735.04	752.02	768.81	773.64
\tilde{u}_1/\tilde{c}_1	755.24	760.29	778.17	795.75	800.34
\tilde{u}_2/\tilde{c}_2	731.79	736.67	753.80	770.73	775.06
\tilde{b}_1	657.94	661.48	678.14	694.20	697.50
\tilde{b}_2	704.72	708.19	724.93	740.96	744.21
\tilde{t}_1	565.70	568.46	583.27	598.06	600.47
\tilde{t}_2	729.25	731.74	747.90	763.69	766.14
$\tilde{\chi}_2^0$	257.10	257.23	265.52	273.74	273.92
$\tilde{\chi}_1^0$	133.93	133.99	138.11	142.28	142.41
$\tilde{\tau}_1$	135.74	154.52	150.14	144.24	162.56

Table 6.1: Sparticle masses in GeV calculated with ISASUGRA 7.69. A_0 is set to zero, μ is positive and $\tan\beta$ is 35.

6.2.2 Production, decay and selection of $\tilde{\chi}_2^0$

There are different possibilities of producing $\tilde{\chi}_2^0$, and there are different channels in which the $\tilde{\chi}_2^0$ can decay. The four $\tilde{\chi}_2^0$ decays with the highest branching ratios are shown in table 6.2. Table 6.3 shows eight processes with the highest cross sections which either produce a neutralino directly, or indirectly in decays of squarks and gluinos.

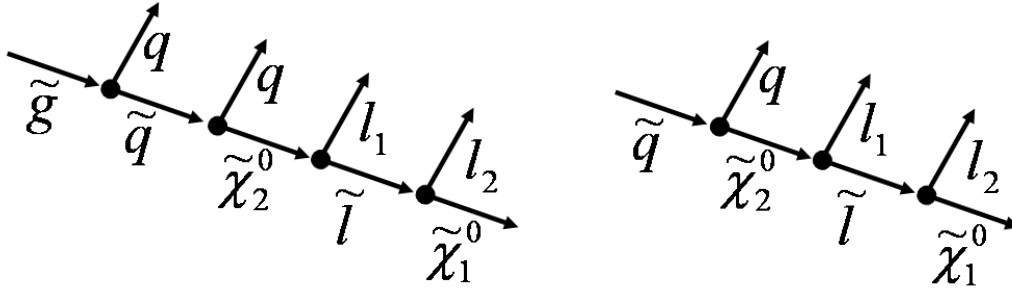


Figure 6.6: Cascade decay of \tilde{g} and \tilde{q} .

The latter processes are used in this study since there are one or two additional quarks in the decay chain which carry information about the involved sparticle masses. They can be combined with both leptons in order to get more kinematic endpoints. The processes are shown in the two diagrams in figure 6.6. Events with directly produced $\tilde{\chi}_2^0$ can only be used for finding the dilepton kinematic endpoint. The cross sections are calculated using PYTHIA 6.220 in combination with ISASUGRA 7.69 at the given $(m_0, m_{1/2})$ values. The reliability of these cross sections is described in appendix A.4. For the indirect production, the squark branching ratios of the decay into the $\tilde{\chi}_2^0$ - shown in table 6.4 - are important. The left handed squarks show much larger branching ratios for the decay into wino-like $\tilde{\chi}_2^0$. The gluinos will in most of the cases first decay into a squark and a quark and then through the squarks produce $\tilde{\chi}_2^0$. Table 6.5 shows

that a significant amount of left squarks is produced through gluino production. Additionally, it can be seen that the sbottom channel is favoured in the gluino decay.

In this study the analysed data samples correspond to 100 000 generated events in which the tau decay is specified. Depending on the values for m_0 and $m_{1/2}$ this leads to between 24278 and 25379 selected events. The event selection in this study is at the Monte Carlo level. In the real experiment it will be an additional challenge to select and reconstruct the taus and the associated quarks. Here an event is defined as follows:

1. Two opposite-sign charged rho mesons (see section 6.2.4) which come from two opposite-sign tau leptons. These tau leptons must come from the cascade decay of the $\tilde{\chi}_2^0$ which is produced through squarks. At this level the exact origin of each particle is known. In order to take the experimental reconstruction of the rho mesons into account, the distribution of the rho mass is included into the simulation. In the real experiment two opposite-sign isolated tau-like jets have to be searched with a π^0 and a π^\pm in the detector having an invariant mass around the ρ^\pm mass.
2. The quarks used in the analysis come only from squarks which decay into a $\tilde{\chi}_2^0$. The flavour is known and also the precise 4-momentum of the quark is used for the analysis. It is mostly called “associated” quark in this study. In the experiment at least one additional jet is needed.
3. No cut on the E_T^{miss} has been applied. However, in the real experiment E_T^{miss} should required to be greater than 100 GeV. This is the value chosen in most of the low $\tan\beta$ studies. It has to be investigated whether this limit is also a good value for high $\tan\beta$.

<i>Branching Ratio in % for $(m_0, m_{1/2})$</i>					
<i>Decay</i>	(167,340)	(187,340)	(181,350)	(173,360)	(193,360)
$\tilde{\chi}_2^0 \rightarrow \tilde{\tau}_1^\pm + \tau^\mp$	96.8	96.2	96.0	96.0	95.2
$\tilde{\chi}_2^0 \rightarrow \tilde{\chi}_1^0 + h^0$	2.1	2.6	2.8	2.9	3.6
$\tilde{\chi}_2^0 \rightarrow \tilde{\chi}_1^0 + Z^0$	0.7	0.9	0.8	0.7	0.9
$\tilde{\chi}_2^0 \rightarrow \tilde{l}_R^\pm + l^\mp$	0.4	0.2	0.3	0.4	0.3

Table 6.2: The largest branching ratios of the $\tilde{\chi}_2^0$ for the chosen mSUGRA parameters. A_0 is set to zero, μ is positive and $\tan\beta$ is 35. The letter l denotes electrons and muons.

Cross Section (pb) for $(m_0, m_{1/2})$						
Subprocess		(167,340)	(187,340)	(181,350)	(173,360)	(193,360)
$g + g \rightarrow \tilde{g} + \tilde{g}$		0.636	0.634	0.526	0.434	0.435
$q_j + g \rightarrow \tilde{q}_{jL} + \tilde{g}$		1.865	1.824	1.578	1.366	1.338
$q_j + g \rightarrow \tilde{q}_{jR} + \tilde{g}$		2.030	1.987	1.718	1.490	1.470
$q + \bar{q} \rightarrow \tilde{\chi}_2^0 + \tilde{\chi}_1^\pm$		0.271	0.276	0.241	0.214	0.217
$q_i + q_j \rightarrow \tilde{q}_{iL} + \tilde{q}_{jL}$		0.502	0.496	0.443	0.399	0.393
$q_i + q_j \rightarrow \tilde{q}_{iR} + \tilde{q}_{jR}$		0.585	0.575	0.515	0.466	0.459
$q_i + q_j \rightarrow (\tilde{q}_{iL} + \tilde{q}_{jR})$		0.467	0.454	0.398	0.365	0.356
$+$	$(\tilde{q}_{iR} + \tilde{q}_{jL})$					
$q_i + \bar{q}_j \rightarrow (\tilde{q}_{iL} + \tilde{\bar{q}}_{jR})$		0.518	0.509	0.444	0.398	0.384
$+$	$(\tilde{q}_{iR} + \tilde{\bar{q}}_{jL})$					

Table 6.3: Most important processes for direct and indirect (in cascade decays of \tilde{g} and \tilde{q}) $\tilde{\chi}_2^0$ production at LHC. A_0 is set to zero, μ is positive and $\tan\beta$ is 35.

Branching Ratio in % for $(m_0, m_{1/2})$					
Decay	(167,340)	(187,340)	(181,350)	(173,360)	(193,360)
$\tilde{d}_L \rightarrow \tilde{\chi}_2^0 + d$	31.1	31.0	31.1	31.2	31.2
$\tilde{d}_R \rightarrow \tilde{\chi}_2^0 + d$	0.3	0.3	0.3	0.2	0.2
$\tilde{u}_L \rightarrow \tilde{\chi}_2^0 + u$	31.5	31.5	31.6	31.6	31.6
$\tilde{u}_R \rightarrow \tilde{\chi}_2^0 + u$	0.3	0.3	0.3	0.2	0.2
$\tilde{s}_L \rightarrow \tilde{\chi}_2^0 + s$	31.1	31.0	31.1	31.2	31.2
$\tilde{s}_R \rightarrow \tilde{\chi}_2^0 + s$	0.3	0.3	0.3	0.2	0.2
$\tilde{c}_L \rightarrow \tilde{\chi}_2^0 + c$	31.5	31.5	31.6	31.6	31.6
$\tilde{c}_R \rightarrow \tilde{\chi}_2^0 + c$	0.3	0.3	0.3	0.2	0.2
$\tilde{b}_1 \rightarrow \tilde{\chi}_2^0 + b$	29.3	29.0	28.5	28.1	27.9
$\tilde{b}_2 \rightarrow \tilde{\chi}_2^0 + b$	7.3	7.0	7.0	7.1	6.9
$\tilde{t}_1 \rightarrow \tilde{\chi}_2^0 + t$	14.3	14.3	14.3	14.4	14.3
$\tilde{t}_2 \rightarrow \tilde{\chi}_2^0 + t$	9.1	9.2	9.3	9.4	9.5

Table 6.4: Squark branching ratios for the decay into $\tilde{\chi}_2^0$. A_0 is set to zero, μ is positive and $\tan\beta$ is 35.

<i>Branching Ratio in % for $(m_0, m_{1/2})$</i>					
<i>Decay</i>	(167,340)	(187,340)	(181,350)	(173,360)	(193,360)
$\tilde{g} \rightarrow \tilde{\chi}_2^0 + t + \bar{t}$	0.01	0.01	0.01	0.01	0.01
$\tilde{g} \rightarrow \tilde{d}_L + d$	3.5	3.2	3.3	3.5	3.2
$\tilde{g} \rightarrow \tilde{d}_R + d$	8.1	7.9	8.0	8.0	7.8
$\tilde{g} \rightarrow \tilde{u}_L + u$	4.1	3.8	3.9	4.0	3.8
$\tilde{g} \rightarrow \tilde{u}_R + u$	7.8	7.6	7.7	7.7	7.5
$\tilde{g} \rightarrow \tilde{s}_L + s$	3.5	3.2	3.3	3.5	3.2
$\tilde{g} \rightarrow \tilde{s}_R + s$	8.1	7.9	8.0	8.0	7.8
$\tilde{g} \rightarrow \tilde{c}_L + c$	4.1	3.8	3.9	4.0	3.8
$\tilde{g} \rightarrow \tilde{c}_R + c$	7.8	7.6	7.7	7.7	7.5
$\tilde{g} \rightarrow \tilde{b}_1 + b$	24.8	25.8	24.8	24.0	24.8
$\tilde{g} \rightarrow \tilde{b}_2 + b$	13.9	14.2	14.0	13.8	14.1
$\tilde{g} \rightarrow \tilde{t}_1 + t$	14.3	15.0	15.5	15.8	16.5
$\tilde{g} \rightarrow \tilde{t}_2 + t$	0.0	0.0	0.0	0.0	0.0

Table 6.5: Gluino branching ratios for the given $(m_0, m_{1/2})$ values. A_0 is set to zero, μ is positive and $\tan \beta$ is 35. For the chosen parameters the \tilde{g} cannot decay into $\tilde{t}_2 + t$ because $M_{\tilde{g}} < M_{\tilde{t}_2} + M_t$.

6.2.3 Methods to find the endpoint

Due to the presence of neutrinos in the investigated $\tilde{\chi}_2^0$ decay, the distribution of the invariant mass of all visible $\tilde{\chi}_2^0$ decay products is fundamentally different from the case where the $\tilde{\chi}_2^0$ decays into a $\tilde{\chi}_1^0$ and a pair of electrons or muons. The neutrinos smear out the kinematic endpoint, which is shown in figure 6.7. Therefore, it is necessary to define a method how to find the kinematic endpoints in the measured invariant mass (M_{INV}) distributions. In the following two “simple” types are presented. “Simple” means here that they do in principle not depend on the model. However, the included corrections for the improvement of the measurement and the obtained systematic uncertainties are based on mSUGRA Monte Carlo simulations.

Linear fit

First, there is the possibility to perform a linear fit $f(M_{INV})$ to the invariant mass distribution near the kinematic limit. The invariant mass range in which the fit is performed needs to be chosen carefully in order to obtain a sensible fit. Certainly, the region is between the bin with the highest content and the end of the tail. Good results have been achieved using an area starting at the bin with 50% and ending at the bin with 5% of the maximum bin content. Definitely, this definition is only meaningful if no background is included. The measured endpoint Ep_i^M for each point i of the $N = 25$ investigated points in the parameter space is then defined as the intercept point of the fit line and the abscissa. A_i is a free parameter which is not needed for the endpoint measurement.

$$f(M_{INV}) = A_i \cdot (M_{INV} - B_i) \quad (6.1)$$

$$Ep_i^M = B_i \quad (6.2)$$

The mean statistical uncertainty on Ep^M is

$$\delta_{stat} Ep^M = \frac{\sum_{i=1}^N \delta B_i}{N} \quad (6.3)$$

with δB_i being the statistical uncertainty of B_i . The systematic shift S of the endpoint measurement is given by the mean difference of the theoretical endpoint Ep_i^T and Ep_i^M , which includes a systematic and a statistical uncertainty.

$$S = \frac{\sum_{i=1}^N Ep_i^T - Ep_i^M}{N} \quad (6.4)$$

$$\delta S = \sqrt{\frac{\sum_{i=1}^N (Ep_i^T - Ep_i^M - S)^2}{N}} \quad (6.5)$$

The corrected measured endpoint is then

$$Ep_i^{M,c} = Ep_i^M + S. \quad (6.6)$$

The pure systematic uncertainty on the endpoint measurement is then

$$\delta_{syst} Ep_i^M = \sqrt{(\delta S)^2 - (\delta_{stat} Ep_i^M)^2} \quad (6.7)$$

Certainly, the calculated S can and will change when a different region in the mSUGRA parameter space is chosen.

Gaussian fit

Second, the shape of the distribution can be investigated. In the chosen region the neutrinos smear out the visible invariant mass distribution near the kinematic limit. As a result the maximum of the invariant mass distribution is at a mass much lower than the endpoint. The measurable maximum G_i is here defined as the maximum of an iterated gaussian fit. The maximum position is determined as follows:

1. The bin with the maximal bin content is the centre for the first gaussian fit. Unless otherwise noted for the investigated invariant mass distributions a sensible area for the gaussian fit is a symmetric area around the centre of 25% of the centre value.
2. The resulting gaussian maximum is then the input for the centre of the second fit.
3. It turned out that three iterations are enough for a stable maximum. The last (out of three) gaussian maximum is taken for G_i .

G_i has a statistical uncertainty δG_i . If there is a correlation between the maximum and the endpoint which is independent of m_0 and $m_{1/2}$ over a large area, then it is possible to get the endpoint value out of the maximum measurement. In the following it is assumed that there exists a linear dependence between G_i and Ep_i^T . A linear least squares fit of Ep_i^T as a function of $G_i \pm \delta G_i$ with the fit function $f(G) = C \cdot G + D$ gives the values for this dependence. The measured endpoint Ep_i^M with its mean statistical uncertainty $\delta_{stat} Ep_i^M$ is then

$$Ep_i^T = C \cdot G_i + D, \quad (6.8)$$

$$\delta_{stat} Ep_i^M = C \cdot \frac{\sum_{i=1}^N \delta G_i}{N}. \quad (6.9)$$

The corrected endpoint, the systematic shift with its uncertainty and the pure systematic uncertainty are equally defined as in the case of the linear fit. Since the gaussian maximum should be zero if Ep_i^T is zero it is interesting to check whether D is close to zero or not. This value gives a hint for the stability of the assumed correlation on further changes in m_0 and $m_{1/2}$. In the following analysis therefore also the slope C and the resulting uncertainties on the endpoint measurement are given if D is forced to zero. It is obvious that the gaussian method relies on

Monte Carlo simulations in order to find C and D whereas the measurements of a sharp edge at low $\tan \beta$ are model independent.

The difference between Ep_i^T and $Ep_i^M + S$ in the linear and in the gaussian case may have in some cases a m_0 and $m_{1/2}$ dependence. This is discussed for each invariant mass distribution separately. For the analysis the binning and the choice of the fit area have been optimised such that they are most universally valid within the investigated area of the mSUGRA parameter space.

6.2.4 Selection of the leptonic decay

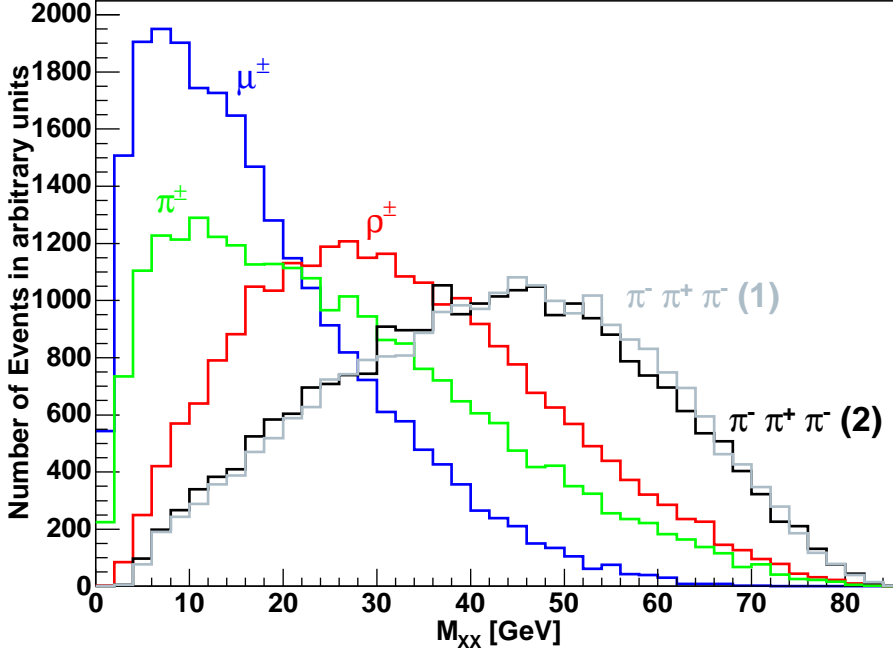


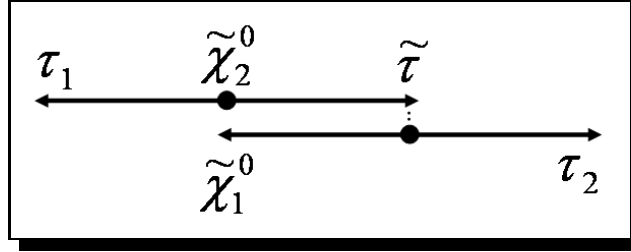
Figure 6.7: The red line shows the visible dilepton invariant mass distribution in the ρ^\pm -channel, the green line in the π^\pm -channel and the blue line in the μ^\pm -channel for $m_0 = 181$ and $m_{1/2} = 350$. The gray (1) and the black (2) line show the distribution of the 3-prong channel. The first includes the $\tau^\pm \rightarrow \pi^\pm \rho^0 \nu_\tau$ and the direct $\tau^\pm \rightarrow \pi^\pm \pi^\mp \pi^\pm \nu_\tau$ decay whereas in the second only the latter is included.

Unlike electrons and muons, the tau leptons cannot be fully reconstructed, since they decay in at least one neutrino within the detector. However, it is the aim to find the invariant mass upper limit of both tau leptons in the leptonic $\tilde{\chi}_2^0$ decay. The kinematic endpoint of the visible dilepton invariant mass distribution is the same as the limit of the true invariant mass because neutrinos are massless. However, its shape is strongly dependent on the chosen visible particles. The branching ratios for the tau decays in detectable particles are shown in table 6.6. For the $\tau^\pm \rightarrow \rho^\pm \nu_\tau$ channel, the visible mass of the $\tilde{\chi}_2^0$ decay products tends to be higher than for the other channels, except the 3-prong, which can be seen in figure 6.7. There the neutrinos get less energy than in the other decay chains because of the relatively large rho mass. The branching ratio of 25.41%, compared to the 14.57% of the 3-prong channel, is a further advantage of this channel. Therefore, in the following analysis the $\tau^\pm \rightarrow \rho^\pm \nu_\tau$ channel is chosen. The ρ^\pm used here are at Monte Carlo level with a mean mass of 766 MeV and a width of about 126 MeV given by PYTHIA.

$\tau^\pm \rightarrow \rho^\pm \nu_\tau$	(25.41%)
$\tau^\pm \rightarrow \mu^\pm \nu_\mu \nu_\tau$	(17.36%)
$\tau^\pm \rightarrow e^\pm \nu_e \nu_\tau$	(17.84%)
$\tau^\pm \rightarrow h^- h^- h^+ \geq 0 \text{ neutrals } \nu_\tau$	(14.57%)
(3-prong, ex. $K_S^0 \rightarrow \pi^+ \pi^-$)	
$\tau^\pm \rightarrow \pi^\pm \nu_\tau$	(11.06%)
Other	(13.76%)

Table 6.6: The branching ratios of the tau lepton [12].

6.2.5 The kinematic limit of $M_{\rho^\pm \rho^\mp}$



The mass of the $\tilde{\tau}^\pm$ is quite similar to that of the $\tilde{\chi}_1^0$ for small values of m_0 in the chosen mSUGRA parameter space. Formula (5.20) shows that in this case the endpoint is close to zero. Therefore, the theoretical values for the dilepton kinematic limit given in figure 6.8 have a strong m_0 and $m_{1/2}$ dependence. In the decay chain of the $\tilde{\chi}_2^0$ at high $\tan \beta$ there will in about 6% of the cases be two opposite-sign rho mesons which can be used for the endpoint measurement. The shape of the invariant mass spectrum of both rho mesons shows that there is no sharp edge near the kinematic limit since it is smeared out due to the neutrinos. However, there are two possibilities to measure the endpoints (see section 6.2.3). In the following analysis the whole data samples with about 25000 events are used to determine the corrections and systematic uncertainties for both methods.

First, it is possible to perform a linear fit to the tail of the distribution. An example is given in figure 6.9. The measured endpoint mass is too small for every point in the investigated region. The mean statistical uncertainty $\delta_{stat} Ep^M$ on this measurement for these large data samples is 0.2 GeV and therefore negligible. The mean correction S is 9.0 GeV which can be seen in figure 6.10. Indeed, the uncertainty $\delta S = 1.8$ GeV on this correction is small, but as can be seen in figure 6.11 the real needed correction should increase with increasing m_0 . The pure mean systematic uncertainty $\delta_{sys} Ep^M$ is 1.7 GeV.

The second method can be applied for this distribution since the gaussian fit is stable for all 25 points and the assumed linear dependence between G_i and Ep_i^T is sensible (see figure 6.12). If the linear fit of Ep_i^T as a function of $G_i \pm \delta G_i$ is forced to go through the origin, the resulting slope C is 3.1. The statistical uncertainty $\delta_{stat} Ep^M$ on the endpoint measurement has then a mean value of 2.2 GeV. However, in this case a systematic shift S of 1.5 ± 2.3 GeV is needed in the whole region to improve the endpoint measurement (see figure 6.13). If the fit is not forced to intersect the origin the value C changes to 3.4, no systematic shift S is needed and δS decreases to 1.9 GeV. The fit here intersects the ordinate at $D = -6.1$ GeV. The mean statistical uncertainty $\delta_{stat} Ep^M$ on the endpoint measurement increases slightly to 2.4 GeV. The mean pure systematic uncertainty is not defined here because δS is dominated by the

statistical uncertainty in the data samples. The difference of the theoretical endpoint Ep_i^T and Ep_i^M shown in figure 6.14 has no significant m_0 and $m_{1/2}$ dependence.

<i>Value</i>	Linear	Gaussian FO	Gaussian NFO
$\delta_{stat}Ep^M$	0.2	2.2	2.4
S	9.1	1.5	0
δS	1.8	2.3	1.9

Table 6.7: A summary of the calculated mean uncertainties and systematic shifts in GeV. $\delta_{stat}Ep^M$ is the statistical uncertainty on the endpoint measurement, S is the mean difference of the measured and the theoretical endpoint with the root-mean-square deviation δS defined in formula 6.4 and 6.5. FO denotes the results with fixed origin and NFO with non-fixed origin in the $G_i-Ep_i^T$ plane.

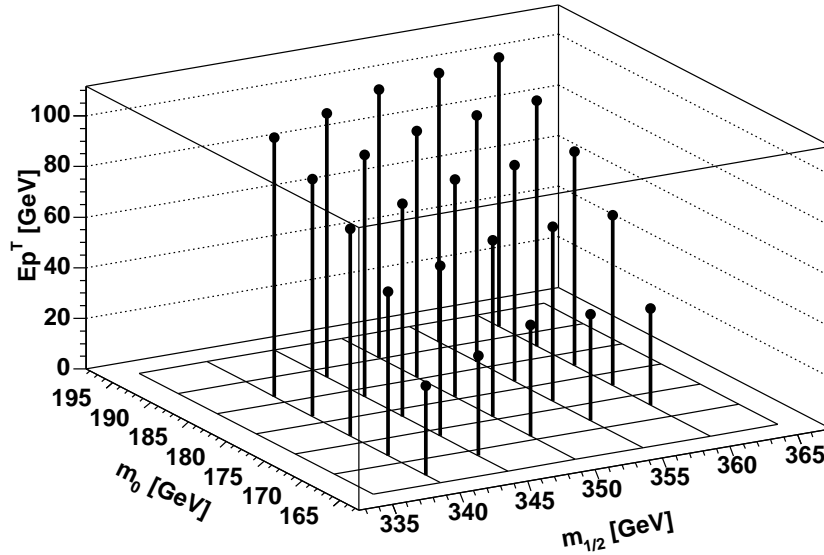


Figure 6.8: Theoretical kinematic endpoints in GeV for the invariant mass of both opposite-sign rhos coming from the $\tilde{\chi}_2^0$ and the $\tilde{\tau}$ respectively. The endpoint masses decrease significantly for decreasing values of m_0 .

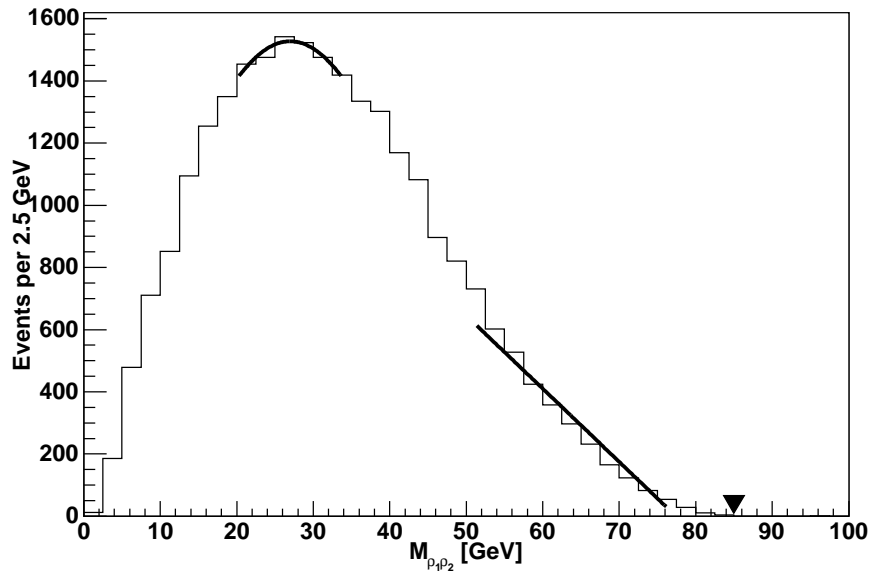


Figure 6.9: Example for the linear and the gaussian fit at $m_0 = 181$ and $m_{1/2} = 350$. In this distribution 25071 events are represented. The triangle shows the theoretical kinematic endpoint at 85.8 GeV.

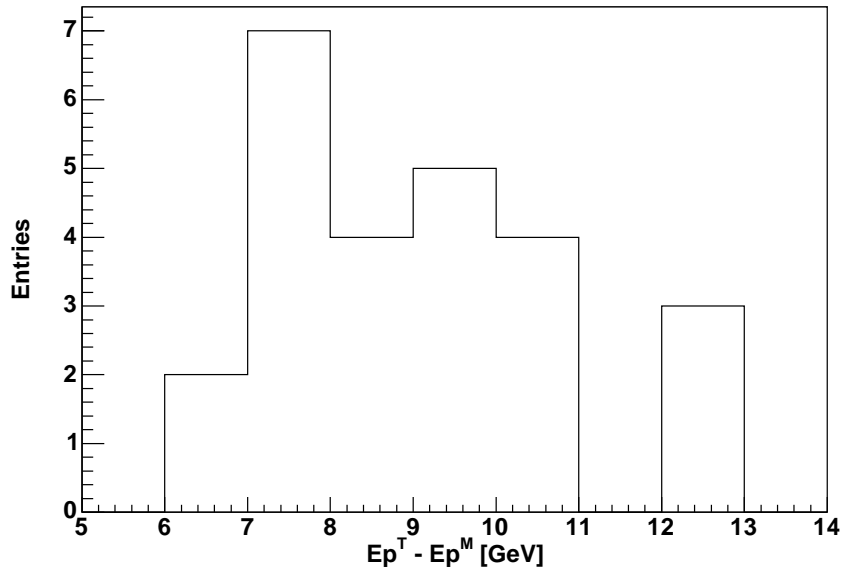


Figure 6.10: The difference of the theoretical and the measured $M_{\rho^\pm\rho^\mp}$ endpoint in GeV obtained with the linear fit at the 25 investigated points in the m_0 - $m_{1/2}$ plane. It shows a mean value of 9.1 GeV with a root-mean-square deviation of 1.8 GeV.

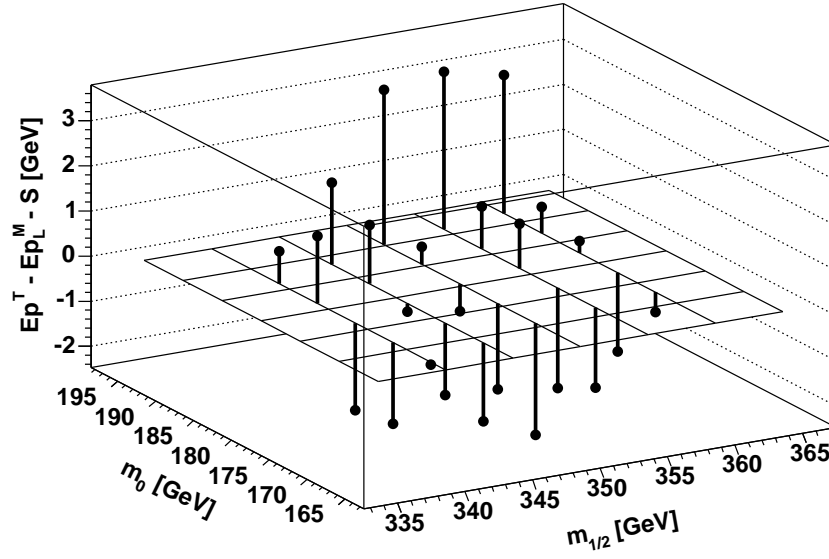


Figure 6.11: The theoretical $M_{\rho^\pm \rho^\mp}$ endpoint minus the measured endpoint in GeV obtained with the linear fit after applying the constant correction of 9.1 GeV. The values decrease significantly for decreasing values of m_0 .

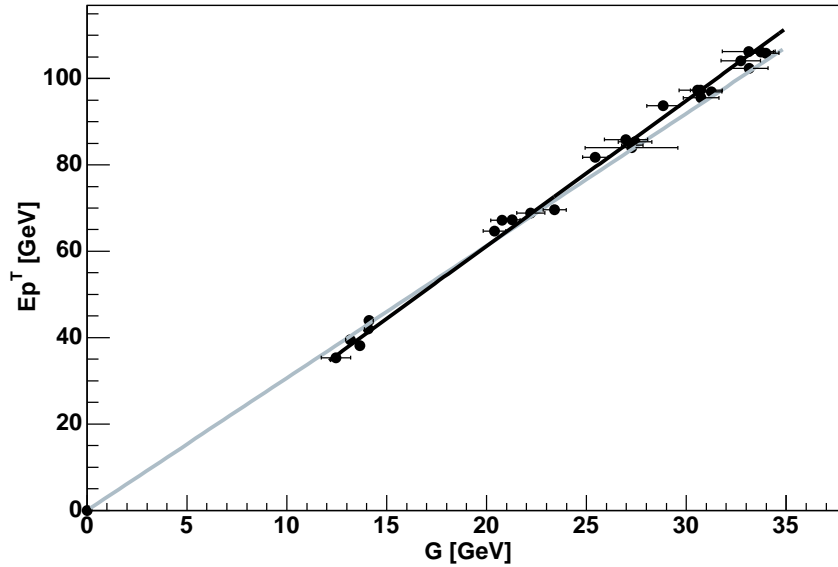


Figure 6.12: The theoretical dilepton kinematic endpoints as a function of the measured gaussian maximum for all 25 investigated points in the m_0 - $m_{1/2}$ plane. The gray line is forced to go through the origin whereas the black has an optimised ordinate value.

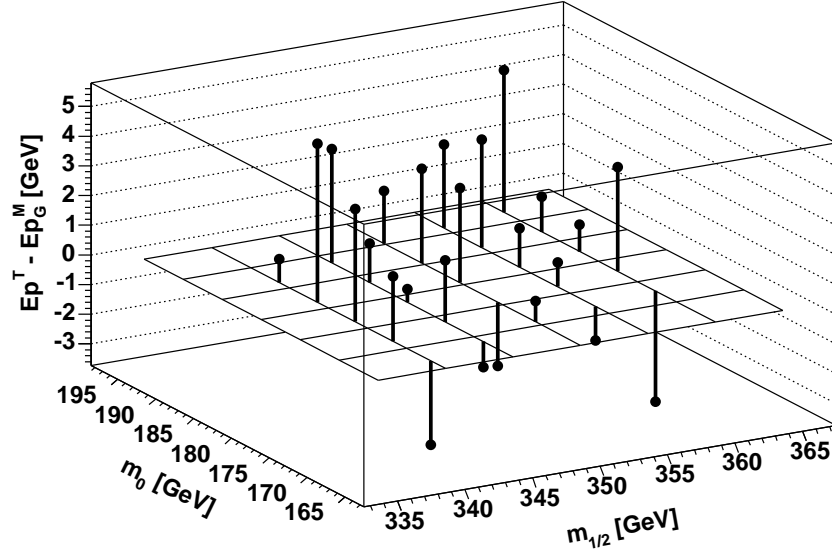


Figure 6.13: The difference of the theoretical and the measured $M_{\rho^\pm \rho^\mp}$ endpoint in GeV obtained with the gaussian fixed origin method. The measured values are on average lower by 1.5 GeV.

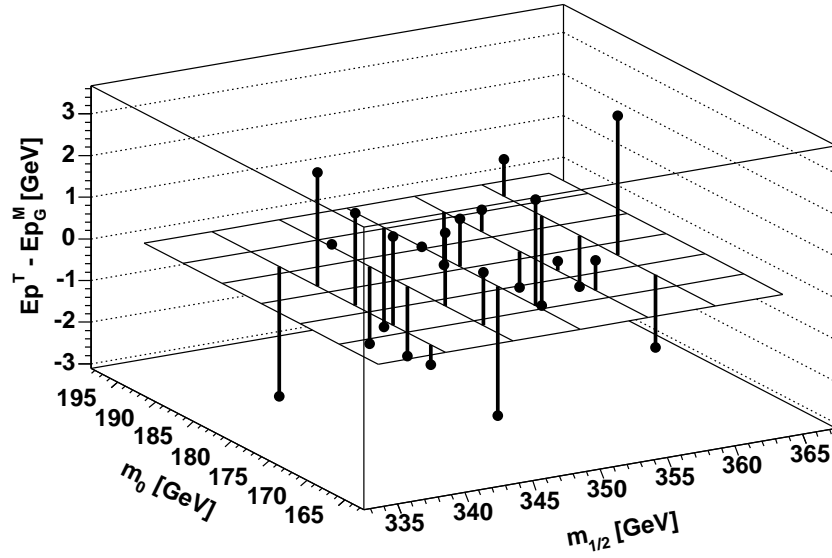
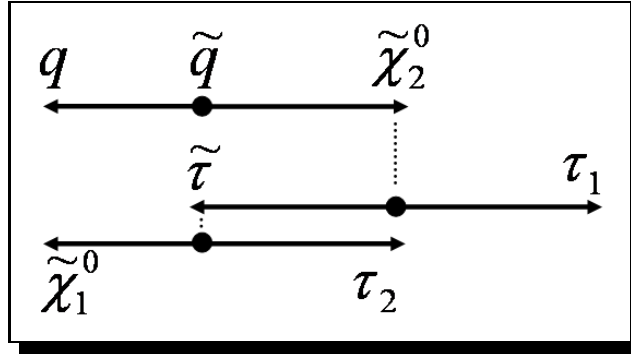


Figure 6.14: The difference of the theoretical and the measured $M_{\rho^\pm \rho^\mp}$ endpoint in GeV obtained with the gaussian non-fixed origin method.

6.2.6 Selection of quarks

In order to get more equations for the reconstruction of the sparticle masses it is necessary to include the quark which comes from the process $\tilde{q}_i \rightarrow \tilde{\chi}_2^0 + q_i$. Since the squark masses are flavour dependent the kinematic limits are as well. In the detector it may in principle be possible to distinguish up, down, charmed and strange quarks from bottom and top quarks. The top quark decays mainly into a bottom quark and a W boson. Therefore, by using the b-tagging it is in principle possible to divide the processes into two groups, light and heavy quarks. The upper kinematic limits of the invariant mass distributions with quarks depend on the most heavy squark. In the investigated region the heaviest squarks among the \tilde{u} , \tilde{d} , \tilde{c} and \tilde{s} are the left handed \tilde{d}_1 and \tilde{s}_1 . Therefore only this mass can be reconstructed. The kinematic limits for events with \tilde{d}_2 , \tilde{s}_2 , $\tilde{u}_{1,2}$ and $\tilde{c}_{1,2}$ are hidden within the measured distributions. However, due to the proton structure the \tilde{u}_1 dominates the distributions as can be seen in figure 6.15. The heavy quark distributions are strongly dominated by the \tilde{b}_1 (\tilde{t}_1), however, \tilde{b}_2 (\tilde{t}_2) are heavier and determine the value for the upper kinematic limit. This problem is discussed in more detail in section 6.2.10. In this study bottom and top quarks are treated separately in order to understand their different contributions to the invariant mass distributions. This knowledge can then be used for more realistic simulations. The following results, which include information from quarks, are strongly dependent on the precision of the quark energy reconstruction. For the analysis quarks are used at the parton level. Indeed, this is a very crude approach but, nevertheless, the methods developed here may also be valid for the real experiment.

6.2.7 The kinematic limit of $M_{\rho^\pm \rho^\mp q}$ for light quarks



The invariant mass distribution of the quark which comes from the decay $\tilde{q} \rightarrow q + \tilde{\chi}_2^0$ and the same two rho mesons used in section 6.2.5 carries further information which can be used for the reconstruction of sparticle masses. Figure 6.16 shows that the theoretical values of the kinematic limits have a very small m_0 dependence and a slightly stronger $m_{1/2}$ dependence in that area compared to the dilepton case. The reason is that the last factor in formula (5.23) in that region is never close to zero in contrast to that in formula (5.20). The m_0 dependence is only caused by the change in the squark mass whereas the $m_{1/2}$ dependence takes also the changes of both neutralino masses into account. For the following analysis data samples of about 18000 events have been used. They include the same events as used in the previous section with the constraint that the associated quarks have the flavour up, down, charmed or strange. An estimation of the kinematic limit can be achieved with a linear fit. An example is given in figure 6.17. The measured value is too low for every point in the parameter space. As can be seen in figure 6.18 and figure 6.19 the actually needed correction is not constant within the investigated area. The gaussian method cannot be applied to this case, since there is no linear dependence between the maximum and the endpoint - which can be seen in figure 6.20.

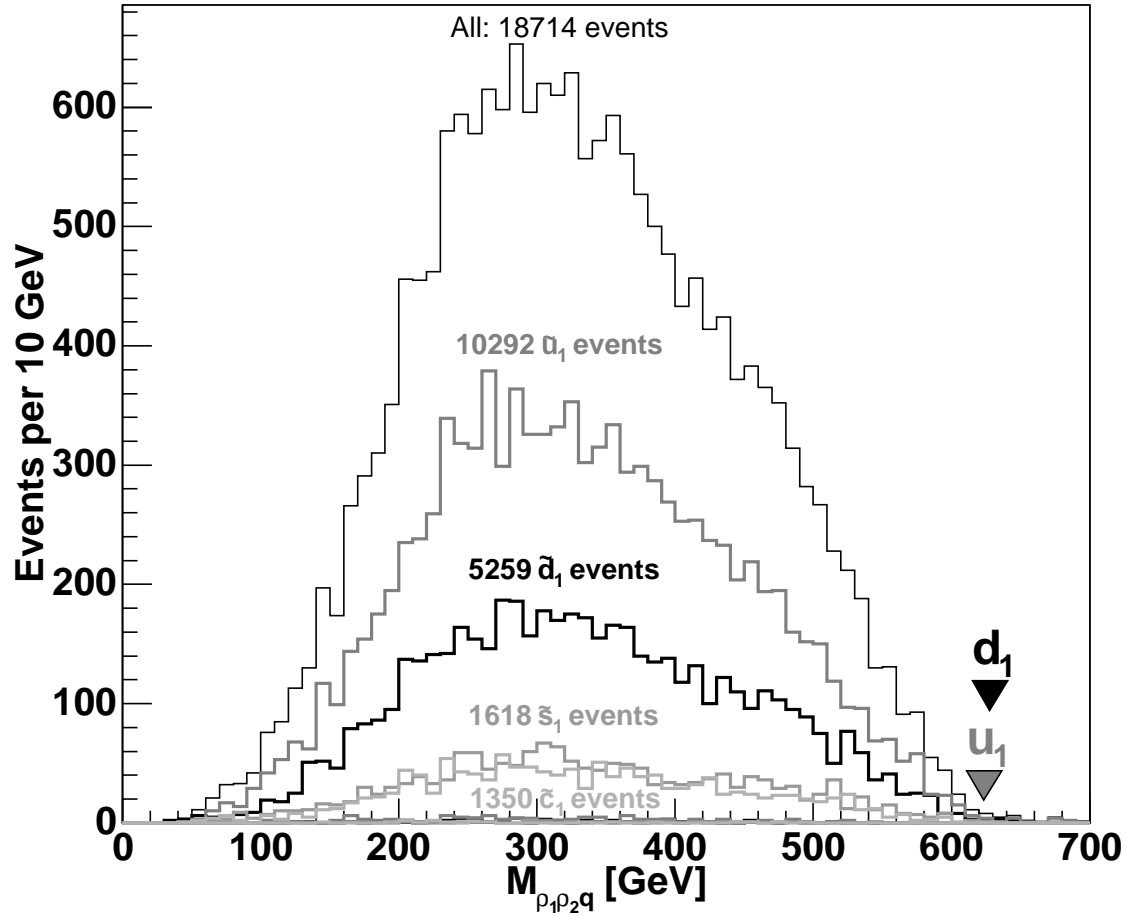


Figure 6.15: The invariant mass distributions for two opposite-sign rhos with the associated light quark q ($\tilde{q} \rightarrow q + \tilde{\chi}_2^0$). The gray triangle shows the theoretical endpoint for the \tilde{u}_1 and \tilde{c}_1 distribution at 624 GeV and the black triangle that for the \tilde{d}_1 and \tilde{s}_1 distribution at 628 GeV. The \tilde{u}_1 distribution clearly dominates, but due to the small difference of both theoretical endpoints the effect is small, too.

Value	Linear
$\delta_{stat} E p^M$	1.7
S	14.0
δS	7.8

Table 6.8: A summary of the calculated correction and the mean uncertainties in GeV for the endpoint measurement in the distribution of $M_{\rho^\pm \rho^\mp q}$.

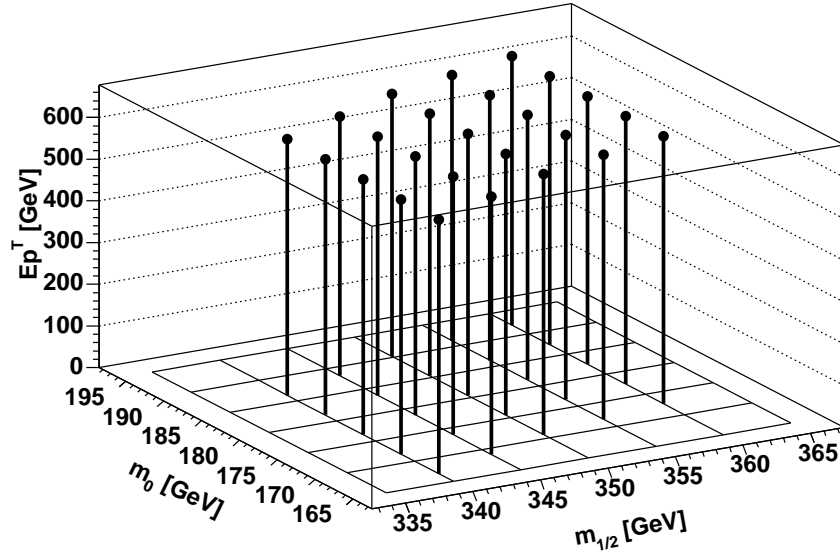


Figure 6.16: Theoretical kinematic endpoints in GeV for the invariant mass of both opposite-sign rhos, coming from the $\tilde{\chi}_2^0$ and the $\tilde{\tau}$ respectively, and the associated quark from $\tilde{s}_1, \tilde{d}_1 \rightarrow s, d + \tilde{\chi}_2^0$ in the investigated area.

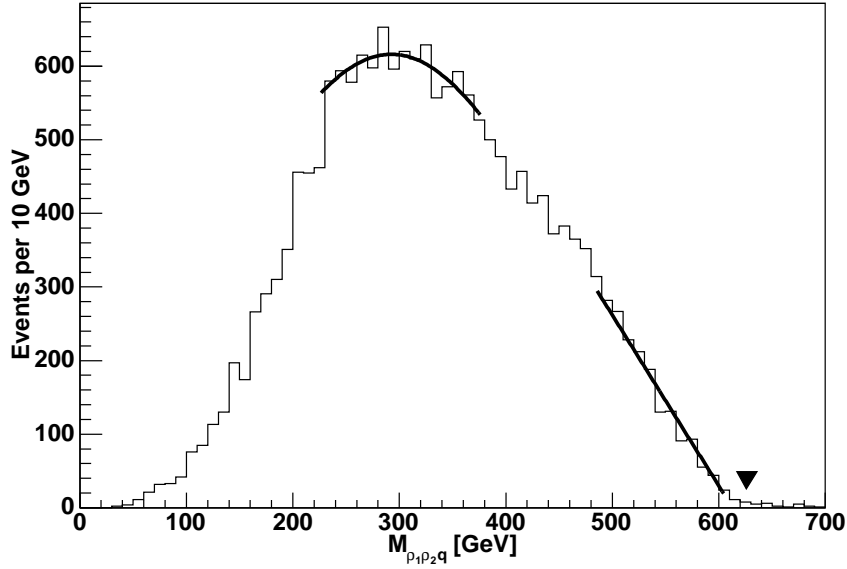


Figure 6.17: Example for the linear and the gaussian fit at $m_0 = 181$ and $m_{1/2} = 350$. The invariant mass distribution is based on 18714 light quark events which are defined in section 6.2.2. The triangle shows the theoretical kinematic endpoint of $M_{\rho^\pm \rho^\mp q}$ at 627.8 GeV.

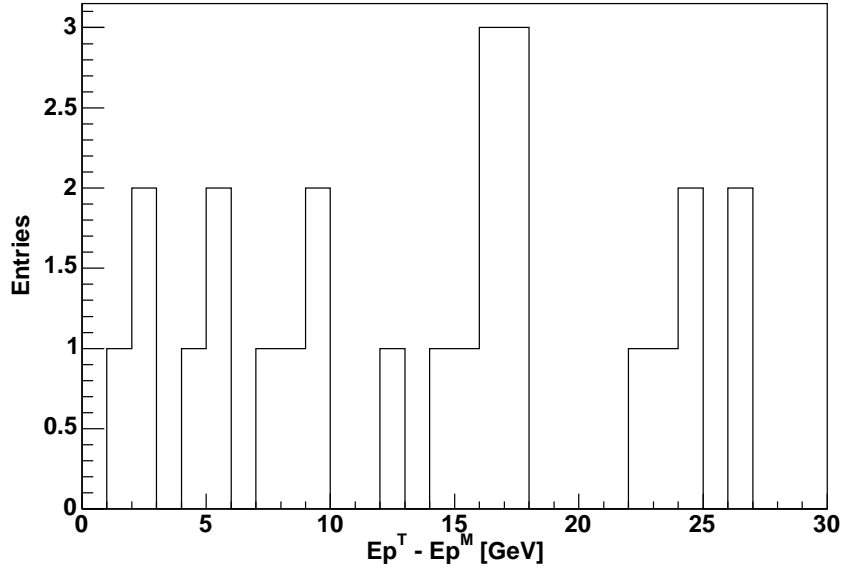


Figure 6.18: The theoretical $M_{\rho^\pm \rho^\mp q}$ endpoint minus the measured endpoint in GeV for all 25 points. The mean value is 14.0 GeV with a root-mean-square deviation of 7.8 GeV.

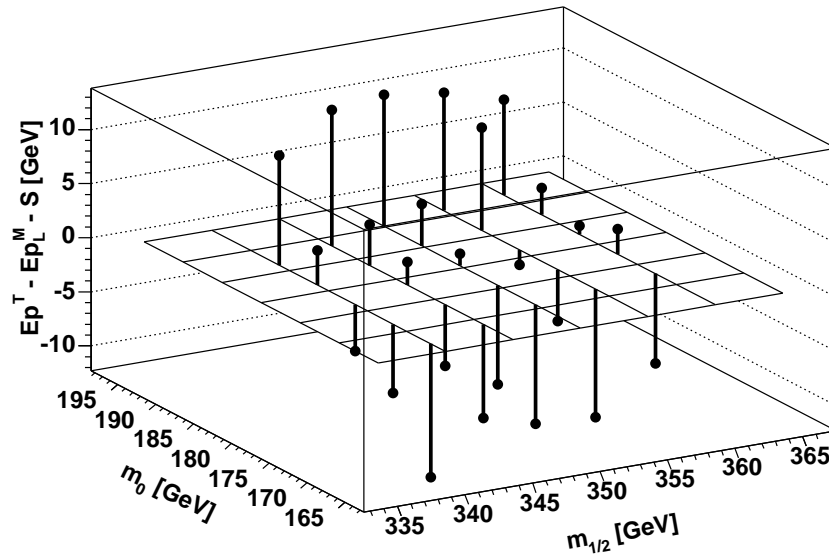


Figure 6.19: The theoretical endpoint minus the measured endpoint in GeV after applying a constant correction of 14.0 GeV.

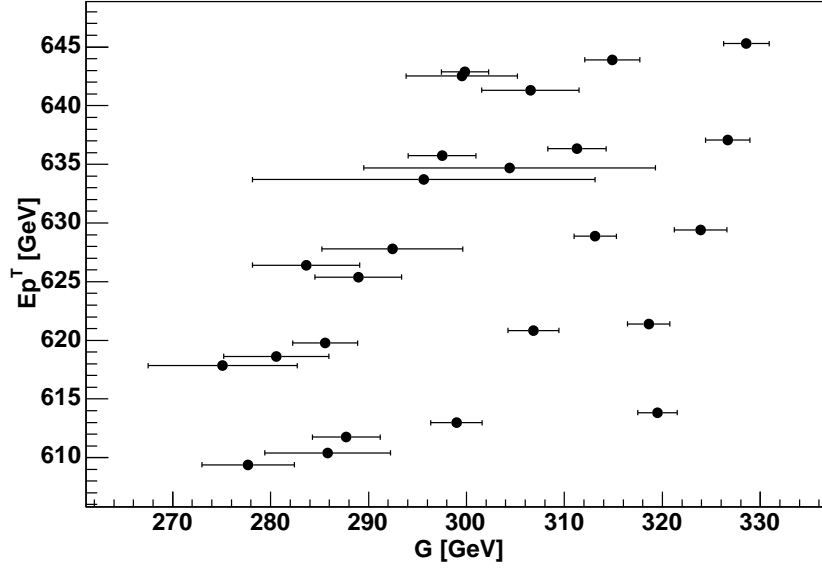
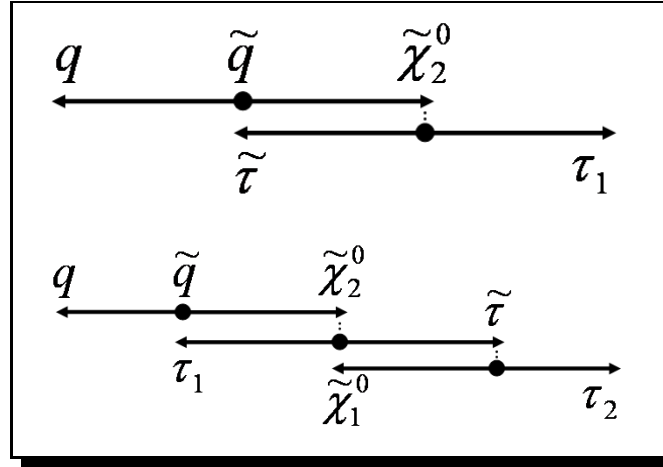


Figure 6.20: The theoretical kinematic dilepton endpoints as a function of the measured gaussian maximum for all 25 investigated points in the m_0 - $m_{1/2}$ plane. A unique mapping of the measured maximum to the theoretical endpoint can not be established since several theoretical endpoint values are associated with the same measured maximum. Additionally, some distributions are flat around the maximum which leads to large uncertainties.

6.2.8 Two kinematic limits in $M_{\rho^{\pm}q}$ for light quarks



As described in section 5.1 there are two different leptons in the investigated decay chain. The first comes directly from the $\tilde{\chi}_2^0$ and the second from the slepton. Both leptons have different kinematic properties so that the endpoint of the invariant mass of first lepton with the light quark is not the same as that with the second lepton. However, in the experiment it will not be possible to know for each event which is the first lepton and which the second. In the following it is described how, nevertheless, both endpoints can be separated if the values are not too close to each other. For the latter constraint it is necessary to compare formula (5.21) with formula (5.22). In the chosen area of m_0 and $m_{1/2}$ the $\tilde{\tau}$ mass is much closer to the $\tilde{\chi}_1^0$ mass

than to the $\tilde{\chi}_2^0$ mass. Thus, the second endpoint is much lower than the first one and it will be possible to distinguish both endpoints. First, the method for finding the second endpoint will be described as its outcome is useful for measuring the first endpoint.

For the measurements of the smaller second endpoint (given in figure 6.22) the first rho gives a background which has to be avoided. In figure 6.21 the invariant mass distribution of the single rho with one quark versus the invariant mass of both opposite-sign rhos is shown. On the left upper quadrant the events with the second rho dominate. Therefore, by ignoring the events with an invariant mass of both rho mesons being less than or equal to 55% of its upper limit the background can be well reduced. This cut value has been uniformly optimised for all 25 points. The ratio of the signal to the first lepton background between zero and the theoretical value for the second kinematic endpoint can thus be increased by a factor which is between 1.4 and 1.9, depending on the values for m_0 and $m_{1/2}$. This improvement can be seen by comparing figure 6.23 with figure 6.24. For each individual point in the parameter space the signal to background ratio could even be improved by changing the cut value. For the following analysis data samples of between 5096 and 6806 events after the cut have been used.

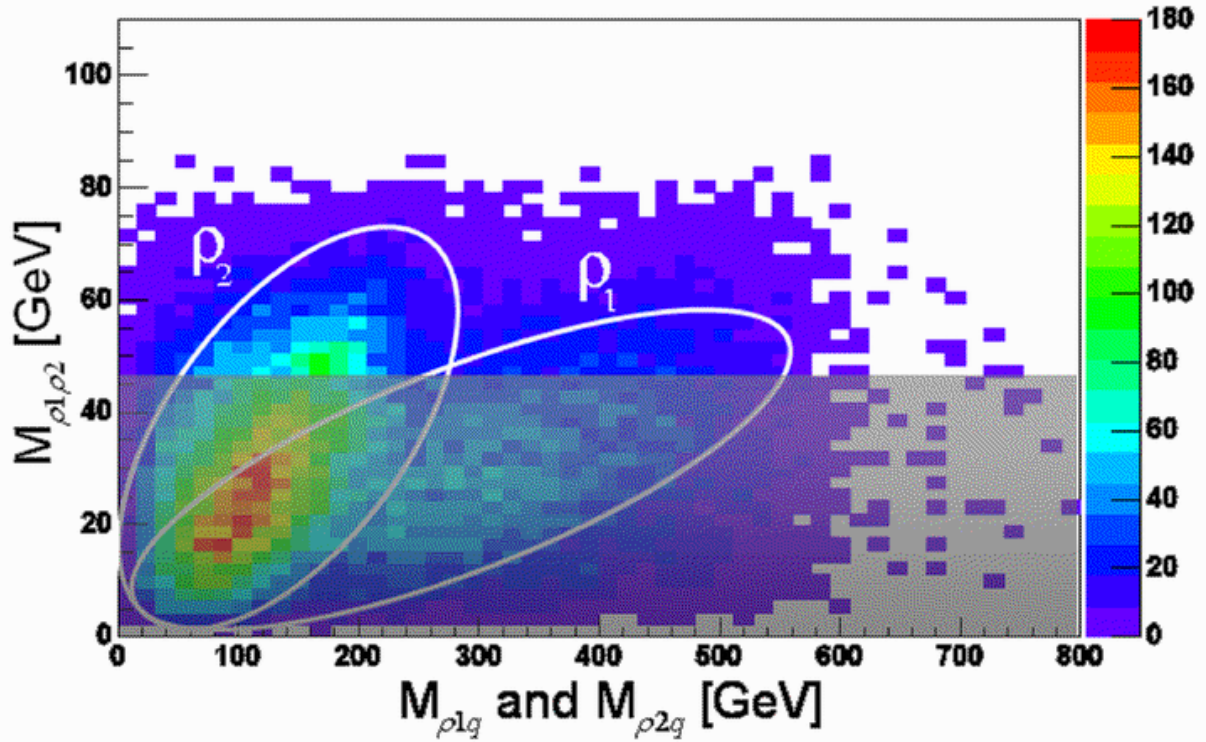


Figure 6.21: The invariant mass of both opposite-sign rho mesons versus the invariant mass of a single rho with the associated quark in GeV. It is an example for the point I'. The right ellipse denotes the events with the first rho whereas the left ellipse includes the second rho events. The lower $M_{\rho^\pm q}$ endpoint is determined from the events with $M_{\rho^\pm\rho^\mp} > 46$ GeV (unshaded region).

The linear fit method has to be adapted to this case. In order to find the endpoint on the background two linear fits are necessary. The first fit with the fit function $f(M_{INV})$ is defined the same way as in section 6.2.3 except that the chosen region is from 95% to 45% with respect

to the maximum bin content. The second fit with the fit function $g(M_{INV})$ iteratively searches the area right of the second lepton peak where the slope is bigger than -0.2 for a fit over seven bins. The minimal slope and the number of bins have been optimised for a stable second fit. The aim of this method is to find the second endpoint on the invariant mass distribution of the first rho with the associated quark. Here, the endpoint Ep_i^M is defined as the intercept point of both linear fits which are shown in figure 6.24. If the two linear fit functions are defined by

$$f(M_{INV}) = A \cdot M_{INV} + B \quad (6.10)$$

$$g(M_{INV}) = C \cdot M_{INV} + D \quad (6.11)$$

the measured endpoint Ep_i^M is given by the intersection of f and g :

$$Ep_i^M = \frac{D_i - B_i}{A_i - B_i} \quad (6.12)$$

The associated statistical uncertainty is:

$$\begin{aligned} (\delta_{stat} Ep^M)^2 &= \frac{\delta_{DD}^i + \delta_{BB}^i}{(A_i - C_i)^2} + \frac{(D_i - B_i)^2 \cdot (\delta_{AA}^i + \delta_{CC}^i)}{(A_i - C_i)^4} \\ &+ 2 \frac{(D_i - B_i)^2 \cdot \delta_{CD}^i \delta_{AB}^i}{(A_i - C_i)^3} \end{aligned} \quad (6.13)$$

The values δ_{XY}^i are the entries of the error matrix which contains the correlated statistical uncertainties on A , B , C and D . Since g and f are not correlated the elements δ_{AC}^i , δ_{AD}^i , δ_{BC}^i and δ_{BD}^i are zero. The result of this method is that the measured endpoint is for every point in the parameter space too low (Figure 6.25). A correction S of 26.8 ± 8.0 GeV has to be added. The actually needed correction here has the same m_0 dependence as that in $M_{\rho^\pm \rho^\mp}$ which can be seen in figure 6.26.

The gaussian method here remains the same except that the symmetric area for the fit changes from 25 % to 45 % of the centre bin value in order to achieve better results. The reason for this change is that the peak here has a smaller width. As can be seen in figure 6.27 it is reasonable to assume a linear dependence of Ep_i^T on $G_i \pm \delta G_i$. If the origin is chosen to be fixed the slope C of the fit is 1.7. If the ordinate value is a free parameter the slope C decreases to 1.5 with $D = 22.7$. The ratio between both slopes is 1.1.

The calculated uncertainties and the systematic shifts for the linear and both gaussian methods are given in table 6.9 .

Value	Linear	Gaussian FO	Gaussian NFO
$\delta_{stat} Ep^M$	4.6	3.0	2.7
S	26.8	-3.9	0.1
δS	8.0	9.9	2.9

Table 6.9: A summary of the calculated mean uncertainties and systematic shifts in GeV for the second $M_{\rho^\pm q}$ endpoint. FO is with fixed origin and NFO with non-fixed origin as described in section 6.2.3.

When the second endpoint is determined it can be used to make a cut on the measured invariant mass in order to select solely first rho events. The uncertainty of that cut value has no effect on the following results since the tail of the distribution is not dependent on the cut. The only important aspect is that the fit algorithm for the linear fit takes the maximum of the first rho distribution and not the maximum of the second rho distribution. For the following analysis data samples of between 5142 and 16963 events after the cut have been used. The

large difference of the events in the data samples is caused by the very different ratio between both endpoint masses. However, the relevant number in the fitted region is in all data samples of the same magnitude. The theoretical first rho endpoints are shown in figure 6.30. In the investigated area the maximum of the first rho plus associated quark distribution is very close to the endpoint concerning the second rho. Therefore, it is only possible to make a linear fit at the tail of the distribution. An example is given in figure 6.31. The systematic shift here is compared to the previous cases with 1.8 ± 2.4 GeV (Figure 6.32) relatively small. Furthermore there is no significant m_0 and $m_{1/2}$ dependence on that shift which can be seen in figure 6.33.

<i>Value</i>	Linear
$\delta_{stat} Ep^M$	1.7
S	1.8
δS	2.4

Table 6.10: A summary of the calculated correction and the mean uncertainties in GeV for the first endpoint in $M_{\rho^\pm q}$.

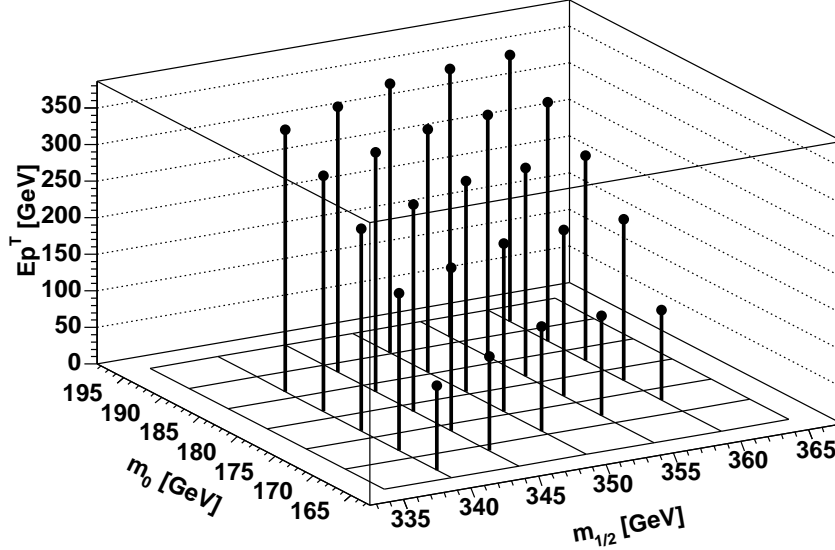


Figure 6.22: Theoretical kinematic endpoints in GeV for the invariant mass of the second rhos coming from the $\tilde{\tau}^\pm$ and the associated light quark coming from the squark in the $\tilde{s}_1, \tilde{d}_1 \rightarrow s, d + \tilde{\chi}_2^0$ decay. The endpoints decrease significantly for decreasing values of m_0 .

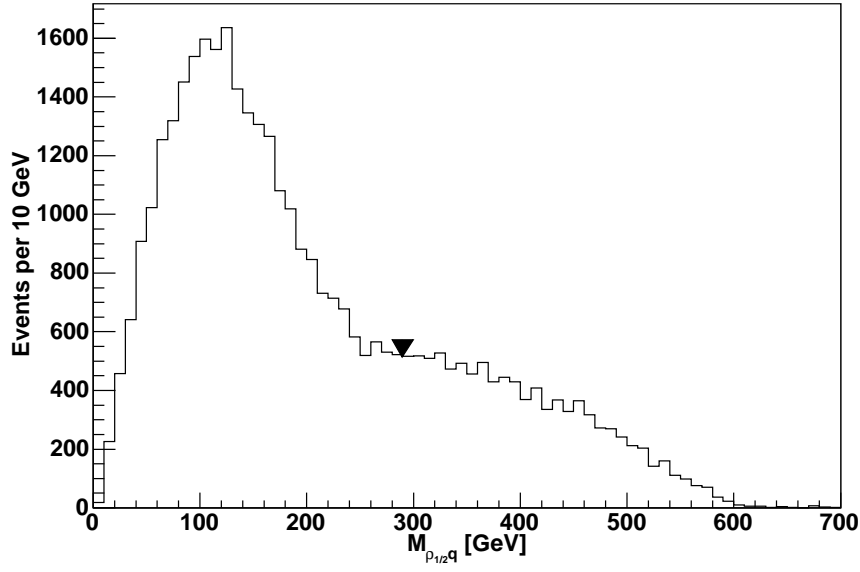


Figure 6.23: Example for the invariant mass $M_{\rho^\pm q}$ distribution at $m_0 = 181$ and $m_{1/2} = 350$ before the cut on $M_{\rho^\pm \rho^\mp}$. In this distribution 37428 events are represented. The triangle shows the theoretical kinematic endpoint of $M_{\rho_2^\pm q}$ at 288.0 GeV.

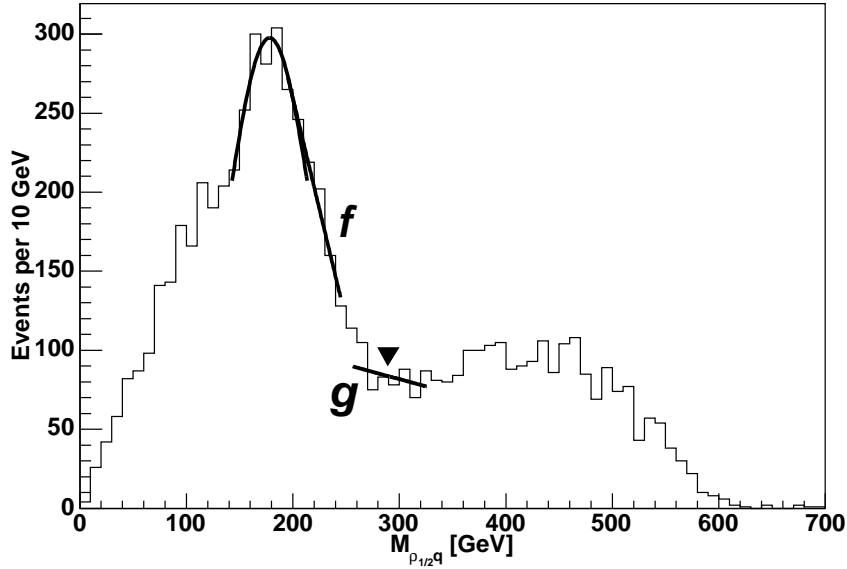


Figure 6.24: Example for the two linear fits f and g and the gaussian fit at $m_0 = 181$ and $m_{1/2} = 350$. In this distribution 6904 events after the cut (55%) on $M_{\rho^\pm \rho^\mp}$ are represented. The triangle shows the theoretical kinematic endpoint of $M_{\rho_2^\pm q}$ at 288.0 GeV.

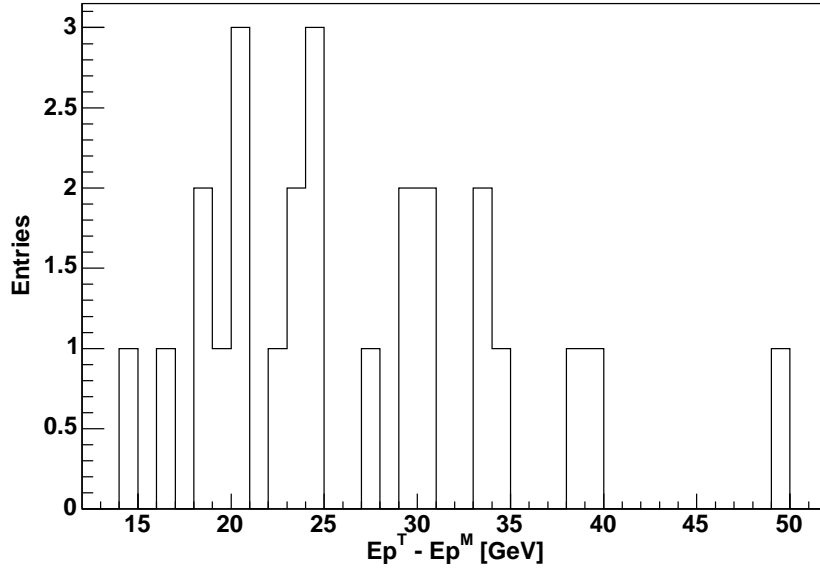


Figure 6.25: The difference of the theoretical and the measured $M_{\rho_2^\pm q}$ endpoint obtained with the linear fit in GeV for all 25 points. It shows a shift of 26.8 GeV with a root-mean-square deviation of 8.0 GeV.

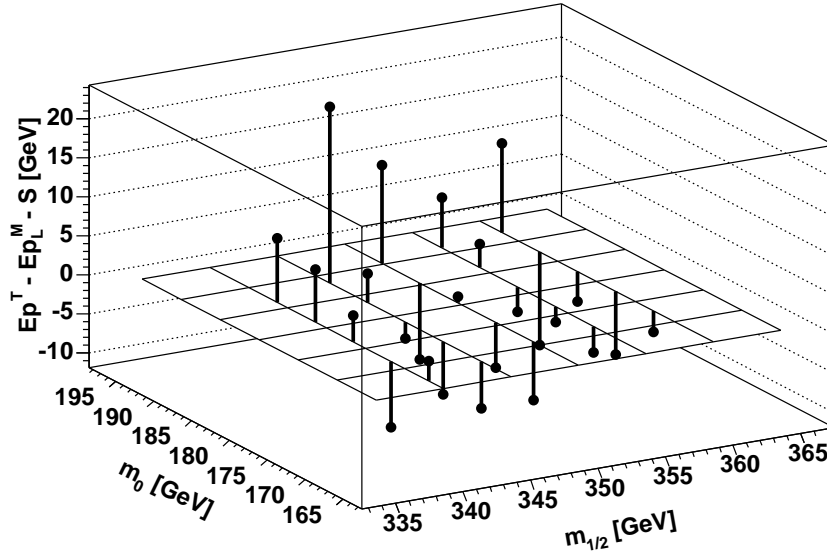


Figure 6.26: The theoretical $M_{\rho_2^\pm q}$ endpoint minus the measured endpoint obtained with the linear fit in GeV after applying the constant correction of 26.8 GeV. The values decrease significantly for decreasing values of m_0 .

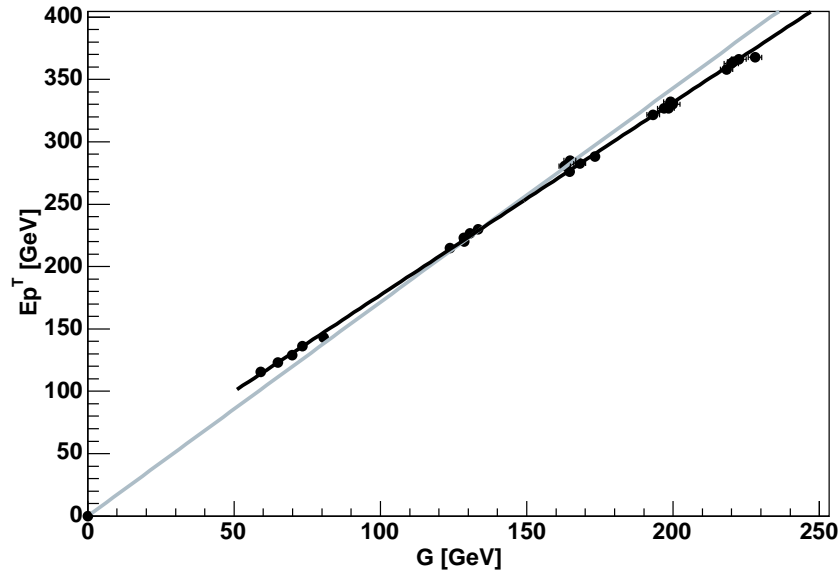


Figure 6.27: The theoretical kinematic endpoints of $M_{\rho_2^\pm q}$ as a function of the measured gaussian maximum for all 25 investigated points in the m_0 - $m_{1/2}$ plane. The gray line is forced to go through the origin whereas the black has an optimised ordinate value of 22.7 GeV.

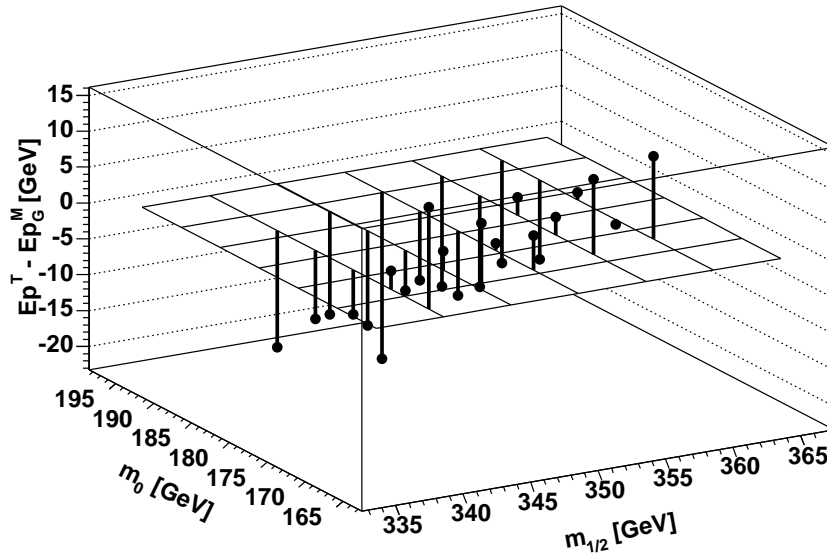


Figure 6.28: The difference of the theoretical and the measured $M_{\rho_2^\pm q}$ endpoint in GeV obtained with the gaussian fixed origin method. The measured values are on average too large by 9.1 GeV

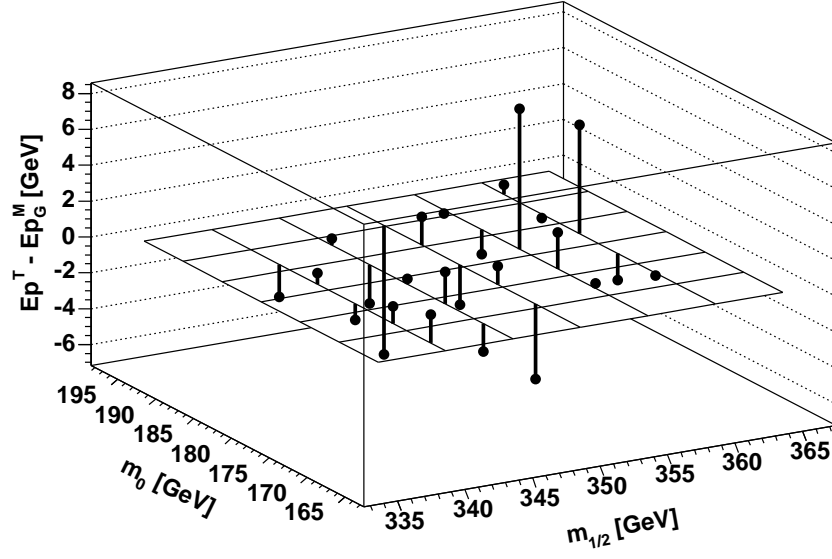


Figure 6.29: The difference of the theoretical and the measured $M_{\rho_2^\pm q}$ endpoint in GeV obtained with the gaussian non-fixed origin method.

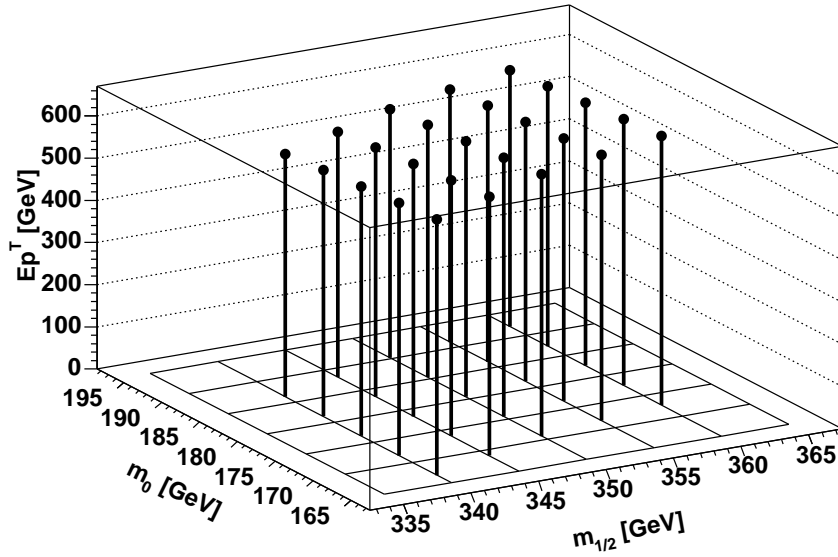


Figure 6.30: Theoretical kinematic endpoints in GeV for the invariant mass of first rho coming from the $\tilde{\chi}_2^0$ and the associated light quark coming from the squark in the $\tilde{s}_1, \tilde{d}_1 \rightarrow s, d + \tilde{\chi}_2^0$ decay.

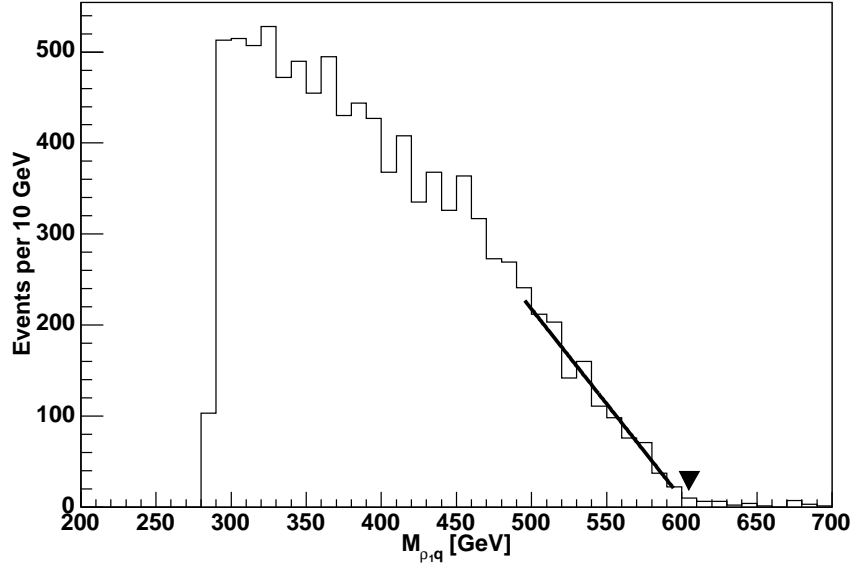


Figure 6.31: Example for the linear fit at $m_0 = 181$ and $m_{1/2} = 350$ after applying a cut on the invariant mass $M_{\rho^\pm q}$ at the theoretical second endpoint value. In this example 9855 events are represented. The triangle shows the theoretical kinematic endpoint of $M_{\rho_1^\pm q}$ at 606.0 GeV.

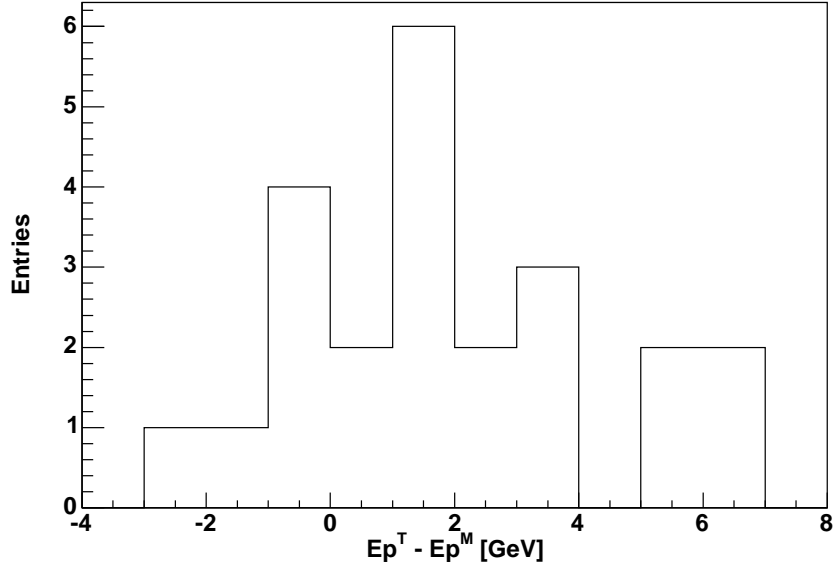


Figure 6.32: The difference of the theoretical and the measured $M_{\rho_1^\pm q}$ endpoint in GeV obtained with a linear fit for all 25 points. It shows a shift of 1.8 GeV with a root-mean-square deviation of 2.4 GeV.

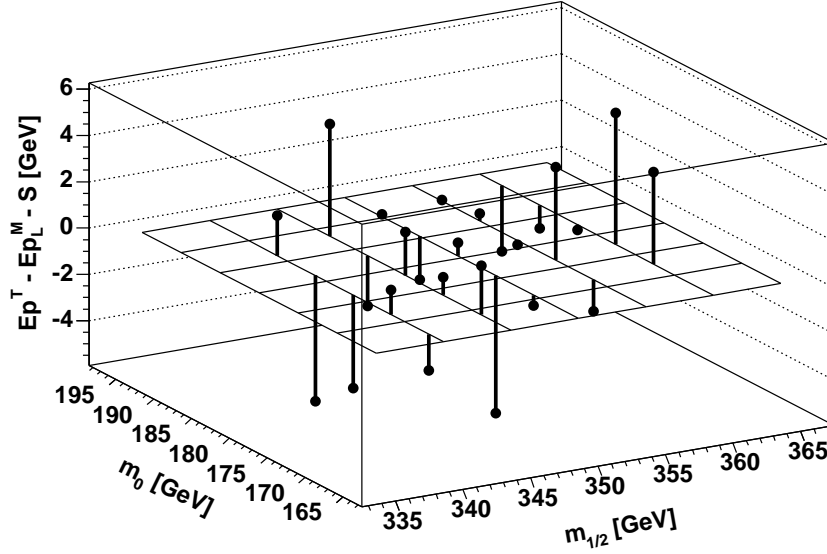
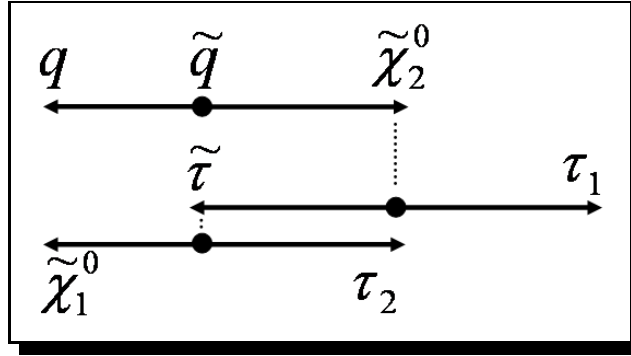


Figure 6.33: The theoretical $M_{\rho_1^\pm q}$ endpoint minus the measured endpoint in GeV obtained with the linear fit after applying the constant correction of 1.8 GeV. The uncertainties show no significant m_0 or $m_{1/2}$ dependence. Thus, a constant correction is sensible in this case.

6.2.9 The kinematic limit of $M_{\rho_1^\pm q} + M_{\rho_2^\mp q}$ for light quarks



If all endpoints could be measured very precisely four measured kinematic limits would be enough to reconstruct the four sparticle masses $M_{\tilde{\chi}_1^0}$, $M_{\tilde{\chi}_2^0}$, $M_{\tilde{\tau}}$ and $M_{\tilde{d},\tilde{s}}$. But mainly due to the neutrinos even at parton level there are large statistical and systematic uncertainties for the measured endpoints. Although this fifth endpoint (Figure 6.34) depends on the previous four endpoints, its measurement improves significantly the uncertainties for the mass reconstruction which is performed in section 6.2.16. For the following analysis the same data sample as in section 6.2.7 is chosen.

The linear fit (Figure 6.35) measures the endpoints systematically too low by 51.4 ± 12.8 GeV as can be seen in figure 6.36. The same m_0 dependence on the actually needed correction as has been determined for $M_{\rho^\pm \rho^\mp}$ or $M_{\rho^\pm \rho^\mp q}$ is shown in figure 6.37.

Figure 6.38 illustrates that the gaussian method is suitable to determine the endpoint. Even if the fit is forced to go through the origin, which leads to a slope value $C = 1.9$, good results

can be achieved. If the fit can optimise the ordinate value the slope C decreases to 1.3 with $D = 254.3$ GeV. The calculated values for the uncertainties and the systematic shifts are given in table 6.11.

<i>Value</i>	Linear	Gaussian FO	Gaussian NFO
$\delta_{stat} Ep^M$	1.9	7.4	5.0
S	51.4	-2.3	0.4
δS	12.8	13.2	5.6

Table 6.11: A summary of the calculated mean uncertainties and systematic shifts in GeV for the $M_{\rho_1^\pm q} + M_{\rho_2^\mp q}$ endpoint analysis. FO denotes the results with fixed origin and NFO with non-fixed origin.

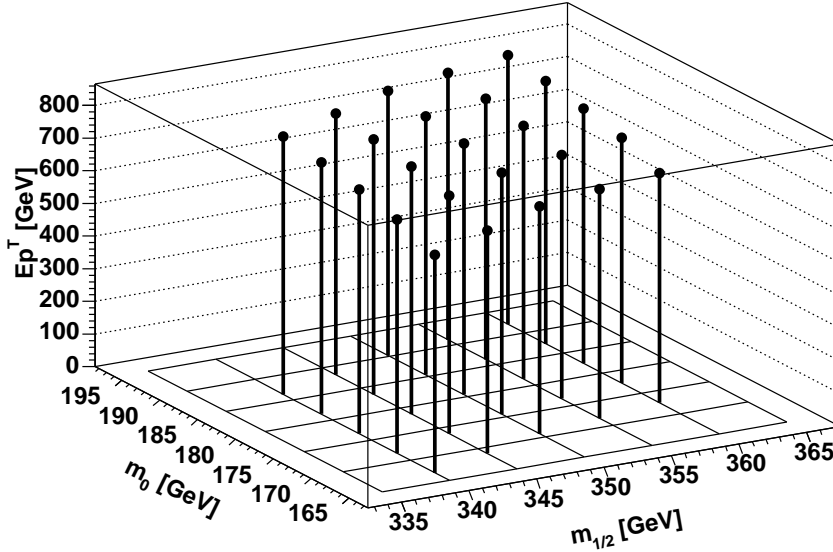


Figure 6.34: Theoretical kinematic endpoints for $M_{\rho_1^\pm q} + M_{\rho_2^\mp q}$ in GeV: The ρ_2^\mp coming from the $\tilde{\tau}$ with the light quark and the ρ_1^\pm coming from the $\tilde{\chi}_2^0$ and the same light quark from $\tilde{s}_1, \tilde{d}_1 \rightarrow s, d + \tilde{\chi}_2^0$.

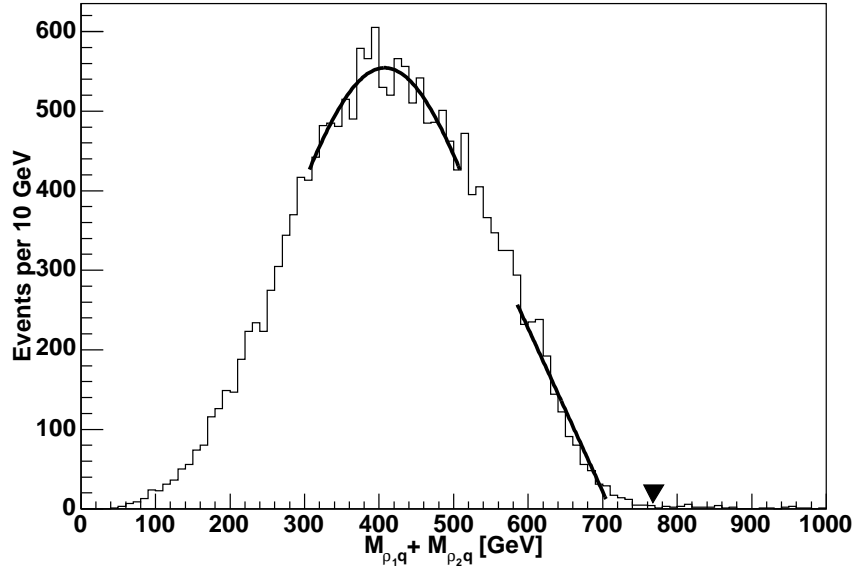


Figure 6.35: Example for the linear and the gaussian fit to the $M_{\rho_1^\pm q} + M_{\rho_2^\mp q}$ distribution at $m_0 = 181$ and $m_{1/2} = 350$. In this distribution 18714 events are represented. The triangle shows the theoretical kinematic endpoint at 768.8 GeV.

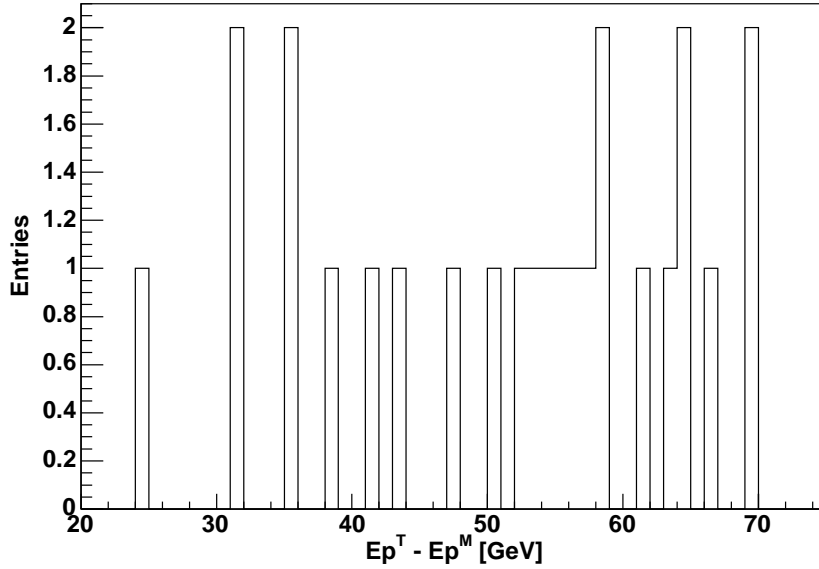


Figure 6.36: The difference of the theoretical and the measured $M_{\rho_1^\pm q} + M_{\rho_2^\mp q}$ endpoint in GeV obtained with a linear fit for all 25 points. It shows a large shift of 51.4 GeV with a root-mean-square deviation of 12.8 GeV.

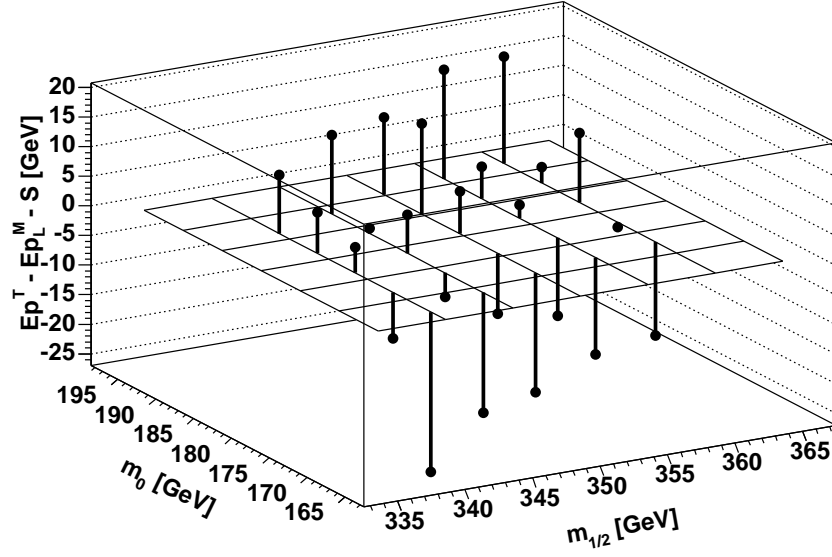


Figure 6.37: The theoretical $M_{\rho_1^\pm q} + M_{\rho_2^\mp q}$ endpoint minus the measured endpoint in GeV obtained with the linear fit after applying the constant correction of 51.4 GeV. The values decrease significantly for decreasing values of m_0 .

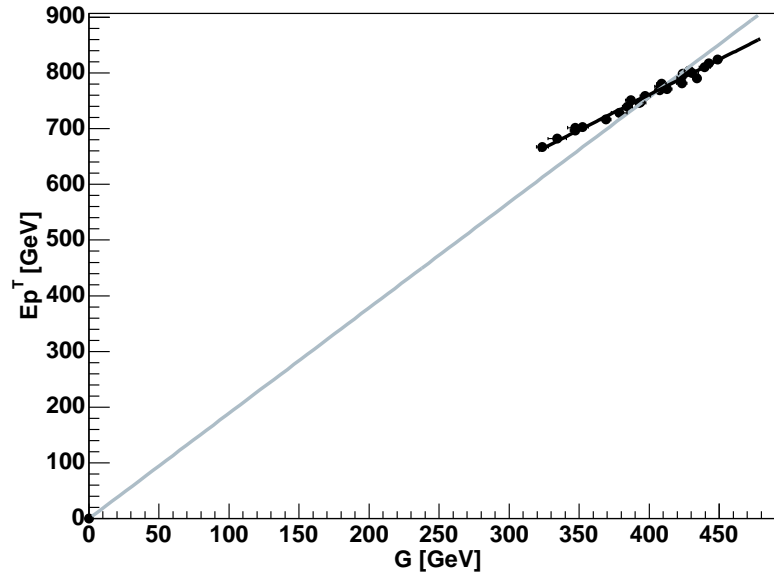


Figure 6.38: The theoretical kinematic $M_{\rho_1^\pm q} + M_{\rho_2^\mp q}$ endpoints as a function of the measured gaussian maximum for all 25 investigated points in the m_0 - $m_{1/2}$ plane. The gray fit with $C = 1.9$ is forced to go through the origin whereas the black with $C = 1.3$ has an optimised ordinate value of 254.3 GeV.

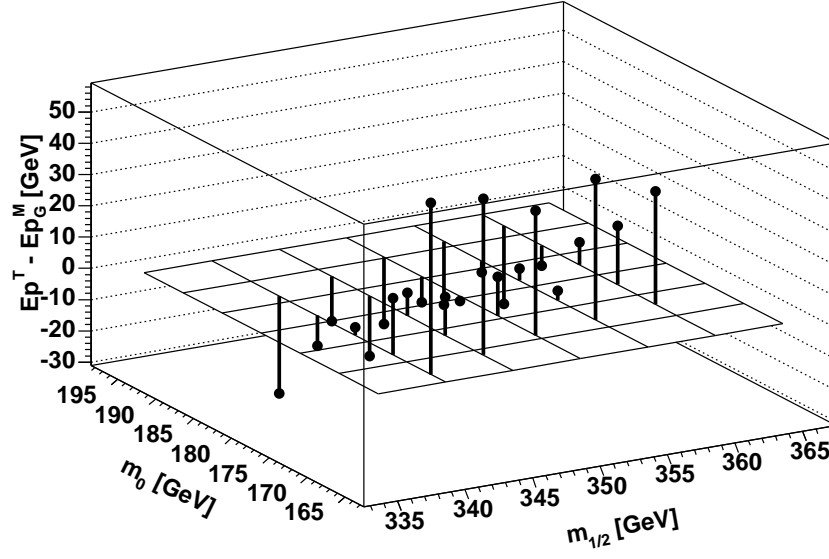


Figure 6.39: The difference of the theoretical and the measured $M_{\rho_1^\pm q} + M_{\rho_2^\mp q}$ endpoint in GeV obtained with the gaussian fixed origin method. The measured values are too high with a systematic shift of 2.3 GeV

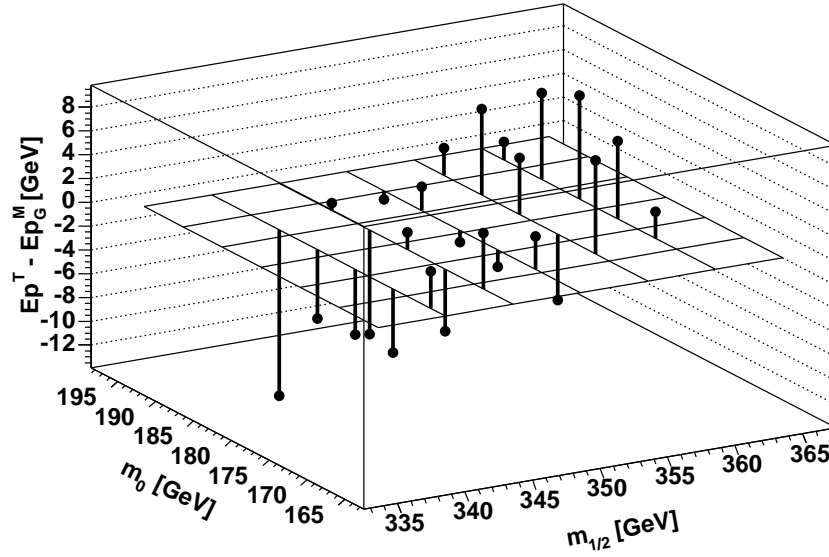
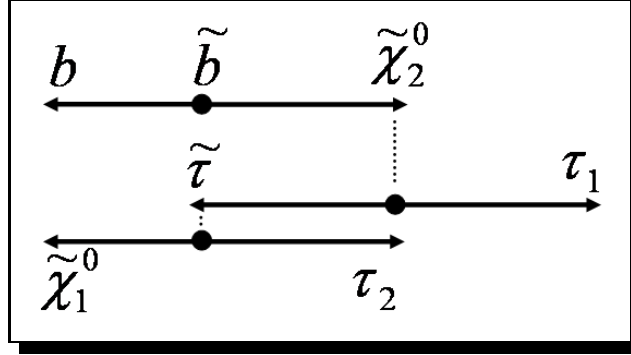


Figure 6.40: The difference of the theoretical $M_{\rho_1^\pm q} + M_{\rho_2^\mp q}$ endpoint and the measured endpoint in GeV obtained with the gaussian non-fixed origin method.

6.2.10 The kinematic limit of $M_{\rho^\pm \rho^\mp q}$ for bottom quarks



Indeed, with the b-tagging it is possible to select events with bottom quarks. But the top quark which is used in the sections 6.2.13 to 6.2.15 decays almost entirely into bottom quarks such that the b-tagging is also sensitive to top events. Nevertheless, there is a possibility to distinguish both kinds of events, as shown in figure 6.41. In the invariant mass distribution of both opposite-sign rho mesons versus the invariant mass of a single rho with the associated top or bottom quark, both kinds of events are well separated. Both processes are treated separately in the following. The analysis in this section is based on 25 data samples with between 4224 and 4901 bottom quark events.

For the kinematic limit of $M_{\rho^\pm \rho^\mp b}$, which is shown in figure 6.42 for all 25 points, the gaussian method cannot be applied for two reasons. First, the shape of the distribution changes significantly within the investigated region. In some cases the region around the maximum of the distribution is flat, resulting in a large χ^2 for the gaussian fit. Second, when applying the gaussian fit on the distribution the maximum value shows no linear dependence on the theoretical endpoint. This can be seen in figure 6.46.

On the other hand, the linear fit (Figure 6.43) provides a good possibility to measure the $M_{\rho^\pm \rho^\mp b}$ endpoint. However, a large systematic correction (Figure 6.44) is needed because there are about six to seven times more events with the lighter \tilde{b}_1 than with the heavier \tilde{b}_2 being responsible for the real kinematic endpoint. This can easily be understood by comparing table 6.1 with table 6.4. The effect of this mixing is shown and explained in figure 6.47. The same m_0 dependence as in previous cases for the actually needed correction can be seen in figure 6.45.

Value	Linear
$\delta_{stat} E p^M$	2.9 (2.9)
S	50.3 (7.2)
δS	8.5 (8.6)

Table 6.12: A summary of the calculated correction and mean uncertainties in GeV. The values in brackets correspond to the case of \tilde{b}_1 being the input for the kinematic limit.

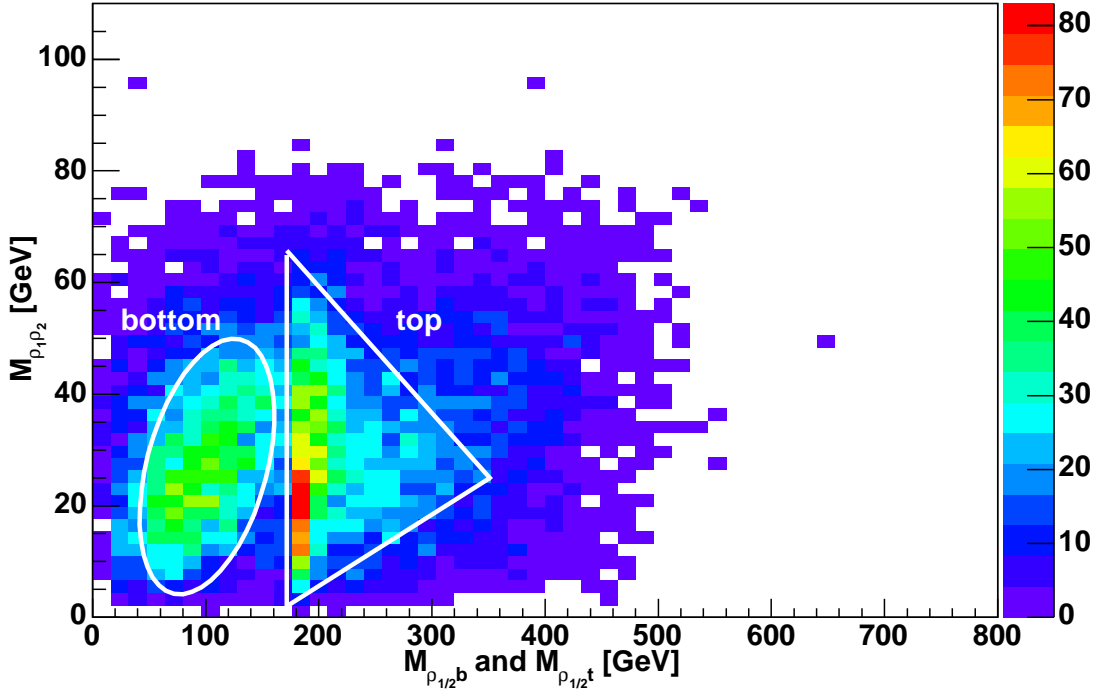


Figure 6.41: The invariant mass of both opposite-sign rho mesons versus the invariant mass of a single rho with the associated top or bottom quark in GeV. It is an example for the point I'. The left ellipse denotes the events with the bottom quarks whereas the top quark events are mainly located in the triangle on the right side.

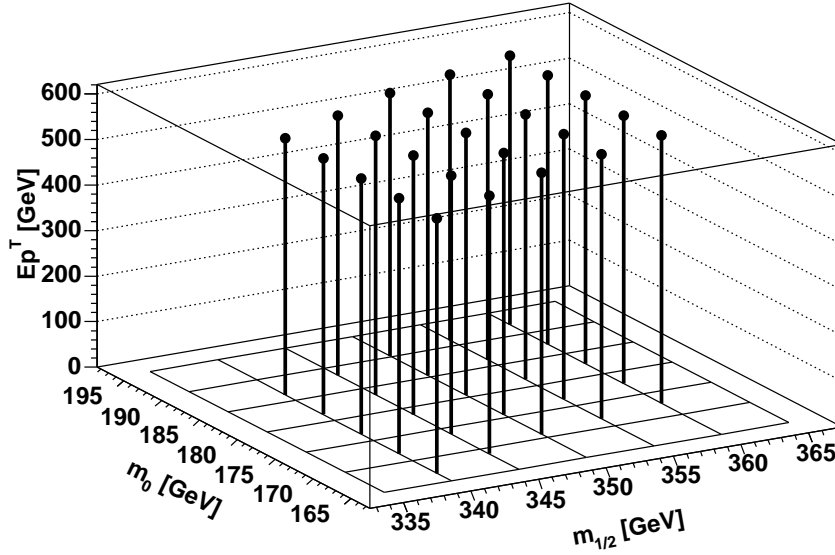


Figure 6.42: Theoretical kinematic endpoints in GeV of the invariant mass of both opposite-sign rhos, coming from the $\tilde{\chi}_2^0$ and the $\tilde{\tau}$ respectively, and the associated quark from $\tilde{b}_2 \rightarrow b + \tilde{\chi}_2^0$.

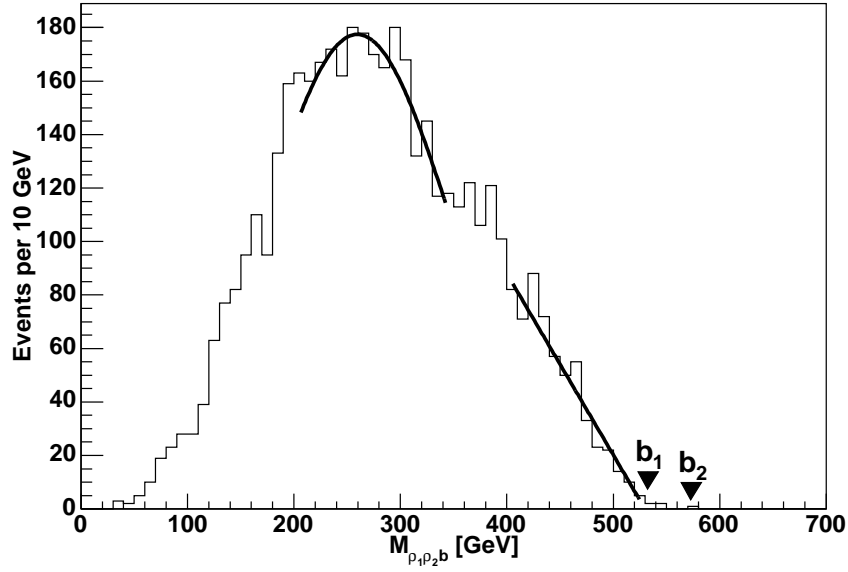


Figure 6.43: Example for the linear and the gaussian fit to the $M_{\rho^\pm\rho^\mp b}$ distribution at $m_0 = 181$ and $m_{1/2} = 350$. The invariant mass distribution is based on 4498 bottom quark events. The two triangles show the theoretical endpoint values for events with \tilde{b}_1 (532.9 GeV) and \tilde{b}_2 (576.3 GeV), respectively.

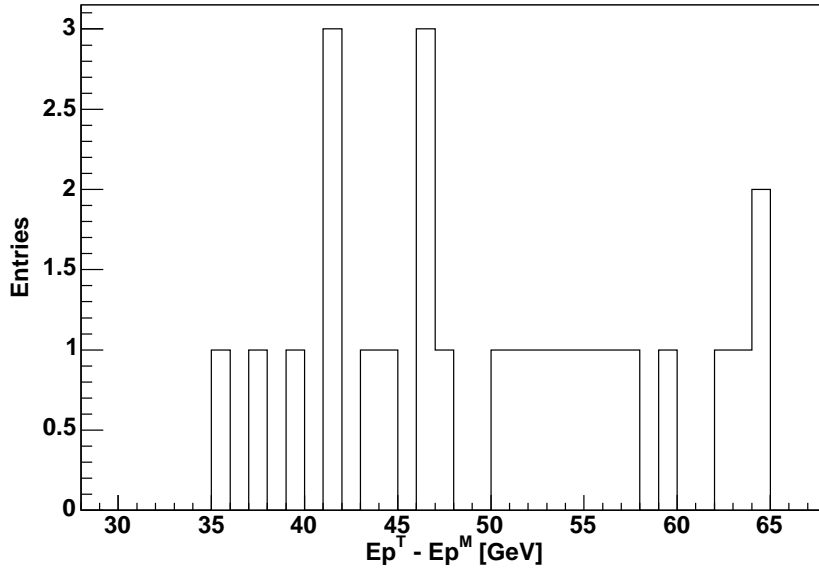


Figure 6.44: The theoretical $M_{\rho^\pm\rho^\mp b}$ endpoint minus the measured endpoint in GeV for all 25 points. The mean value S is 50.3 GeV with a root-mean-square deviation of 8.5 GeV. If the \tilde{b}_1 mass instead of the \tilde{b}_2 mass is taken for the theoretical endpoint the value S changes to 7.2 ± 8.6 GeV

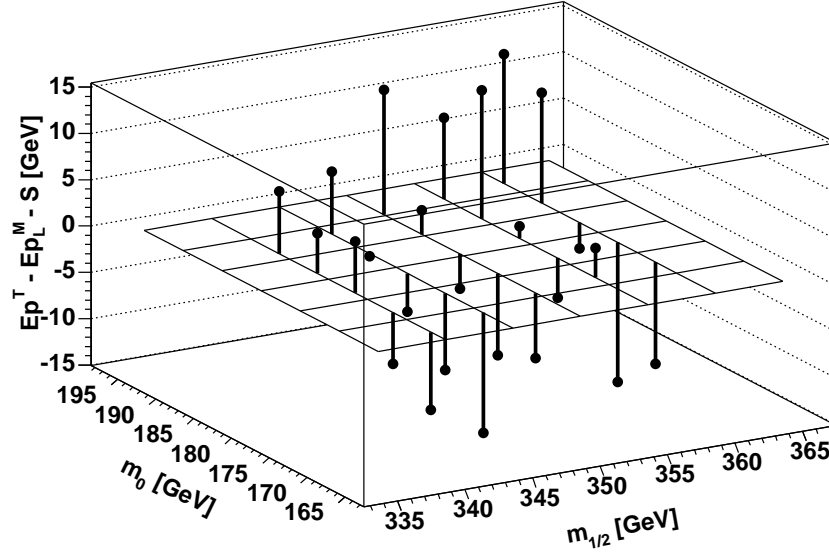


Figure 6.45: The theoretical $M_{\rho^\pm \rho^\mp b}$ endpoint minus the measured endpoint in GeV after applying a constant correction of 50.3 GeV. The values decrease with decreasing values of m_0 .

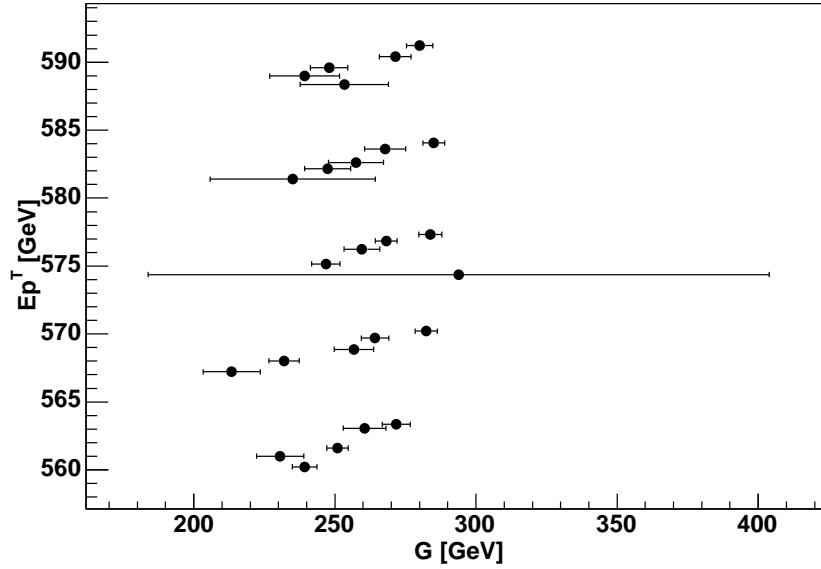


Figure 6.46: The theoretical kinematic $M_{\rho^\pm \rho^\mp b}$ endpoints versus the measured gaussian maximum for all 25 investigated points in the m_0 - $m_{1/2}$ plane. Due to the flat shape near the maximum of one distribution, one point shows a large uncertainty. A unique mapping of the measured maximum to the theoretical endpoint can not be established since several theoretical endpoint values are associated with the same measured maximum.

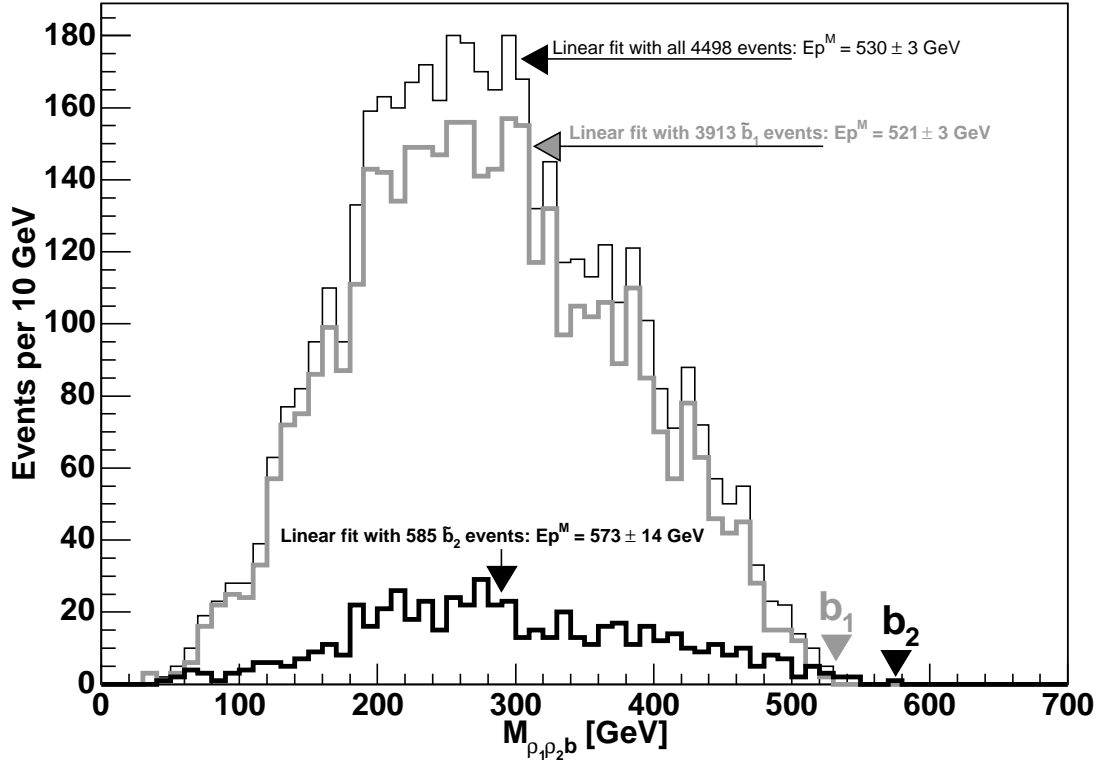
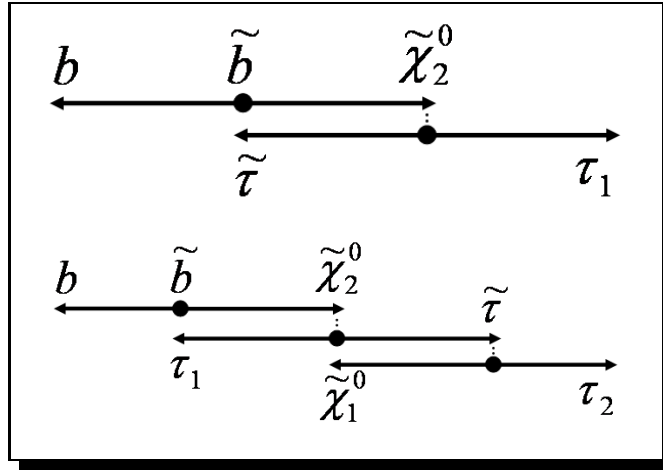


Figure 6.47: The invariant mass distribution of both rho with the associated bottom quark. The bold black line shows 585 events coming from a \tilde{b}_2 , the bold gray line 3913 events coming from a \tilde{b}_1 and the light black line shows the superposition of both lines. Although the \tilde{b}_1 events clearly dominate, the \tilde{b}_2 events have a significant influence on the measurement of $E p^M$. The triangles show the theoretical endpoints at 533 GeV (\tilde{b}_1) and 576 GeV (\tilde{b}_2).

6.2.11 Two kinematic limits in $M_{\rho^{\pm}q}$ for bottom quarks



The principles described in section 6.2.8 remain the same for this invariant mass distribution. In the following only the necessary changes and the results are described. The region for the

gaussian fit is changed from a symmetric area of 25% of the bin value which is used for the fitting centre to a symmetric area of 45% similar to section 6.2.8. The gaussian method for this distribution can be applied since the gaussian fit is stable for all 25 points and the assumed linear dependence is sensible (see figure 6.52). If the linear fit of Ep_i^T as a function of the fitted gaussian maximum $G_i \pm \delta G_i$ is forced to go to the origin the resulting slope C is 2.3. The statistical uncertainty $\delta_{stat} Ep^M$ on the endpoint measurement has then a mean value of 4.9 GeV. However, in this case a systematic shift S of -8.3 ± 14.1 GeV is needed in the whole region to improve the endpoint measurement (see figure 6.53). If the fit is not restricted to intersect the origin the value C changes to 2.1, nearly no systematic shift S is needed and δS decreases to 6.0 GeV. The fit here intersects the ordinate at $D = 21.6$ GeV. The mean statistical uncertainty $\delta_{stat} Ep^M$ on the endpoint measurement decreases slightly to 4.3 GeV. The ratio between both slopes is 1.1.

For the double linear fit method the second fit iteratively searches the area right of the second lepton peak where the slope is bigger than -0.25 , instead of -0.2 like in section 6.2.8. This value leads to a stable fit over the whole investigated parameter space. This method here again has the problem that a large shift of 46.9 ± 10.3 GeV is needed. However, it can be used to estimate the endpoint. Table 6.13 summarises the results.

<i>Value</i>	Linear	Gaussian FO	Gaussian NFO
$\delta_{stat} Ep^M$	5.8 (5.8)	4.9	4.3
S	46.9 (28.7)	-8.3	0.2
δS	10.3 (7.7)	14.1	6.0

Table 6.13: A summary of the calculated mean uncertainties and systematic shifts in GeV for the second endpoint in $M_{\rho^{\pm}b}$. FO is with fixed origin and NFO with non-fixed origin.

The endpoint for the first rho with the associated bottom quark is determined with a linear fit (Figure 6.56) the same way as it is described in section 6.2.8. In figure 6.55 the theoretical value is shown which corresponds to events coming from the \tilde{b}_2 . In figure 6.57 the large systematic shift $S = 36.5 \pm 3.7$ GeV can be seen. There is no significant m_0 and $m_{1/2}$ dependence on that shift as shown in figure 6.58. This is similar to the first $M_{\rho^{\pm}q}$ endpoint for the light quarks (Figure 6.33).

<i>Value</i>	Linear
$\delta_{stat} Ep^M$	2.6 (2.6)
S	36.5 (-4.8)
δS	3.9 (3.7)

Table 6.14: A summary of the calculated correction and mean uncertainties in GeV for the first endpoint in the $M_{\rho^{\pm}q}$ distribution.

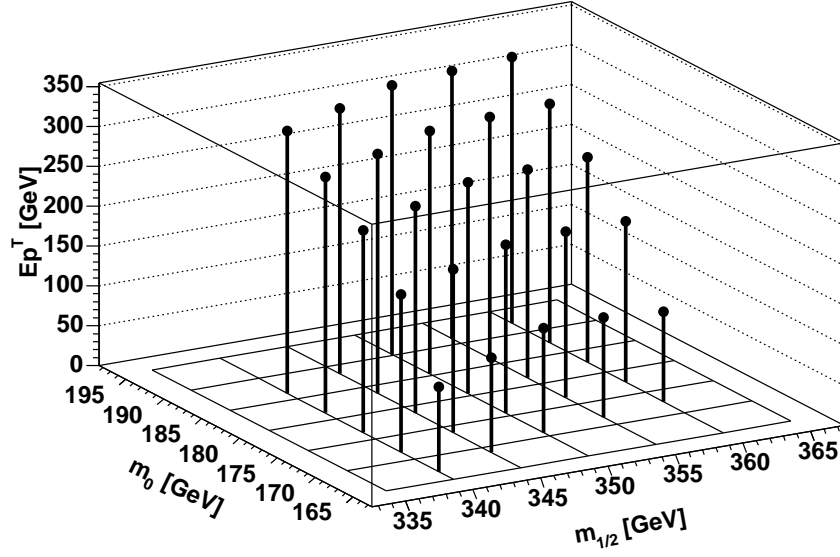


Figure 6.48: Theoretical kinematic endpoints in GeV for the invariant mass of the second rho coming from the $\tilde{\tau}^\pm$ and the associated bottom quark coming from the sbottom in the $\tilde{b}_2 \rightarrow b + \tilde{\chi}_2^0$ decay. The endpoints decrease significantly for decreasing values of m_0 .

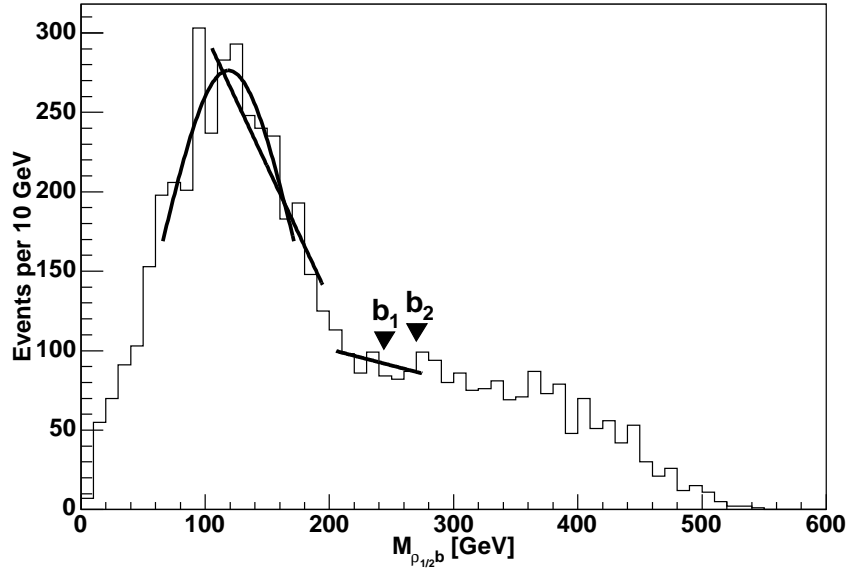


Figure 6.49: Example for the two linear fits and the gaussian fit to the $M_{\rho^\pm b}$ distribution at $m_0 = 181$ and $m_{1/2} = 350$. In this distribution 5636 events after the cut at 30% of the maximum invariant mass of both rhos (see section 6.2.8) are represented. The two triangles show the theoretical endpoint values for events with \tilde{b}_1 (244.7 GeV) and \tilde{b}_2 (264.5 GeV), respectively.

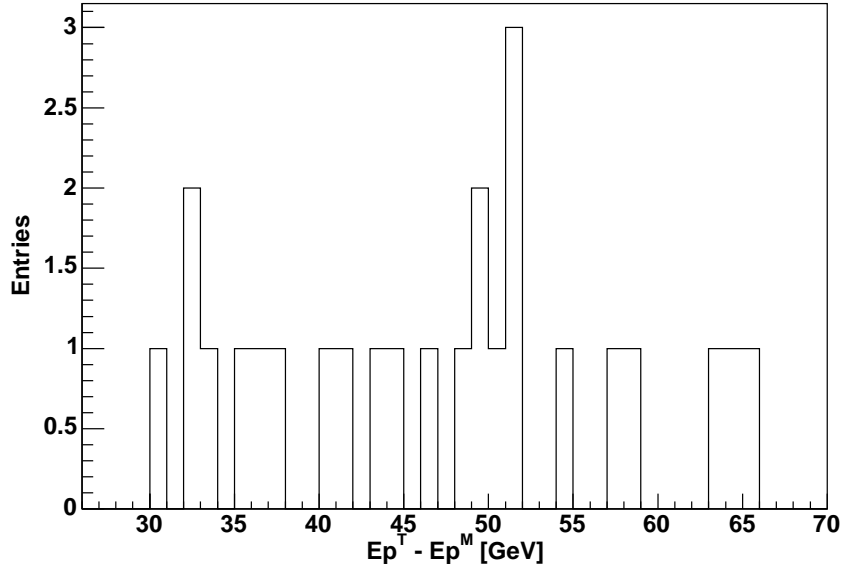


Figure 6.50: The difference of the theoretical and the measured $M_{\rho_2^{\pm}b}$ endpoint in GeV obtained with the linear fit for all 25 points. It shows a shift of 46.9 GeV with a root-mean-square deviation of 10.3 GeV.

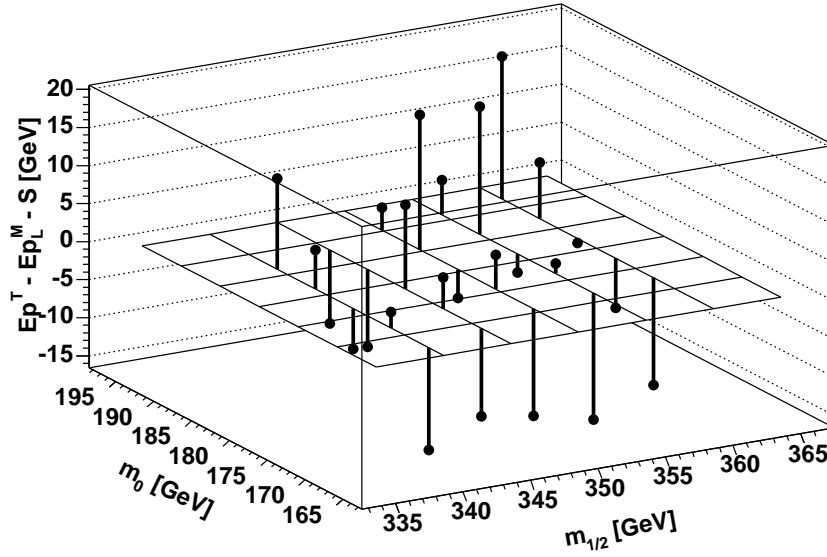


Figure 6.51: The theoretical $M_{\rho_2^{\pm}b}$ endpoint minus the measured endpoint in GeV obtained with the linear fit after applying the constant correction of 46.9 GeV.

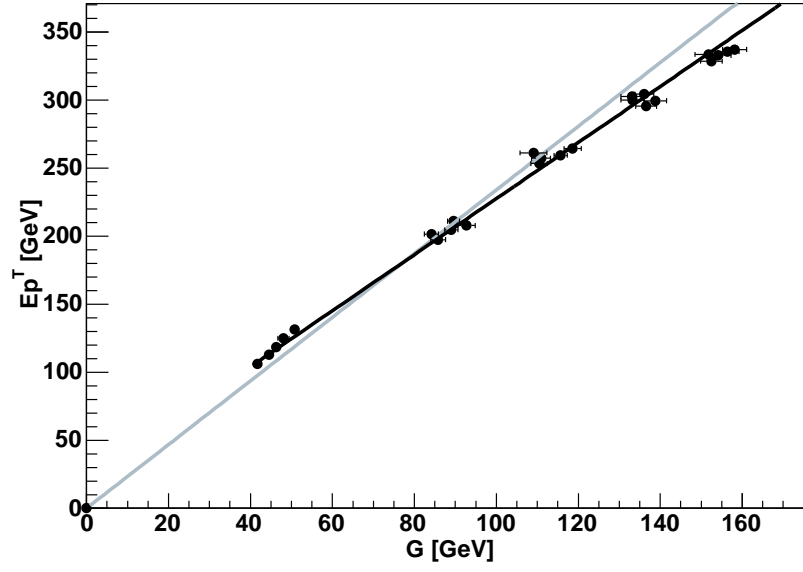


Figure 6.52: The theoretical kinematic $M_{\rho_2^{\pm}b}$ endpoints as a function of the measured gaussian maximum for all 25 investigated points in the m_0 - $m_{1/2}$ plane. The gray line is forced to go through the origin whereas the black has an optimised ordinate value of 21.6 GeV.

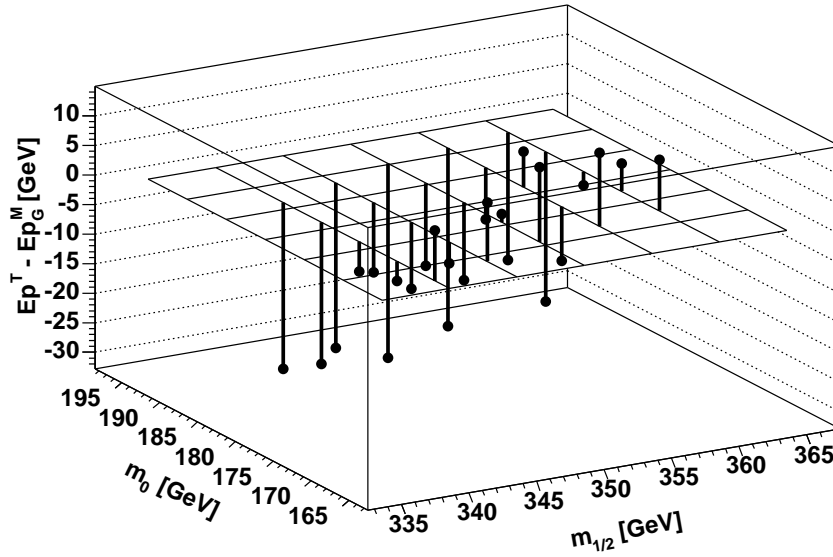


Figure 6.53: The difference of the theoretical and the measured $M_{\rho_2^{\pm}b}$ endpoint in GeV obtained with the gaussian fixed origin method. The measured values are too low with a systematic shift of -8.3 GeV

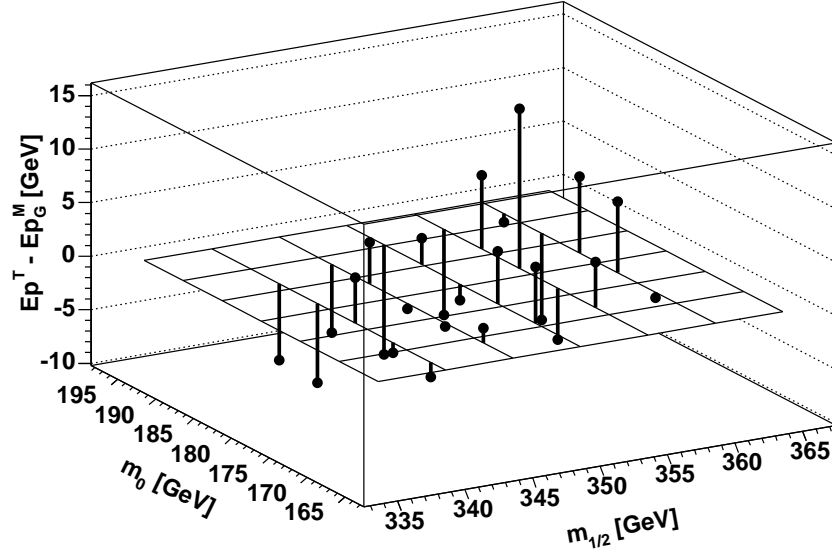


Figure 6.54: The difference of the theoretical and the measured $M_{\rho_2^\pm b}$ endpoint in GeV obtained with the gaussian non-fixed origin method.

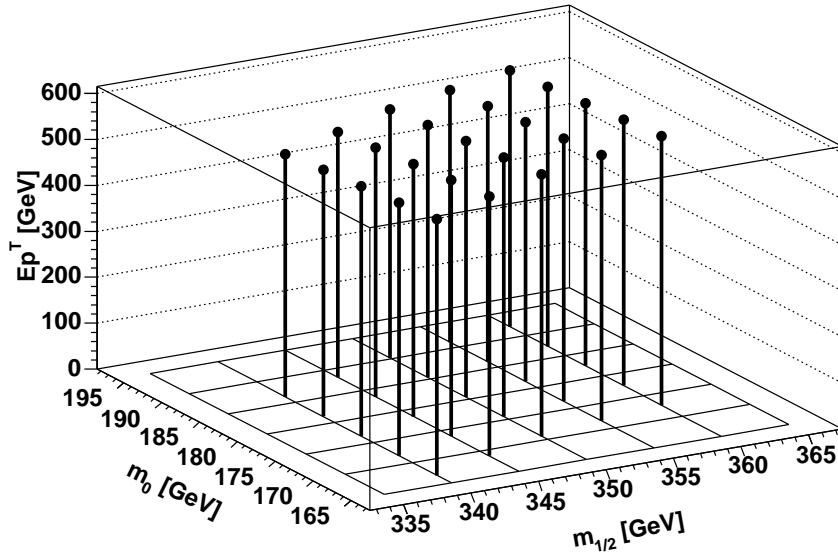


Figure 6.55: Theoretical kinematic endpoints in GeV for the invariant mass of first rho coming from the $\tilde{\chi}_2^0$ and the associated bottom quark coming from the sbottom in the $\tilde{b}_2 \rightarrow b + \tilde{\chi}_2^0$ decay.

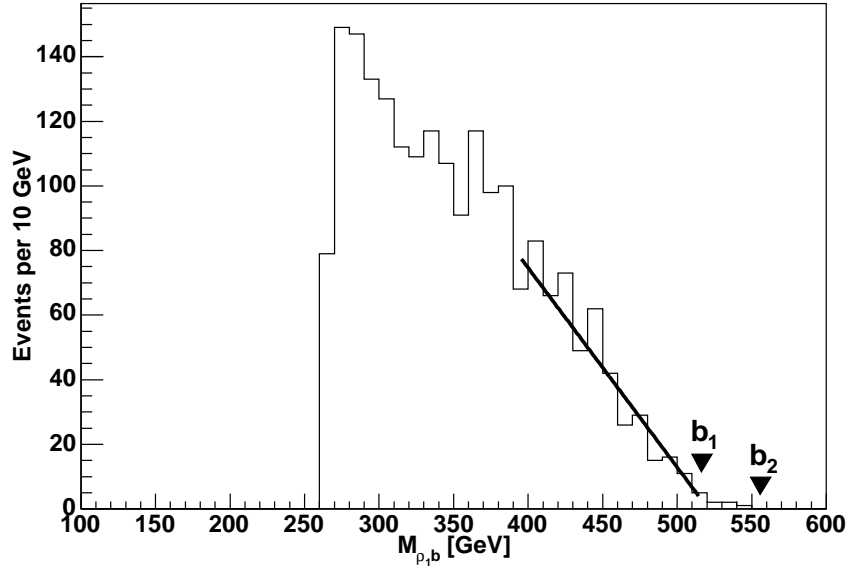


Figure 6.56: Example for the linear fit at $m_0 = 181$ and $m_{1/2} = 350$ after applying a cut on the invariant mass $M_{\rho^\pm b}$ at the second endpoint. In this distribution 2036 events are represented. The two triangles show the theoretical endpoint values for events with \tilde{b}_1 (514.7 GeV) and \tilde{b}_2 (556.4 GeV), respectively.

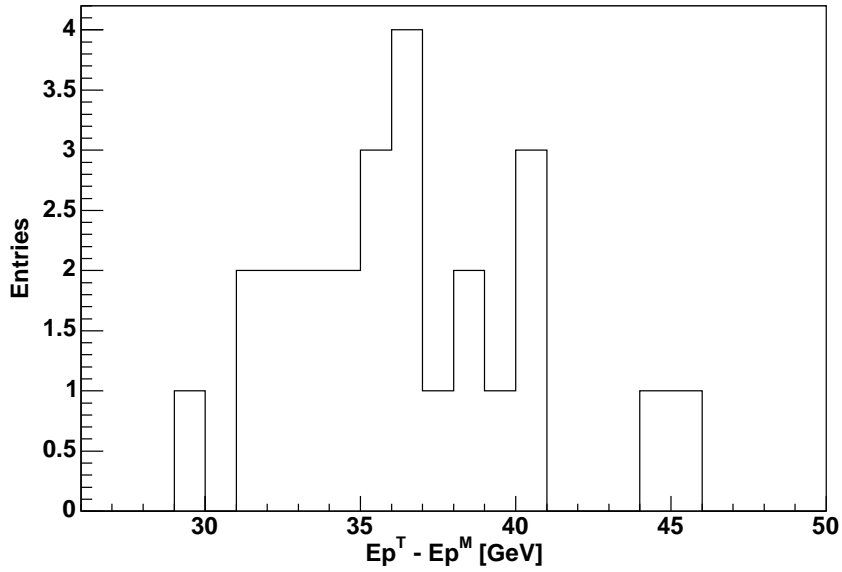


Figure 6.57: The difference of the theoretical and the measured $M_{\rho^\pm b}$ endpoint in GeV obtained with the linear fit. It shows a shift of 36.5 GeV with a root-mean-square deviation of 3.9 GeV.

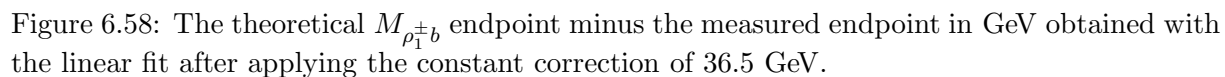


Diagram illustrating the construction of the effective action for the τ field. The diagram shows two horizontal lines representing the τ field. The top line has a left-pointing arrow labeled b and a right-pointing arrow labeled $\tilde{\chi}_2^0$. A black dot is on the top line, with a vertical dotted line extending downwards to a black dot on the bottom line. The bottom line has a left-pointing arrow labeled $\tilde{\chi}_1^0$ and a right-pointing arrow labeled τ_2 . A vertical dotted line also extends upwards from the bottom dot to the top dot. A label τ_1 is at the right end of the bottom line, and a label $\tilde{\tau}$ is next to the top dot.

For the linear fit the large correction $S = 89.3 \pm 15.1$ GeV is again caused by the origin of the bottom quark. A clear m_0 dependence can be seen in figure 6.62 which should be included into the correction. Similar to the light quark case the gaussian method can be applied as well. In order to achieve good results for the gaussian fit the symmetric area is chosen to be 35% of the maximum bin value. By comparing the two linear fits for the light quark gaussian case in figure 6.38 with the bottom quark gaussian case in figure 6.63 an interesting similarity can be found. In both cases the ratio between the slope in the fixed origin fit and the slope in the non-fixed origin fit has an universal value of 1.5. A summary of the measured values is given in table 6.15.

<i>Value</i>	Linear	Gaussian FO	Gaussian NFO
$\delta_{stat} E p^M$	3.2 (3.2)	9.7	6.5
S	89.3 (37.2)	6.2	1.0
δS	15.1 (12.6)	21.3	6.4

Table 6.15: A summary of the calculated mean uncertainties and systematic shifts in GeV for the $M_{\rho_1^\pm b} + M_{\rho_2^\mp b}$ distribution. FO is with fixed origin and NFO with non-fixed origin.

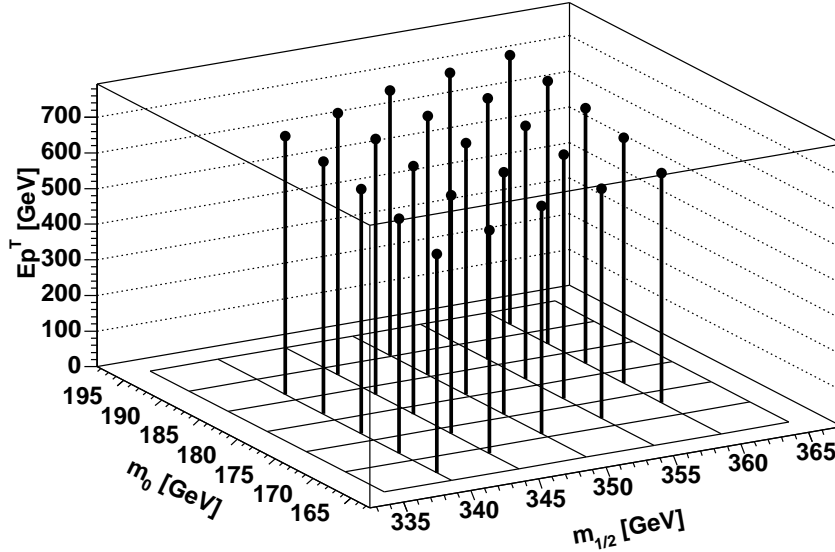


Figure 6.59: Theoretical kinematic endpoints for $M_{\rho_1^\pm b} + M_{\rho_2^\mp b}$ in GeV: The ρ_2^\mp coming from the $\tilde{\tau}$ with the bottom quark and the ρ_1^\pm coming from the $\tilde{\chi}_2^0$ and the same bottom quark from the $\tilde{b}_2 \rightarrow b + \tilde{\chi}_2^0$ decay.

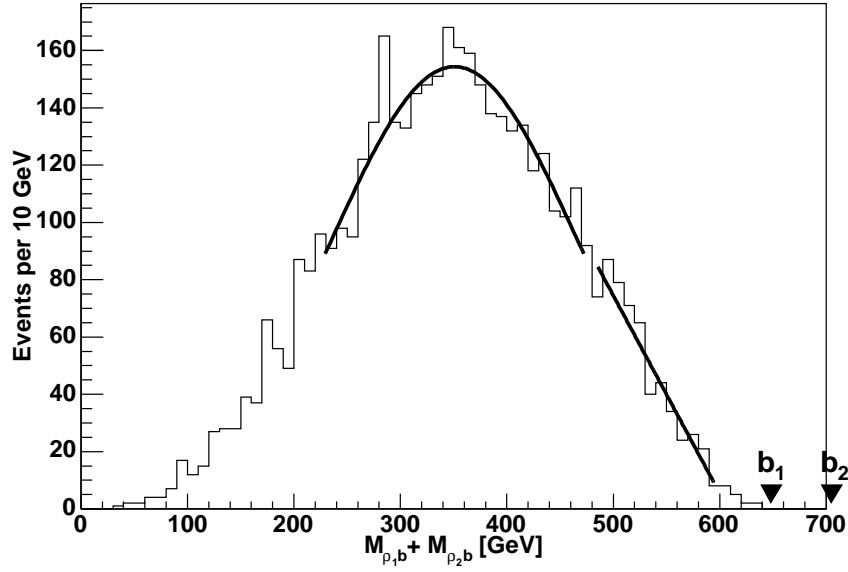


Figure 6.60: Example of a linear and a gaussian fit to the $M_{\rho_1^\pm b} + M_{\rho_2^\mp b}$ distribution at $m_0 = 181$ and $m_{1/2} = 350$. In this distribution 4498 events are represented. The two triangles show the theoretical values for events with \tilde{b}_1 (653.1 GeV) and \tilde{b}_2 (706.1 GeV), respectively.

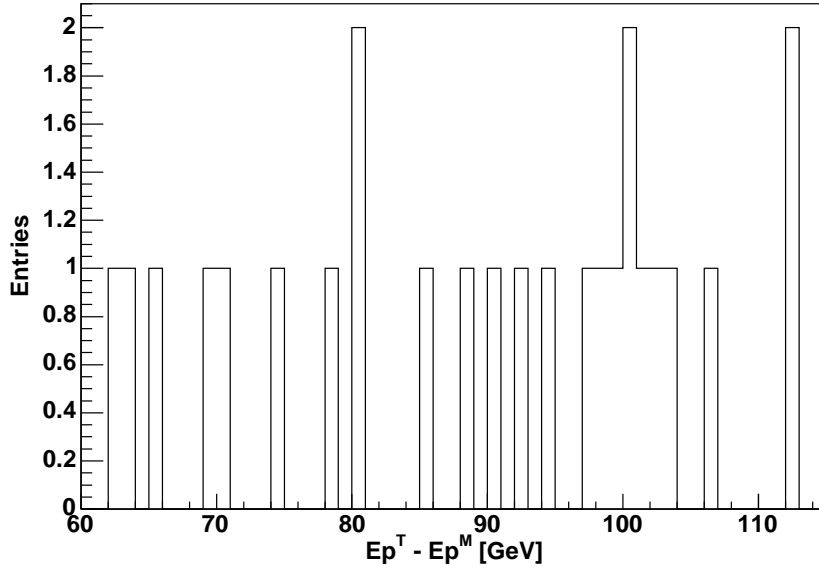


Figure 6.61: The difference of the theoretical and the measured $M_{\rho_1^\pm b} + M_{\rho_2^\mp b}$ endpoint in GeV obtained with the linear fit for all 25 points. It shows a large mean shift of 89.3 GeV with a root-mean-square deviation of 15.1 GeV.

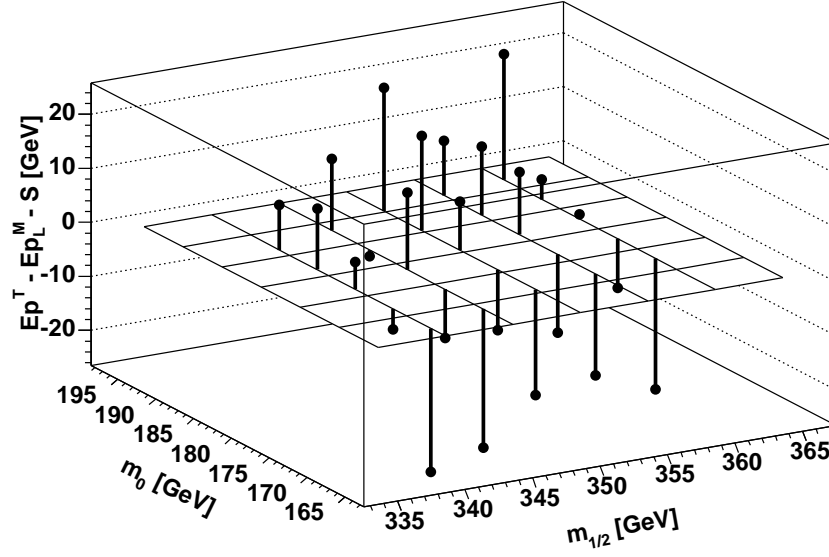


Figure 6.62: The theoretical $M_{\rho_1^\pm b} + M_{\rho_2^\mp b}$ endpoint minus the measured endpoint in GeV obtained with the linear fit after applying the constant correction of 89.3 GeV. The values decrease significantly for decreasing values of m_0 .

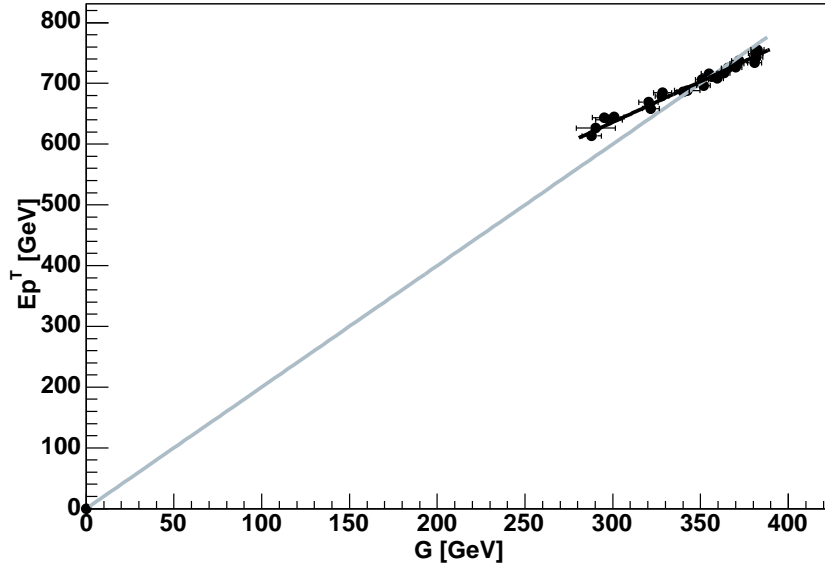


Figure 6.63: The theoretical kinematic $M_{\rho_1^\pm b} + M_{\rho_2^\mp b}$ endpoints as a function of the measured gaussian maximum for all 25 investigated points in the m_0 - $m_{1/2}$ plane. The gray line with $C = 2.0$ is forced to go through the origin whereas the black with $C = 1.3$ has an optimised ordinate value of 234.5 GeV.

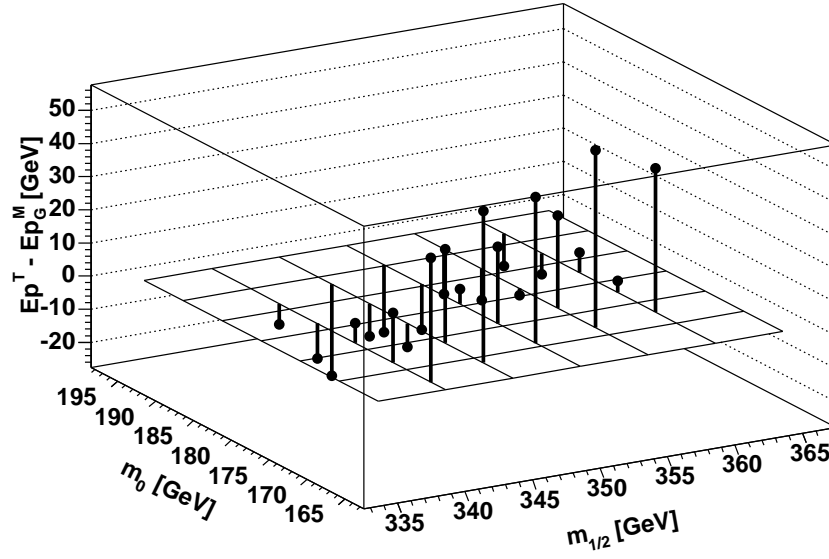


Figure 6.64: The difference of the theoretical and the measured $M_{\rho_1^\pm b} + M_{\rho_2^\mp b}$ endpoint in GeV obtained with the gaussian fixed origin method. The measured values are too low with a mean systematic shift of 6.2 GeV

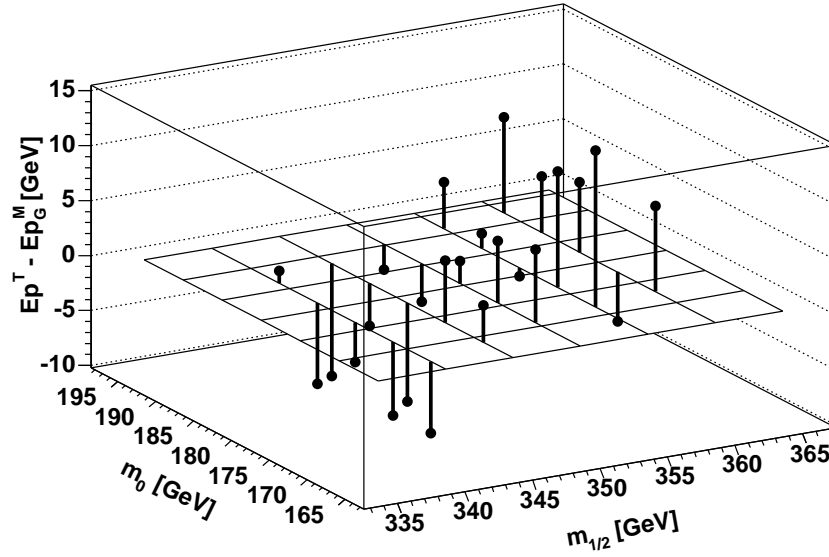
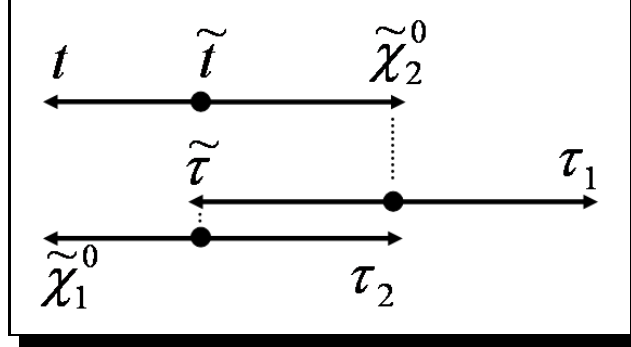


Figure 6.65: The difference of the theoretical and the measured $M_{\rho_1^\pm b} + M_{\rho_2^\mp b}$ endpoint in GeV obtained with the gaussian non-fixed origin method.

6.2.13 The kinematic limit of $M_{\rho^\pm \rho^\mp q}$ for top quarks



For the analysis of events with top quarks it is necessary to use the endpoint formulae given in section 5.3. The input for the upper limit is the mass of the \tilde{t}_2 and for the lower limit the lighter \tilde{t}_1 . For the following analysis 25 data samples with about 1750 events have been used. Similar to the previous cases, the gaussian method cannot be applied here which can be seen in figure 6.70. The lower kinematic limit which is given by formula (5.34) does not provide any information which can be used for the mass reconstruction since the theoretical value hardly depends on m_0 and $m_{1/2}$. It is 193.5 ± 0.1 GeV over the whole investigated area. The upper limit given by formula (5.33) varies from 586.7 GeV at $m_0 = 167$ and $m_{1/2} = 340$ to 615.1 GeV at $m_0 = 193$ and $m_{1/2} = 360$ which can be seen in figure 6.66. The linear fit gives the endpoint which arises from the \tilde{t}_1 mass with adequate precision. However, the real kinematic endpoint is given by the \tilde{t}_2 mass. Thus, a quite large correction S of 155.5 ± 5.7 GeV is necessary. The reason for this is the stop mixing. The principle is described in section 6.2.10 for the sbottom mixing.

Value	Linear
$\delta_{stat} Ep^M$	3.1 (3.1)
S	155.5 (0.4)
δS	5.7 (5.6)

Table 6.16: A summary of the calculated correction and mean uncertainties in GeV. The values in brackets correspond to the case of \tilde{t}_1 being the input for the upper kinematic limit.

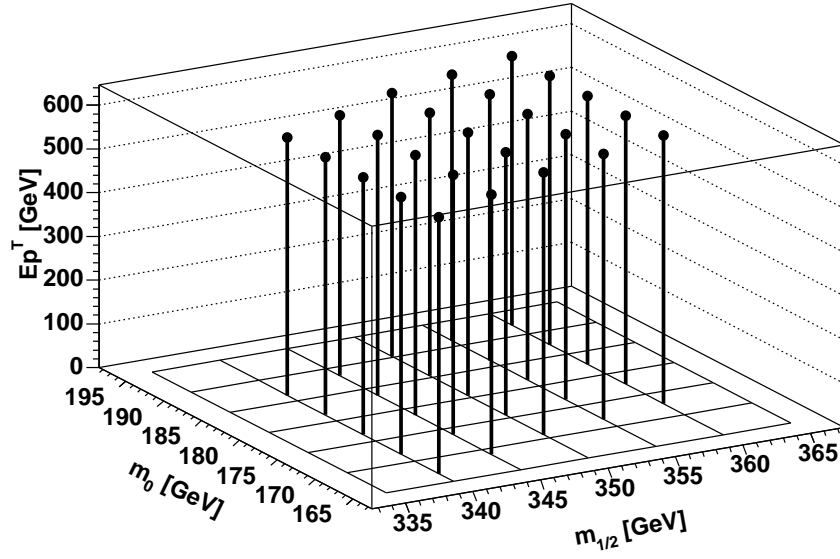


Figure 6.66: Theoretical kinematic endpoints in GeV for the invariant mass of both opposite-sign rhos, coming from the $\tilde{\chi}_2^0$ and the $\tilde{\tau}$ respectively, and the associated top quark from $\tilde{t}_2 \rightarrow t + \tilde{\chi}_2^0$.

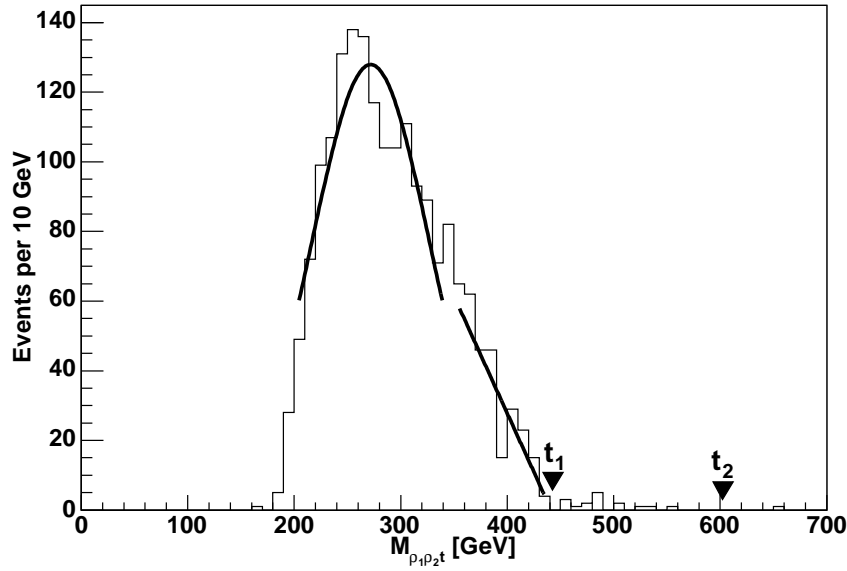


Figure 6.67: Example of a linear and a gaussian fit to the $M_{\rho^{\pm}\rho^{\mp}t}$ distribution at $m_0 = 181$ and $m_{1/2} = 350$. The invariant mass distribution is based on 1859 top quark events. The two triangles show the theoretical values for events with \tilde{t}_1 (446.1 GeV) and \tilde{t}_2 (601.2 GeV), respectively.

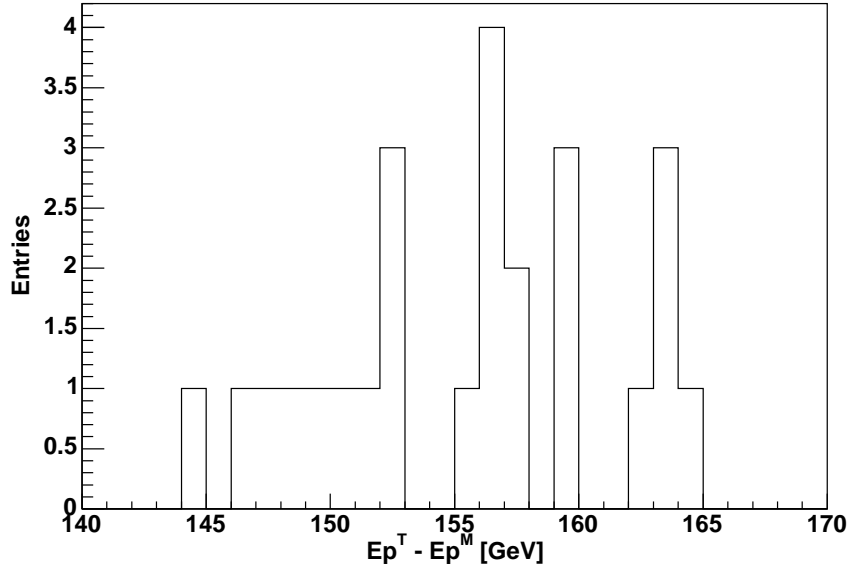


Figure 6.68: The theoretical $M_{\rho^\pm \rho^\mp t}$ endpoint minus the measured endpoint in GeV. The mean value S is 155.5 GeV with a root-mean-square deviation of 5.7 GeV. If the \tilde{t}_1 mass is taken for the theoretical endpoint the value S changes to 0.6 ± 5.6 GeV

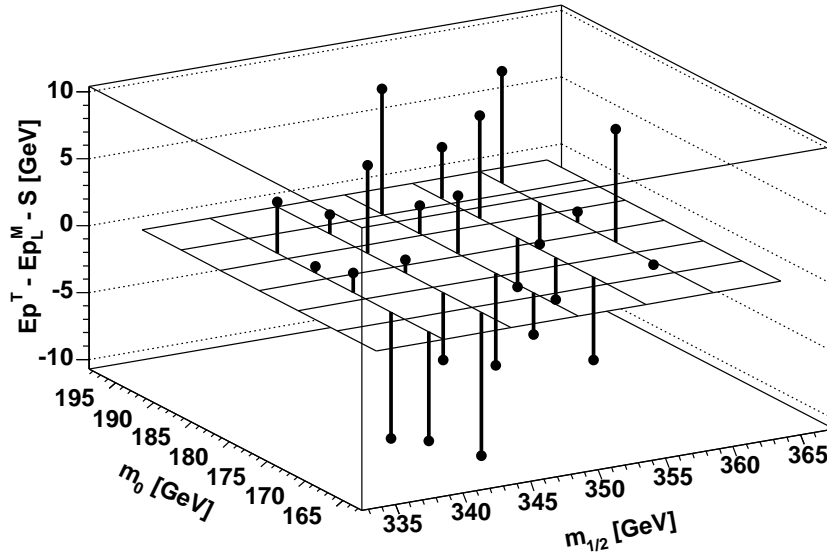


Figure 6.69: The theoretical $M_{\rho^\pm \rho^\mp t}$ endpoint minus the measured endpoint in GeV obtained with the linear fit after applying a constant correction of 155.5 GeV.

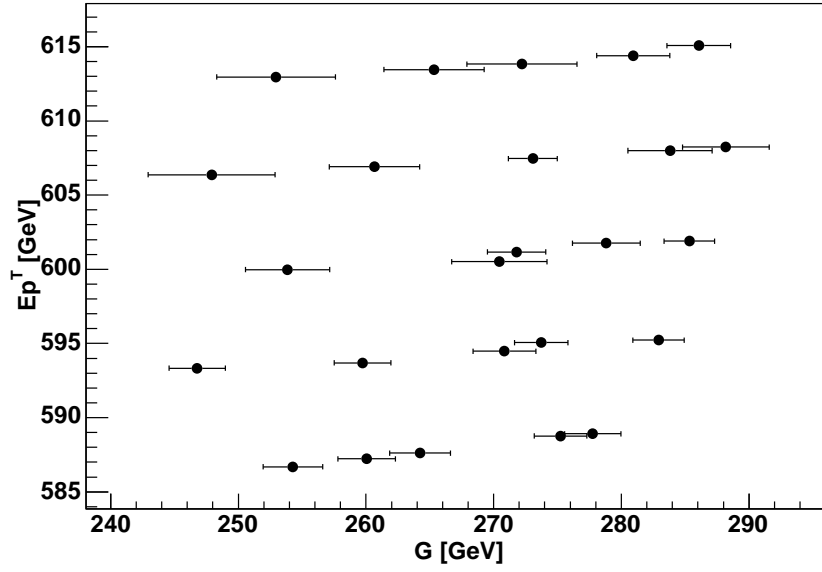
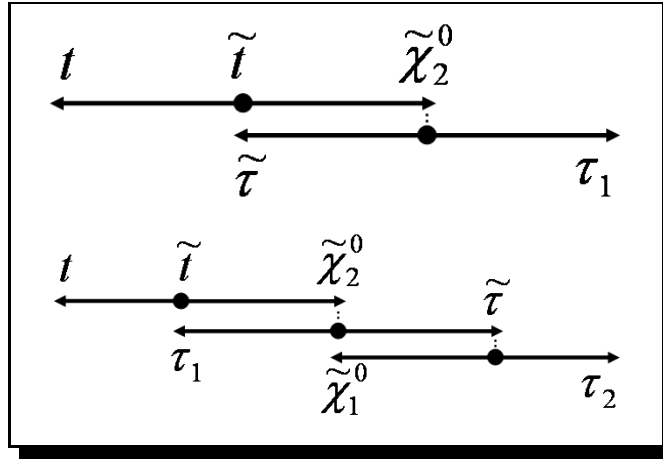


Figure 6.70: The theoretical kinematic $M_{\rho^\pm \rho^\mp t}$ endpoints versus the measured gaussian maximum for all 25 investigated points in the m_0 - $m_{1/2}$ plane. A unique mapping of the measured maximum to the theoretical endpoint can not be established since several theoretical endpoint values are associated with the same measured maximum.

6.2.14 Two kinematic limits in $M_{\rho^\pm q}$ for top quarks



The theoretical lower limit of the first rho with associated top quark distribution is constant at a value 192.4 ± 0.8 GeV and for the second it is 176.3 ± 0.7 GeV. The upper limit of the second distribution shown in figure 6.71 varies from 204.7 GeV at $m_0 = 167$ and $m_{1/2} = 340$ to 376.0 GeV at $m_0 = 193$ and $m_{1/2} = 360$. The linear fit method can in principal be applied in the area with a m_0 value around 170 GeV. However, for m_0 values around 190 GeV this is not possible, even if the cut at 30% of the invariant mass of both rhos is used. An example for the first case at $m_0 = 167$ and $m_{1/2} = 340$ is given in figure 6.72 and figure 6.73 shows an example of the latter at $m_0 = 187$ and $m_{1/2} = 340$. The gaussian method is applicable here as can be seen in figure 6.74. The only necessary change is that due to the large top mass the origin in

the Ep^T - G plane used in the previous sections has to be moved from (0,0) to (175,175). This is called hence the “adapted” origin. The formula (6.8) has to be changed to

$$Ep_i^T = C \cdot (G_i - 175) + D + 175. \quad (6.14)$$

If the adapted origin is fixed the slope C is 5.6. If it is not, it decreases to $C = 4.5$ with $D = 15.4$.

<i>Value</i>	Gaussian FO	Gaussian NFO
$\delta_{stat}Ep^M$	3.7	2.9
S	-14.6	-1.2
δS	21.6	6.8

Table 6.17: A summary of the calculated mean uncertainties and systematic shifts in GeV for $M_{\rho^{\pm t}}$ endpoint measurements. FO denotes the values with fixed adapted origin and NFO with non-fixed adapted origin.

The upper limit of the first distribution shown in figure 6.77 varies from 555.0 GeV at $m_0 = 187$ and $m_{1/2} = 340$ to 610.1 GeV at $m_0 = 173$ and $m_{1/2} = 360$. In order to achieve stable results the linear fit area has to start at the bin with 60% and ending at the bin with 5% of the maximum bin content. This change is necessary, because - due to the much lower statistics - for some points in the parameter space MINUIT [22] tries to fit a single bin. As can be seen in figure 6.78 the linear fit actually measures the endpoint given by the \tilde{t}_1 . Therefore also the shift S and its uncertainty for measuring this endpoint is given in table 6.18. Figure 6.79 and figure 6.80, however, show only the results for the real kinematic endpoint which is determined by \tilde{t}_2 .

<i>Value</i>	Linear
$\delta_{stat}Ep^M$	3.2 (3.2)
S	138.8 (-5.7)
δS	12.2 (4.2)

Table 6.18: A summary of the calculated mean uncertainties in GeV for the ρ_1^{\pm} endpoint in $M_{\rho^{\pm t}}$. The values in brackets correspond to the case of \tilde{t}_1 being the input for the kinematic limit.

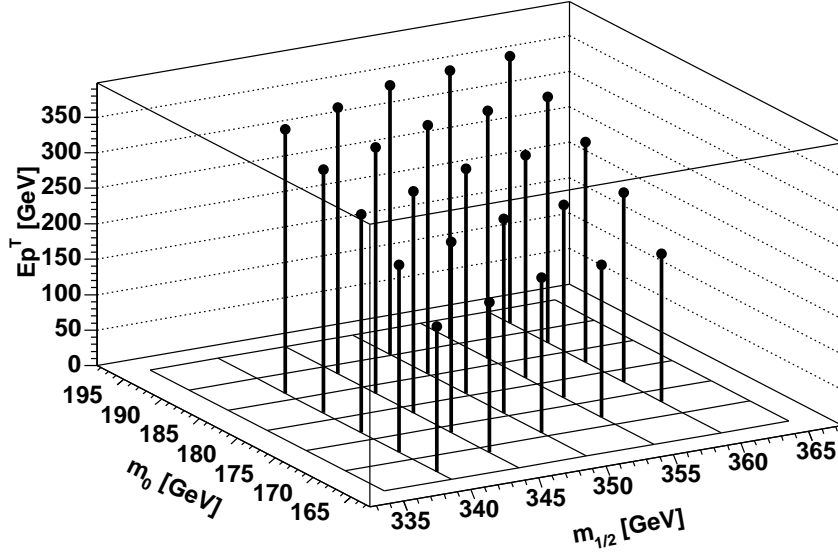


Figure 6.71: Theoretical kinematic endpoints in GeV for the invariant mass of the second rhos coming from the $\tilde{\tau}^\pm$ and the associated top quark coming from the stop in the $\tilde{t}_2 \rightarrow t + \tilde{\chi}_2^0$ decay. The endpoints decrease for decreasing values of m_0 .

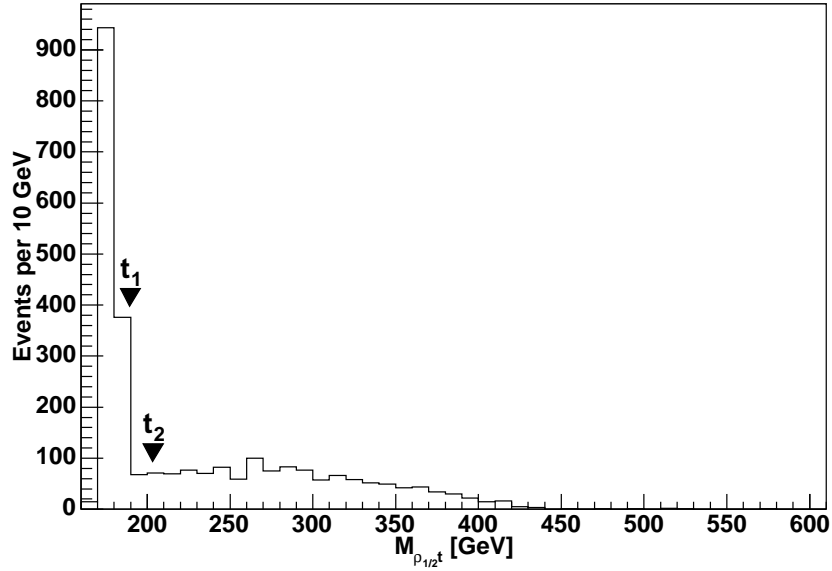


Figure 6.72: Example of $M_{\rho^\pm t}$ at $m_0 = 167$ and $m_{1/2} = 340$ after the cut on $M_{\rho^\pm \rho^\mp}$ at 30% of its maximum invariant mass (see section 6.2.8). 2676 events are represented. The two triangles show the theoretical values for events with \tilde{t}_1 (190.4 GeV) and \tilde{t}_2 (204.7 GeV), respectively. In this case it is possible to measure the endpoint of the $M_{\rho_2^\pm t}$ distribution.

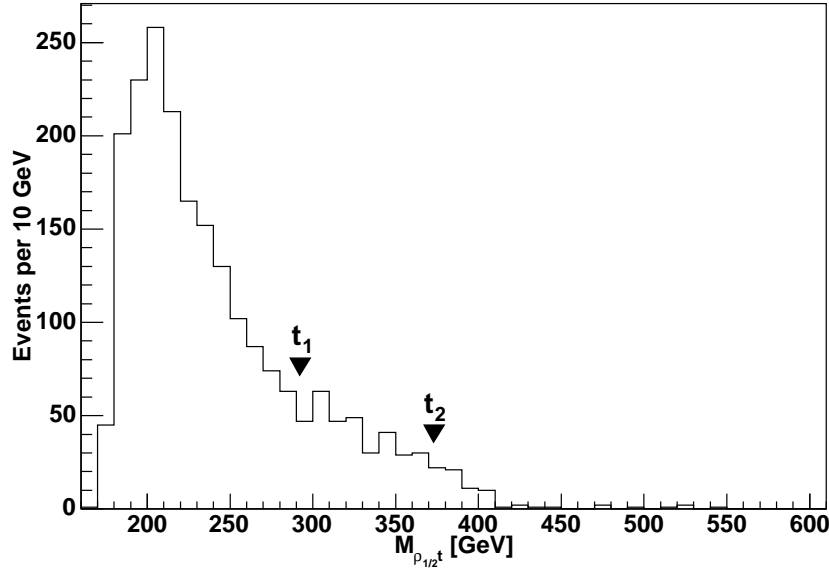


Figure 6.73: Example of $M_{\rho^{\pm}t}$ at $m_0 = 187$ and $m_{1/2} = 340$ after the cut at 30% of the maximum invariant mass of both rhos. 2140 events are represented. The two triangles show the theoretical values for events with \tilde{t}_1 (291.0 GeV) and \tilde{t}_2 (371.8 GeV), respectively. In this case, even with the cut, it is not possible to measure the endpoint of the $M_{\rho_2^{\pm}t}$ distribution.

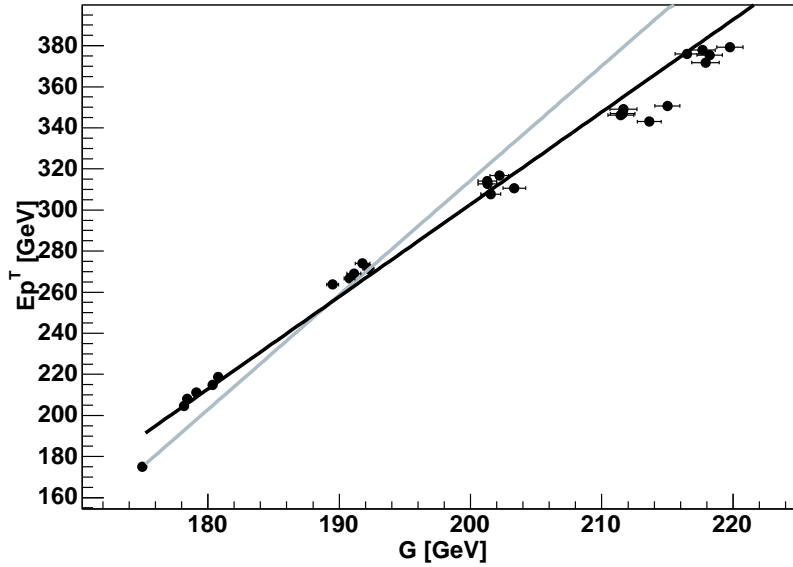


Figure 6.74: The theoretical kinematic $M_{\rho_2^{\pm}t}$ endpoints as a function of the measured gaussian maximum for all 25 investigated points in the m_0 - $m_{1/2}$ plane. The gray line is forced to go through the adapted origin whereas the black has an optimised adapted ordinate value of 15.4 GeV.

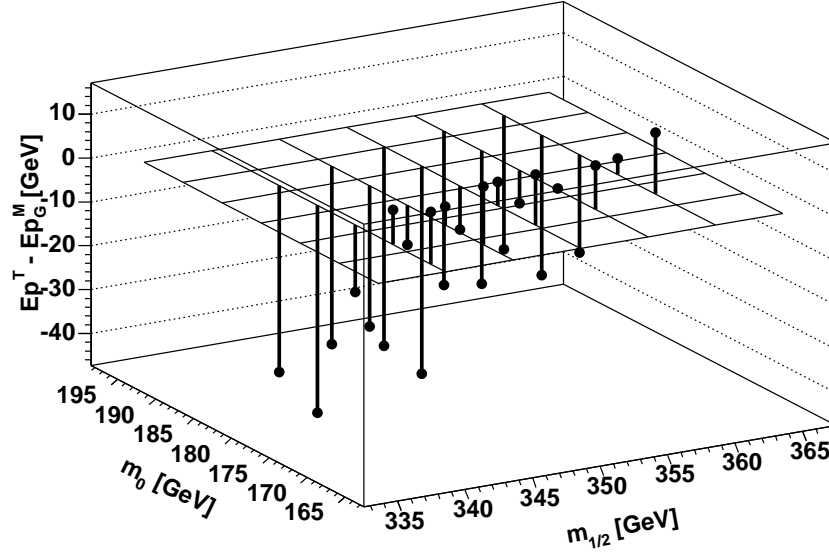


Figure 6.75: The difference of the theoretical and the measured $M_{\rho_2^{\pm}t}$ endpoint in GeV obtained with the gaussian fixed adapted origin method for all 25 points. The value is systematically too low on average by 14.6 GeV.

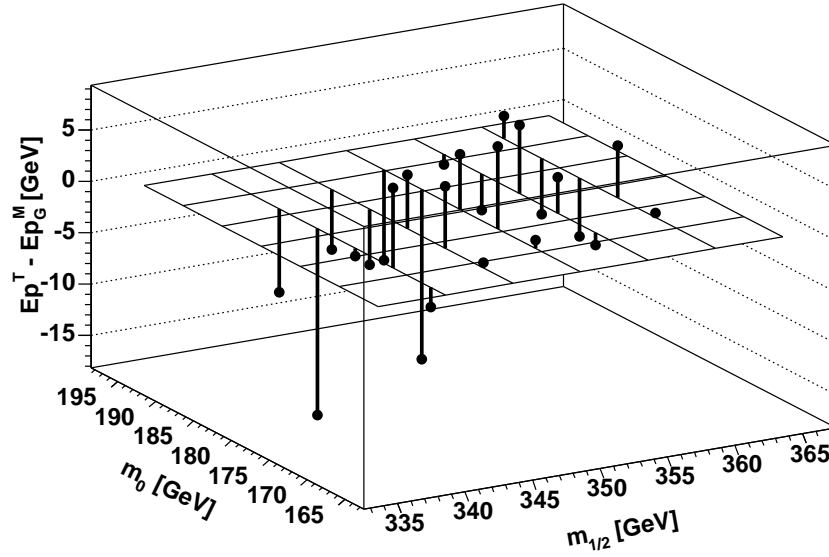


Figure 6.76: The difference of the theoretical and the measured $M_{\rho_2^{\pm}t}$ endpoint in GeV obtained with the gaussian non-fixed adapted origin method.

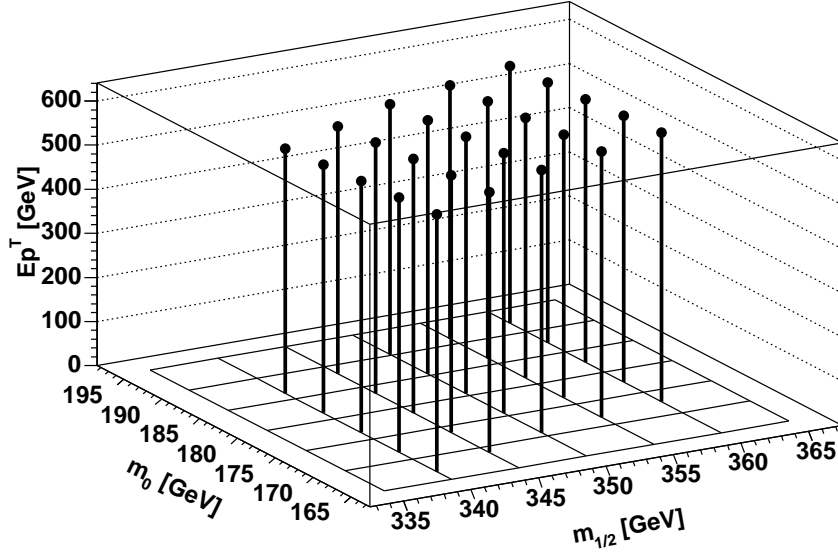


Figure 6.77: Theoretical kinematic endpoints in GeV for the invariant mass of first rho coming from the $\tilde{\chi}_2^0$ and the associated top quark coming from the stop in the $\tilde{t}_2 \rightarrow t + \tilde{\chi}_2^0$ decay.

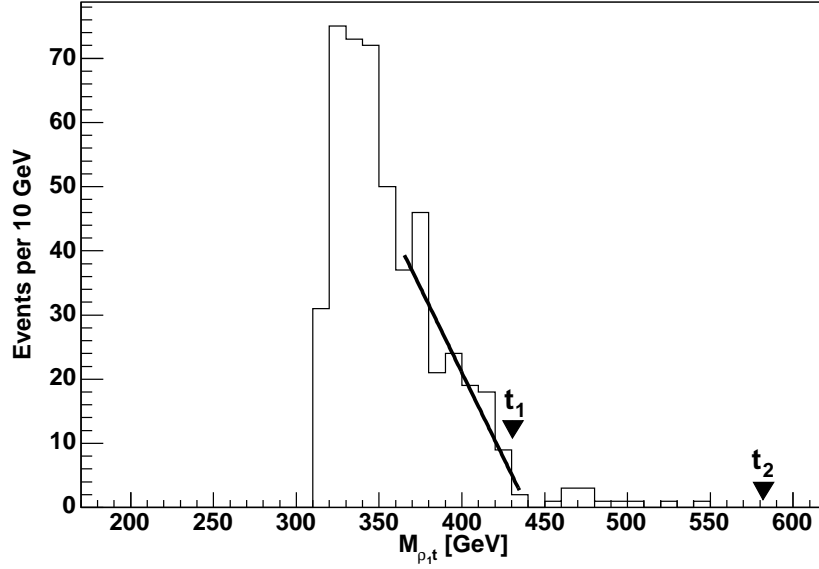


Figure 6.78: Example for the linear fit to the $M_{\rho^{\pm}t}$ distribution at $m_0 = 181$ and $m_{1/2} = 350$ after applying a cut on $M_{\rho^{\pm}t}$ at the theoretical second endpoint value. In this example 490 events are represented. The two triangles show the theoretical values for events with t_1 (429.2 GeV) and t_2 (582.3 GeV), respectively.

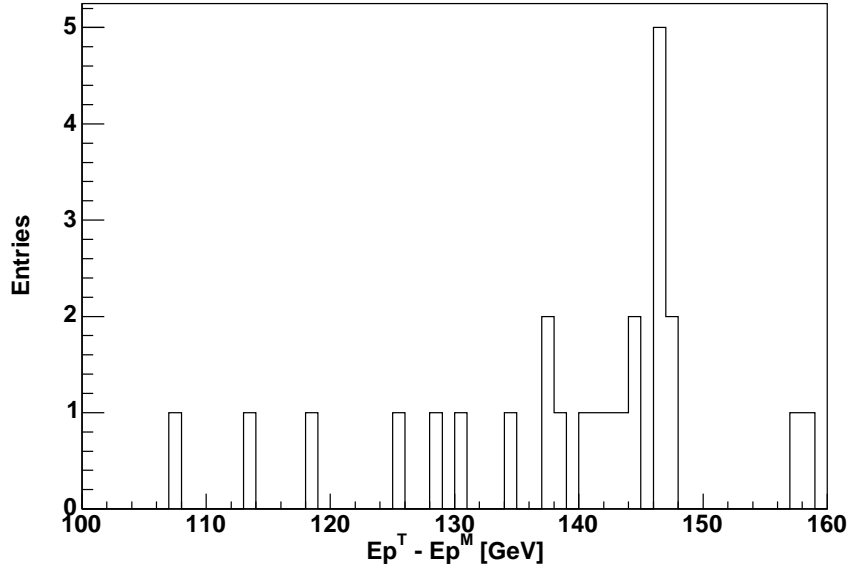


Figure 6.79: The difference of the theoretical and the measured $M_{\rho_1^{\pm}t}$ endpoint in GeV obtained with the linear fit for all 25 points. It shows a shift of 138.8 GeV with a root-mean-square deviation of 12.2 GeV.

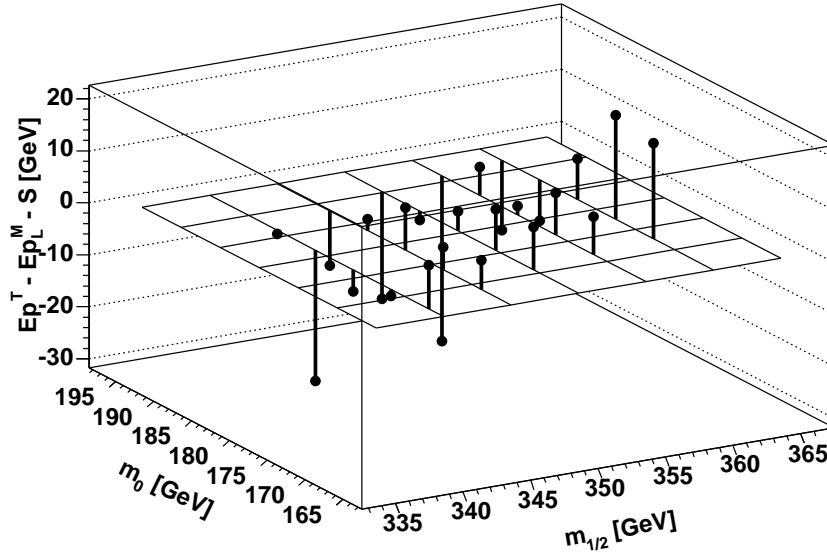
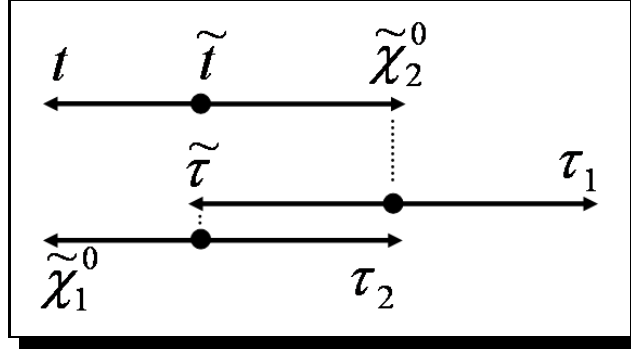


Figure 6.80: The theoretical $M_{\rho_1^{\pm}t}$ endpoint minus the measured endpoint in GeV obtained with the linear fit after applying the constant correction of 138.8 GeV.

6.2.15 The kinematic limit of $M_{\rho_1^\pm q} + M_{\rho_2^\mp q}$ for top quarks



Both methods can give an adequate estimate on the kinematic endpoint of the $M_{\rho_1^\pm t} + M_{\rho_2^\mp t}$ distribution. An example of such a distribution is shown in figure 6.82. The data sample is the same as used in section 6.2.13. The large correction $S = 127.3 \pm 28.5$ GeV for the linear fit is mainly caused by the stop mixing. A significant m_0 dependence which should be included into the correction can be seen in figure 6.84. Similar to the light and bottom quark case the gaussian method can be applied, which can be seen in figure 6.85. However, the gaussian function does not fit well in every case. In order to achieve adequate results for the gaussian fit the symmetric area is chosen to be 15% of the maximum bin value. The origin in the Ep^T - G plane has to be moved from (0,0) to (350,350) since two top quarks are involved. This is hence again called the “adapted” origin. Thus, the formula (6.8) changes to

$$Ep_i^T = C \cdot (G_i - 350) + D + 350. \quad (6.15)$$

The ratio between the slope of the fixed adapted origin fit and the slope in the non-fixed adapted origin fit has a value of 1.7. A summary of the measured values is given in table 6.19 which show that the \tilde{t}_2 definitely has an important influence on the endpoint measurement.

Value	Linear	Gaussian FO	Gaussian NFO
$\delta_{stat} Ep^M$	3.0 (3.0)	14.9	8.8
S	127.3 (-52.6)	1.3	1.9
δS	28.5 (18.2)	21.6	8.1

Table 6.19: A summary of the calculated mean uncertainties and systematic shifts in GeV for endpoint measurements in $M_{\rho_1^\pm t} + M_{\rho_2^\mp t}$. FO is with fixed origin and NFO with non-fixed origin. The values in brackets correspond to the case of \tilde{t}_1 being the input for the kinematic limit.

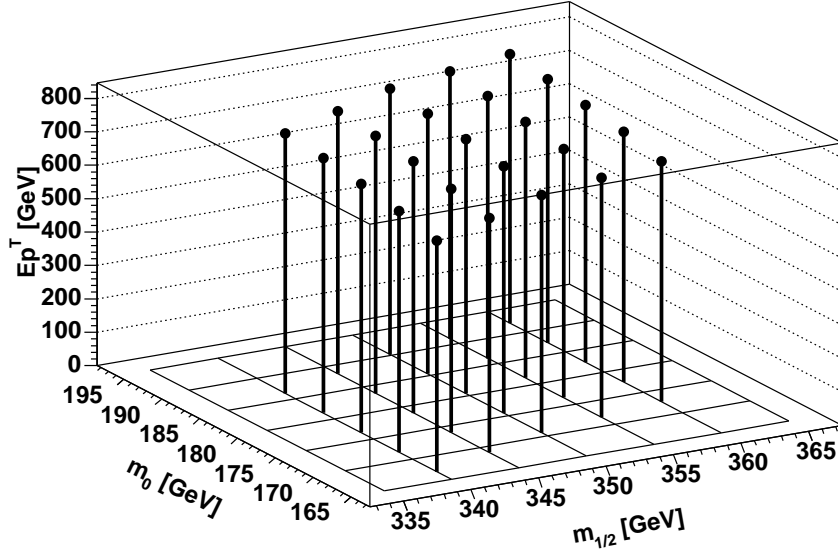


Figure 6.81: Theoretical kinematic endpoints for $M_{\rho_1^\pm t} + M_{\rho_2^\mp t}$ in GeV: The ρ_2^\mp coming from the $\tilde{\tau}$ with the top quark and the ρ_1^\pm coming from the $\tilde{\chi}_2^0$ and the same top quark from the $\tilde{t}_2 \rightarrow t + \tilde{\chi}_2^0$ decay.

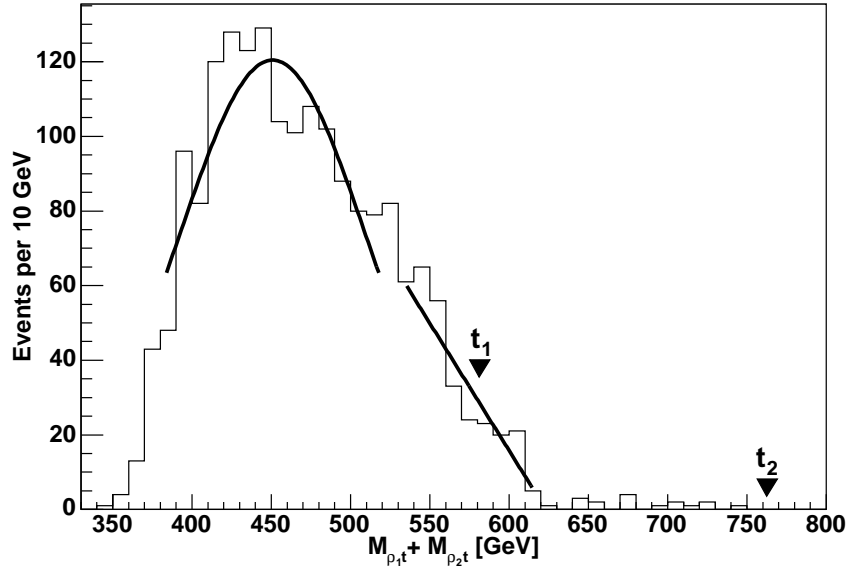


Figure 6.82: Example of a linear and a gaussian fit to $M_{\rho_1^\pm t} + M_{\rho_2^\mp t}$ at $m_0 = 181$ and $m_{1/2} = 350$. In this distribution 1859 events are represented. The two triangles show the theoretical values for events with \tilde{t}_1 (578.6 GeV) and \tilde{t}_2 (761.4 GeV), respectively.

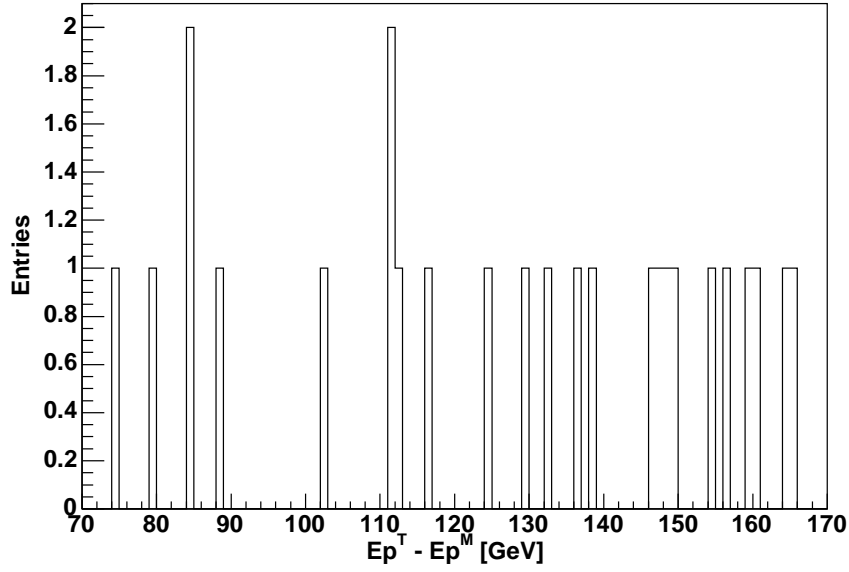


Figure 6.83: The difference of the theoretical and the measured $M_{\rho_1^\pm t} + M_{\rho_2^\mp t}$ endpoint in GeV obtained with the linear fit. It shows a large mean shift of 127.3 GeV with a root-mean-square deviation of 28.5 GeV.

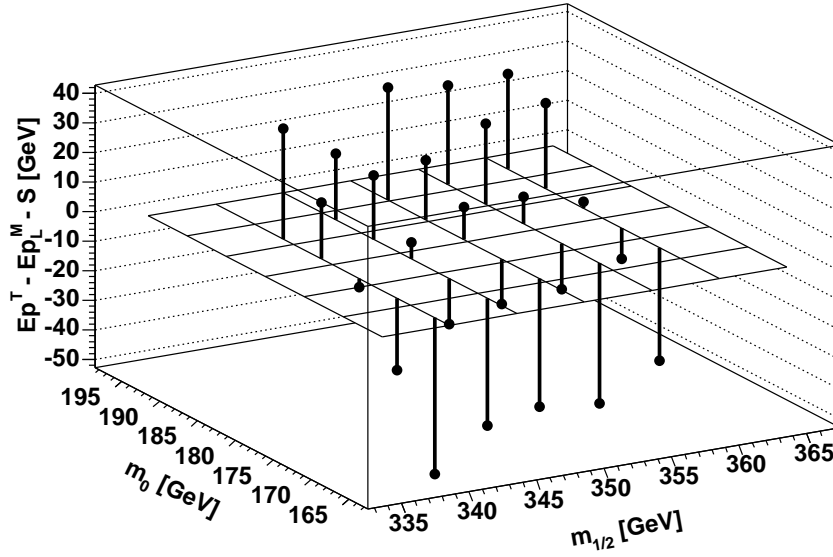


Figure 6.84: The theoretical endpoint minus the measured $M_{\rho_1^\pm t} + M_{\rho_2^\mp t}$ endpoint in GeV obtained with the linear fit after applying the constant correction of 127.3 GeV. The values decrease significantly for decreasing values of m_0 .

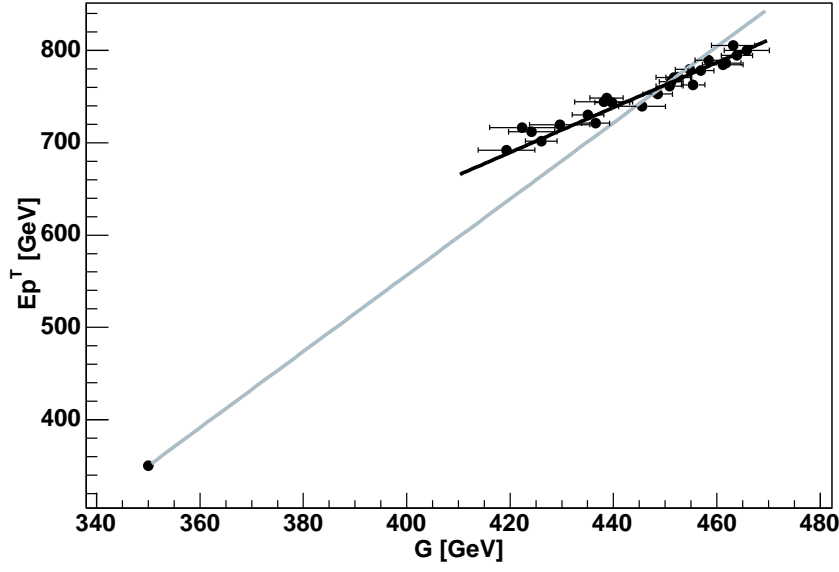


Figure 6.85: The theoretical kinematic endpoints as a function of the measured gaussian maximum for all 25 investigated points in the m_0 - $m_{1/2}$ plane. The gray line with $C = 4.3$ is forced to go through the adapted origin whereas the black line with $C = 2.4$ has an optimised adapted ordinate value of 169.0 GeV associated to the real ordinate value of -335.0 GeV.

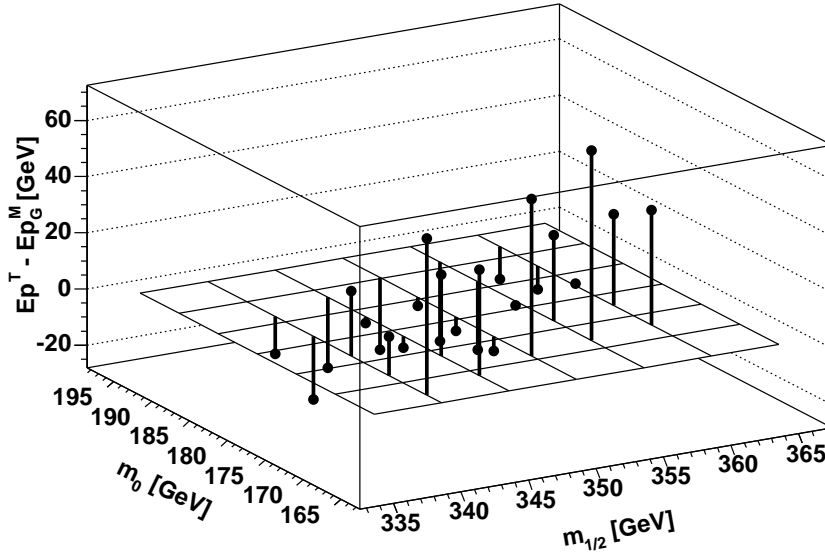


Figure 6.86: The difference of the theoretical and the measured $M_{\rho_1^\pm t} + M_{\rho_2^\mp t}$ endpoint in GeV obtained with the gaussian fixed origin method.

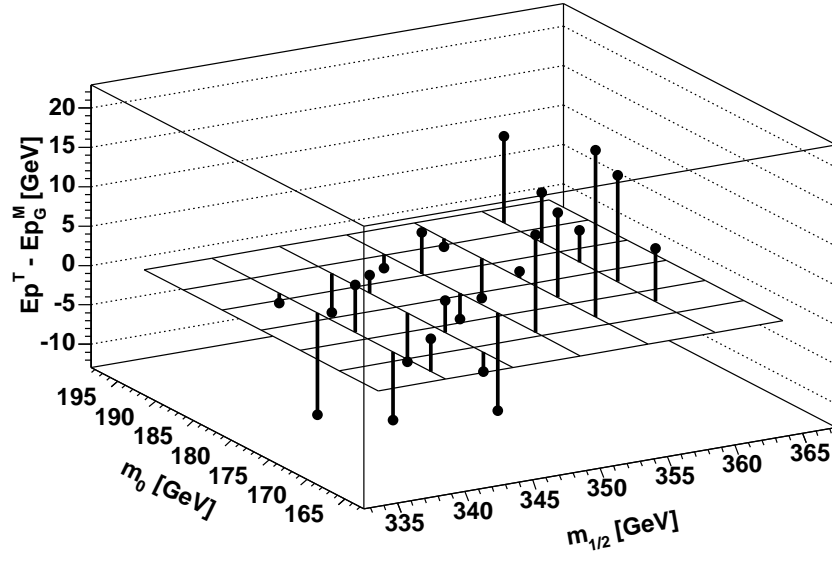


Figure 6.87: The difference of the theoretical and the measured $M_{\rho_1^\pm t} + M_{\rho_2^\mp t}$ endpoint in GeV obtained with the gaussian non-fixed adapted origin method.

6.2.16 Examples of measurements with 30 fb^{-1}

In the following a Monte Carlo sample at Γ is used which corresponds to an integrated luminosity of 30 fb^{-1} if all efficiencies and acceptances were 100%. The aim is to test the methods introduced in the previous sections for a low statistics sample. Table 6.20 shows the results of the endpoint measurements and figure 6.88 to 6.100 show all associated distributions.

<i>Distribution</i>	Linear	Gaussian FO	Gaussian NFO	Ep^T
$M_{\rho\rho}$	$83.5^{+0.5}_{-1.8}$	$81.0^{+4.3}_{-2.3}$	$81.2^{+4.7}_{-1.9}$	85.8
$M_{\rho\rho q}$	$614.8^{+5.0}_{-7.8}$	<i>n.a.</i>	<i>n.a.</i>	627.8
$M_{\rho_2 q}$	$320.0^{+83.7}_{-8.0}$	$300.2^{+8.6}_{-9.9}$	$296.7^{+7.7}_{-2.9}$	288.0
$M_{\rho_1 q}$	$594.3^{+4.2}_{-2.4}$	<i>n.a.</i>	<i>n.a.</i>	606.0
$\sum M_{\rho_i q}$	$742.7^{+5.7}_{-12.8}$	$770.6^{+15.3}_{-13.19}$	$774.1^{+10.3}_{-5.61}$	768.8
$M_{\rho\rho b}$	$560.4^{+11.7}_{-8.5}$	<i>n.a.</i>	<i>n.a.</i>	576.3
$M_{\rho_2 b}$	$219.2^{+25.4}_{-10.3}$	$265.2^{+12.0}_{-14.1}$	$262.4^{+10.6}_{-6.0}$	264.5
$M_{\rho_1 b}$	$542.3^{+10.4}_{-3.9}$	<i>n.a.</i>	<i>n.a.</i>	556.4
$\sum M_{\rho_i b}$	$700.0^{+11.7}_{-15.1}$	$679.0^{+17.9}_{-21.3}$	$686.3^{+12.0}_{-6.42}$	706.1
$M_{\rho\rho t}$	$592.2^{+11.3}_{-5.7}$	<i>n.a.</i>	<i>n.a.</i>	601.2
$M_{\rho_2 t}$	<i>n.a.</i>	$285.9^{+8.4}_{-21.6}$	$290.2^{+6.8}_{-6.8}$	316.7
$M_{\rho_1 t}$	$559.9^{+11.9}_{-12.2}$	<i>n.a.</i>	<i>n.a.</i>	582.3
$\sum M_{\rho_i t}$	$917.5^{+236.3}_{-28.5}$	$744.7^{+61.2}_{-21.6}$	$743.6^{+34.6}_{-8.1}$	761.4

Table 6.20: The measured values $Ep^M \pm_{\pm syst}^{stat}$ for 30 fb^{-1} . If endpoints are not available they are denoted with “n.a.”. All values are in GeV.

With the 13 measured endpoints it is now possible to reconstruct the masses of the involved sparticles. For the mass reconstruction the minimisation package MINUIT within the ROOT framework [22] is chosen. The input to the minimisation are the measured endpoint values with their associated formulae from section 5.2 and 5.3 and the measurement uncertainties $\delta = \sqrt{stat^2 + syst^2}$.

First, the measurements of the dilepton mass and the masses with the light quark with the smallest δ have been chosen. Thus, five endpoints are used to measure four masses. The result (with the masses calculated by ISASUGRA in brackets) is:

$$\begin{aligned}
M_{\tilde{d}/\tilde{s}_1} &= 787.5 \pm 35.5 \text{ GeV (782.6 GeV)} \\
M_{\tilde{\chi}_2^0} &= 261.6 \pm 25.5 \text{ GeV (265.5 GeV)} \\
M_{\tilde{\tau}_1} &= 157.4 \pm 26.5 \text{ GeV (150.1 GeV)} \\
M_{\tilde{\chi}_1^0} &= 144.3 \pm 25.7 \text{ GeV (138.1 GeV)}
\end{aligned} \tag{6.16}$$

The uncertainties given in 6.16 are noticeably larger if only the first four endpoints are used. There are two reasons for these, nevertheless, large uncertainties. First, the endpoints cannot be measured as precisely as it is possible for low $\tan\beta$ models due to the presence of neutrinos in the decay chains. Second, the equations for the endpoints are strongly correlated and therefore do not contain sufficiently complementary information which could compensate the endpoint uncertainties. By adding the endpoint measurements which involve the bottom quark the uncertainties can be improved and the sbottom mass can be measured. Here nine measured

values are taken to determine five unknown masses.

$$\begin{aligned}
M_{\tilde{d}/\tilde{s}_1} &= 778.4 \pm 28.2 \text{ GeV (782.6 GeV)} \\
M_{\tilde{t}_{b_2}} &= 710.8 \pm 25.7 \text{ GeV (724.9 GeV)} \\
M_{\tilde{\chi}_2^0} &= 256.9 \pm 20.4 \text{ GeV (265.5 GeV)} \\
M_{\tilde{\tau}_1} &= 150.9 \pm 21.2 \text{ GeV (150.1 GeV)} \\
M_{\tilde{\chi}_1^0} &= 138.2 \pm 20.5 \text{ GeV (138.1 GeV)}
\end{aligned} \tag{6.17}$$

With adding the endpoint measurements which involve the top quark the uncertainties on the reconstructed masses slightly increase due to the large endpoint uncertainties. However, the stop mass can be estimated. Here 13 measured values are taken for the determination of six unknown masses.

$$\begin{aligned}
M_{\tilde{d}/\tilde{s}_1} &= 795.2 \pm 29.9 \text{ GeV (782.6 GeV)} \\
M_{\tilde{t}_{b_2}} &= 743.1 \pm 28.8 \text{ GeV (747.9 GeV)} \\
M_{\tilde{t}_{b_2}} &= 727.2 \pm 27.2 \text{ GeV (724.9 GeV)} \\
M_{\tilde{\chi}_2^0} &= 272.4 \pm 21.7 \text{ GeV (265.5 GeV)} \\
M_{\tilde{\tau}_1} &= 164.5 \pm 22.6 \text{ GeV (150.1 GeV)} \\
M_{\tilde{\chi}_1^0} &= 151.9 \pm 21.9 \text{ GeV (138.1 GeV)}
\end{aligned} \tag{6.18}$$

The uncertainties on the masses are larger than the mass differences within the investigated area of the mSUGRA parameter space. However, it is at this level possible to give good estimates on these six sparticle masses.

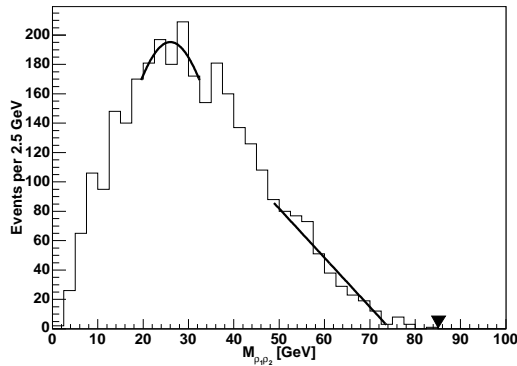


Figure 6.88: The invariant mass distribution of both opposite-sign rhos is based on 3062 events. The triangle shows the theoretical endpoint value at 85.8 GeV.

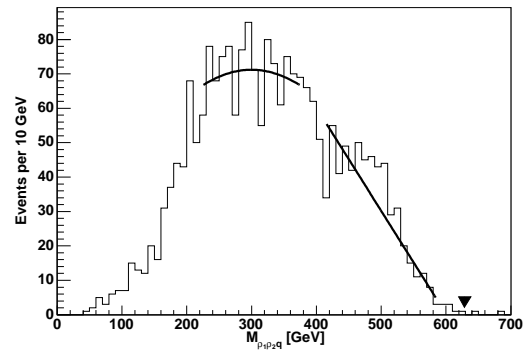


Figure 6.89: The invariant mass distribution of both rhos and the associated light quark is based on 2282 events. The triangle shows the theoretical kinematic endpoint of $M_{\rho^\pm \rho^\mp q}$ at 627.8 GeV.

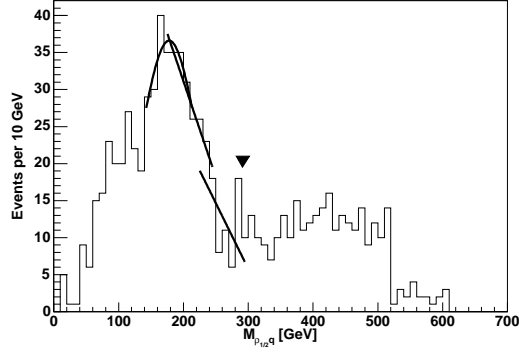


Figure 6.90: The invariant mass distribution of the second rho and the associated light quark with the first rho background is after the cut (55%) based on 844 events. The triangle shows the theoretical endpoint value at 288.0 GeV.

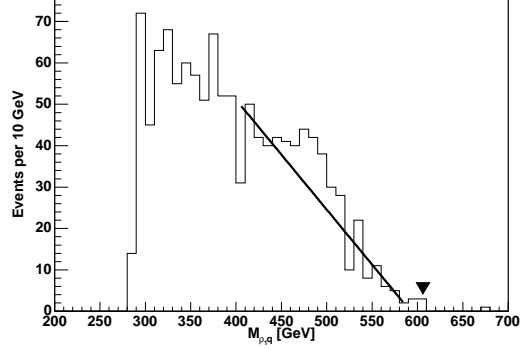


Figure 6.91: The invariant mass distribution of the first rho and the associated light quark is after the cut on the invariant mass $M_{\rho^{\pm}q}$ at the second endpoint based on 1199 events. The triangle shows the theoretical endpoint value at 606.0 GeV.

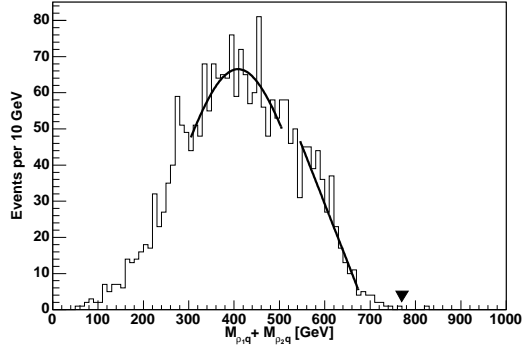


Figure 6.92: Example for the linear and the gaussian fit to the $M_{\rho^{\pm}q} + M_{\rho^{\mp}q}$ distribution at $m_0 = 181$ and $m_{1/2} = 350$. In this distribution 2282 events are represented. The triangle shows the theoretical kinematic endpoint at 768.8 GeV.

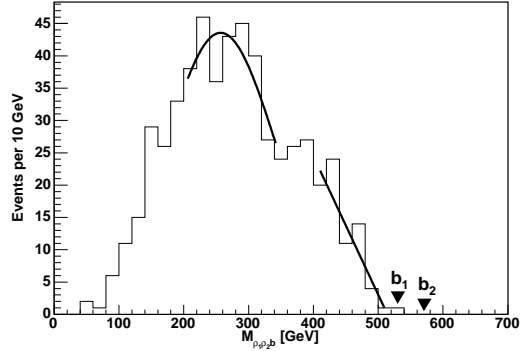


Figure 6.93: The invariant mass distribution of both rhos and the associated bottom quark is based on 550 events. The two triangles show the theoretical endpoint values for events with \tilde{b}_1 (532.9 GeV) and \tilde{b}_2 (576.3 GeV), respectively.

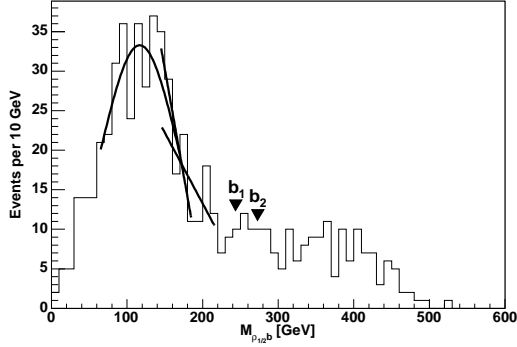


Figure 6.94: The invariant mass distribution of the second rho and the associated bottom quark with the first rho background is after the cut (30%) based on 642 events. The two triangles show the theoretical endpoint values for events with \tilde{b}_1 (244.7 GeV) and \tilde{b}_2 (264.5 GeV), respectively.

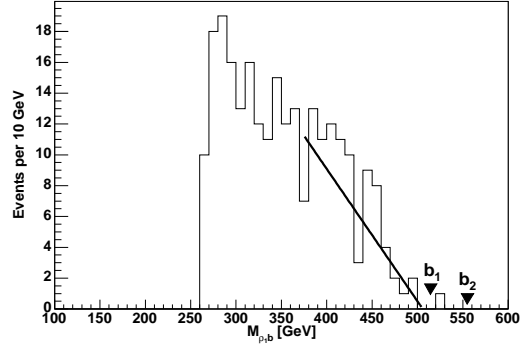


Figure 6.95: The invariant mass distribution of the first rho and the associated bottom quark is after the cut on the invariant mass $M_{\rho^{\pm}b}$ at the second endpoint based on 249 events. The two triangles show the theoretical endpoint values for events with \tilde{b}_1 (514.7 GeV) and \tilde{b}_2 (556.4 GeV), respectively.

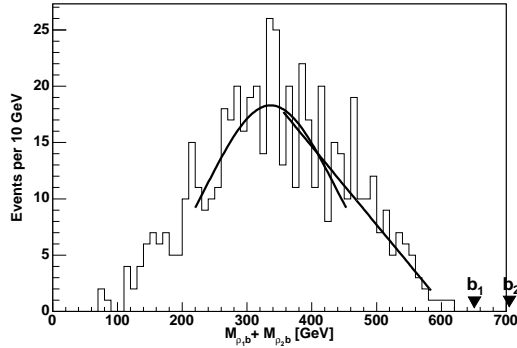


Figure 6.96: Example of a linear and a gaussian fit to the $M_{\rho_1^{\pm}b} + M_{\rho_2^{\mp}b}$ distribution at $m_0 = 181$ and $m_{1/2} = 350$. In this distribution 550 events are represented. The two triangles show the theoretical values for events with \tilde{b}_1 (653.1 GeV) and \tilde{b}_2 (706.1 GeV), respectively.

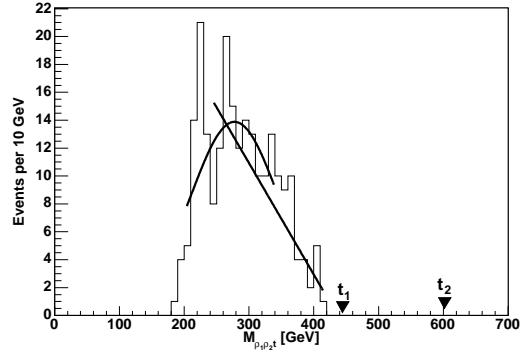


Figure 6.97: The invariant mass distribution of both rhos and the associated top quark is based on 230 events. The two triangles show the theoretical values for events with \tilde{t}_1 (446.1 GeV) and \tilde{t}_2 (601.2 GeV), respectively.

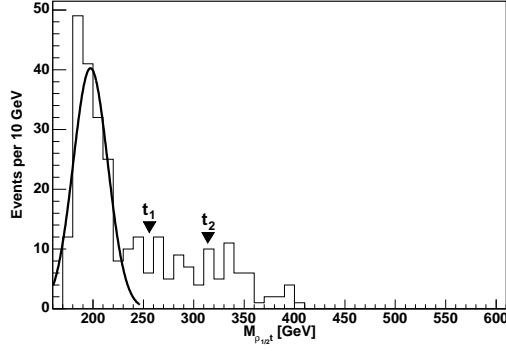


Figure 6.98: The invariant mass distribution of the second rho and the associated top quark with the first rho background is after the cut (30%) based on 280 events. The two triangles show the theoretical values for events with \tilde{t}_1 (257.1 GeV) and \tilde{t}_2 (316.7 GeV), respectively.

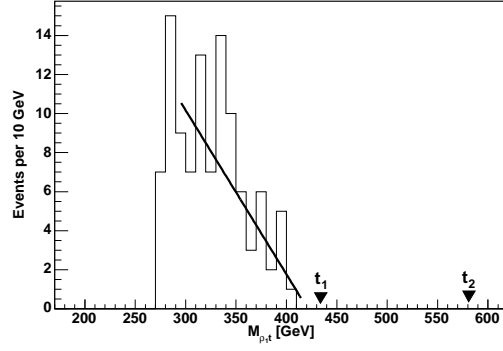


Figure 6.99: The invariant mass distribution of the first rho and the associated top quark is after the cut on $M_{\rho_{\pm}t}$ at the theoretical second endpoint value based on 112 events. The two triangles show the theoretical values for events with \tilde{t}_1 (429.2 GeV) and \tilde{t}_2 (582.3 GeV), respectively.

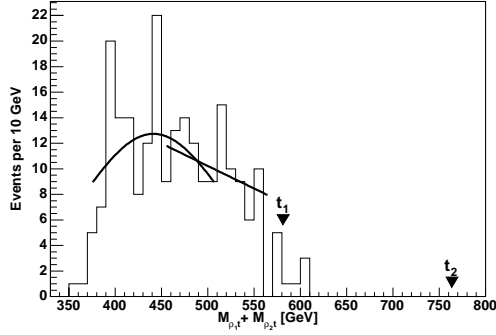


Figure 6.100: Example of a linear and a gaussian fit to $M_{\rho_1^{\pm}t} + M_{\rho_2^{\mp}t}$ at $m_0 = 181$ and $m_{1/2} = 350$. In this distribution 230 events are represented. The two triangles show the theoretical values for events with \tilde{t}_1 (578.6 GeV) and \tilde{t}_2 (761.4 GeV), respectively. Especially this figure shows the necessity to further optimise the fitting methods for low statistic samples.

Chapter 7

Conclusions

If nature is described by mSUGRA in the investigated region around I' there will be some difficulties to reconstruct the investigated sparticle masses in the dileptonic decay of the $\tilde{\chi}_2^0$. However, with the Large Hadron Collider the CMS and the ATLAS experiments would be able to find signals for Supersymmetry and to give an estimate of the sparticle masses. The results of this study can be summarised as follows:

1. Since the cascade decay of the $\tilde{\chi}_2^0$ is dominated by tau leptons at high $\tan\beta$ the dileptonic invariant mass distribution has no sharp edge at the kinematic limit.
2. The $\tau^\pm \rightarrow \rho^\pm \nu_\tau$ channel offers a good opportunity to search for endpoints.
3. In the investigated parameter space it is possible - at the Monte Carlo level - to reconstruct five to six sparticle masses in a 30 fb^{-1} data sample, with an uncertainty of about 20 to 30 GeV, by using the methods introduced in this study.
4. There is a linear dependence between the gaussian maximum and the theoretical endpoint for several mass distributions. Thus, endpoint measurements with a linear fit at the tail of the distribution can be well improved.
5. In principle it is possible to obtain two kinematic limits - the limit of $M_{\rho_1^\pm q}$ and $M_{\rho_2^\pm q}$ - by measuring the $M_{\rho^\pm q}$ distribution with a cut on the invariant mass of both opposite-sign rho mesons.
6. Top and bottom quark events can be well separated in the $M_{\rho\rho} - M_{\rho q}$ plane.
7. In the investigated parameter space the endpoints of the distributions involving bottom and top quarks are determined by the \tilde{b}_2 and \tilde{t}_2 , respectively. However, the measured endpoints with the linear fit method correspond more to the \tilde{b}_1 mass and \tilde{t}_1 mass, respectively, because \tilde{b}_1 and \tilde{t}_1 significantly dominate the distributions. Thus, it is generally very important to take the mixing of the involved particles into account.

Chapter 8

Outlook

In this study many simplifications have been applied. In order to obtain a more realistic prediction, at least the improvements given below have to be included. Furthermore, even at the Monte Carlo level additional studies like the investigation of the 3-prong channel may give useful information. The next steps towards a more detailed analysis are:

1. *Estimate of background*

This study does not take Standard Model backgrounds into account. Additionally, there is also a mSUGRA background coming from taus in chargino and other decays. An estimate of these backgrounds is necessary.

2. *Estimate of detector effects*

Since this study is purely at the Monte Carlo level, no detector effects have been taken into account. The CMS programs OSCAR for the full simulation, ORCA for the reconstruction and FAMOS for a combined fast detector simulation and reconstruction are necessary to give an estimate of detector effects.

3. *Investigation of the 3-prong channel*

Not only the $\tau^\pm \rightarrow \rho^\pm \nu_\tau$ channel can be used for the $\tilde{\chi}_2^0$ discovery at high $\tan \beta$. Due to the nearly similar particles involved in the decay chain, the $\tau^\pm \rightarrow \pi^\pm \pi^\mp \pi^\pm \nu_\tau$ channel should have related properties. Assuming the same efficiency and acceptance, its use would increase the statistics by a factor 2.5.

4. *Possible effect through spin correlations*

In the simulations no spin correlations are taken into account. However, it is possible to make an estimate how the spin correlations might have an effect on the invariant mass distributions. Since the statistics in the region of a kinematic endpoint depends on whether that special configuration is favoured or not the investigation of that configuration with respect to the spin gives a hint of the a possible effect.

Appendix A

Problems using PYTHIA 6.220

A.1 Bug in the hadronic tau decay

We found that in PYTHIA 6.220 the invariant mass distribution of the visible particles in the $\tau^\pm \rightarrow \rho^0 \pi^\pm \nu_\tau$ decay has a τ -energy dependence which is unphysical. Further investigations showed that the energy distribution of the ν_τ in the rest frame of the τ^\pm depends on the τ -energy in the laboratory frame of the program, which is a clear violation of Lorentz Invariance. According to the author the intended neutrino spectrum correction had not been obtained for taus with $E_\tau > 20m_\tau$, which is the limit where taus are boosted to their rest frame for better numerical precision [23]. The bug has been fixed in version 6.222, which has been released on the web [23] on 21st January 2004. However, the author remarks that the correction of the neutrino spectrum is still crude.

A.2 Particle listing

In the particle listings of PYTHIA 6.220 interfaced with ISASUGRA 7.69 we found some problems depending on the value of *MSTP(128)*. It is not clear whether the problem is caused by PYTHIA in this case. In the following the change of the particle listing due to different values of *MSTP(128)* is briefly presented. Particles in the documentation section have status three and particles in the rest of the particle listing have status one or two.

1. *MSTP(128) = 0*: For this value there is a huge overlap between the documentation section and the rest of the particle listing. All intermediate states are declared here, but it happens that particles point to their children, but the children point to the mother particle of their mother. This causes huge problems when selecting special decay chains.
2. *MSTP(128) = 1*: This is the value which is chosen in this study. Even here there are difficulties in finding the right decay chain, but it is possible to make unique assignments.
3. *MSTP(128) = 2*: In this case the problem is that particles in the particle listing with status one or two do not always point to the right mother particle in the documentation section with status three. It happens that intermediate states are totally missing sometimes. Since the particles in the documentation section carry no information about their children, it is therefore difficult to distinguish between different decay chains.

A.3 PYTHIA 6.220 and TAUOLA

We tried to use TAUOLA to solve the tau problem described in section A.1 but we did not achieve to run TAUOLA with PYTHIA and ISASUGRA. For Standard Model processes we

found no problem. C. Biscarat mentions this problem on her homepage [24] and we assume that the mixed order of particles in PYTHIA (see A.2) is responsible for that.

A.4 Calculated cross sections

It seems that there is a dependence of the cross section values on the selected production channels. We found changes in the production cross section of about 20 %.

Bibliography

- [1] S. L. Glashow, Nucl. Phys. **22** (1961) 579; S. Weinberg, Phys. Rev. Lett. **19** (1967) 1264; A. Salam, in *Elementary Particle Theory*, ed. N. Svartholm, Stockholm, Almqvist and Wiksell (1968), 367.
- [2] M. Spira and P.M. Zerwas arXiv:hep-ph/9803257.
- [3] L. Alvarez-Gaume, J. Polchinski and M.B. Wise, Nucl. Phys. B221, 495 (1983); L. Ibáñez, Phys. Lett. 118B, 73 (1982); J. Ellis, D.V. Nanopoulos and K. Tamvakis, Phys. Lett. 121B, 123 (1983); K. Inoue et al. Prog. Theor. Phys. 68, 927 (1982); A.H. Chamseddine, R. Arnowitt, and P. Nath, Phys. Rev. Lett., 49, 970 (1982).
- [4] H. Baer, C.-H. Chen, F. Paige and X. Tata, Phys.Rev. D50 (1994) 4508 and references therein, arXiv:hep-ph/9404212.
- [5] M. Battaglia et al., arXiv:hep-ph/0306219 v1, 23rd July 2003, (9) – (12).
- [6] G.W. Bennett et al. arXiv:hep-ex/0401008; H.N. Brown et al. 2001 Phys. Rev. Lett. **86** 2227.
- [7] S. J. Asztalos et al. arXiv:astro-ph/0104200.
- [8] S. Dawson, arXiv:hep-ph/9712464 v1, 19th December 1997.
- [9] S.P. Martin, arXiv:hep-ph/9709356 v3, 7th April 1999.
- [10] H. Baer et al., ISAJET 7.69, arXiv:hep-ph/0312045.
- [11] T. Sjöstrand, P. Edén, C. Friberg, L. Lönnblad, G. Miu, S. Mrenna and E. Norrbin, Computer Physics Commun. 135 (2001) 238.
- [12] K. Hagiwara et al. (Particle Data Group), Phys. Rev. D 66, 010001.
- [13] LEP Higgs Working Group, arXiv:hep-ex/0107030.
- [14] LEPSUSYWG, ALEPH, DELPHI, L3 and OPAL experiments, note LEPSUSYWG/02-06.2, LEP2 Susy Working Group.
- [15] <http://map.gsfc.nasa.gov/> - image gallery.
- [16] Wilson, R.W.; Penzias, A.A. Bell Telephone Labs., Holmdel, N. J. Science, 156: 1100-1 (May 26, 1967).
- [17] M. Davier et al., arXiv:hep-ph/0208177.
- [18] <http://hepweb.rl.ac.uk/ppUKpics/> - archive.
- [19] CERN Courier, February 1999, “A cold start for LHC”.
- [20] Luc Pape, private communication.

- [21] I. Iashvili and A. Kharchilava, CMS Note 1997/065; S. Abdullin et al., CMS Note 1998/006; D. Denegri, W. Majerotto and L. Rurua, CMS Note 1997/094.
- [22] Rene Brun and Fons Rademakers, ROOT - An Object Oriented Data Analysis Framework, Proceedings AIHENP'96 Workshop, Lausanne, Sep. 1996, Nucl. Inst.& Meth. in Phys. Res. A 389 (1997) 81-86. See also ROOT Webpage.
- [23] <http://www.thep.lu.se/torbjorn/pythia/pythia6222.update>.
- [24] http://cbiscara.home.cern.ch/cbiscara/tauola_valid.html.

Acknowledgements

First of all, I want to thank Prof. Felicitas Pauss for giving me the possibility to carry out my diploma thesis in her group on a highly interesting topic, and for great support in various concerns. I am very grateful for the excellent supervision by the two experts Dr. André Holzner and Dr. Luc Pape. It was a great pleasure to work with Giovanna Davatz, Prof. Günther Dissertori, Dr. Michael Dittmar, PD Klaus Freudenreich, Gabriele Kogler, Anne-Sylvie Nicollrat and Radoslaw Ofierzynski. My special thanks go to my friends who exceedingly enriched my life during my studies at ETH Zurich. I want to express my gratitude to my family who supported me unconditionally during my life.

